ROYAUME DU MAROC
Université Mohammed V - RABAT -
جامعة محمد الخامس – الرباط –
Faculté des sciences
كلية العلوم
CENTRE D'ETUDES DOCTORALES - SCIENCES ET TECHNOLOGIES

N° d'ordre 3210

THESE

En vue de l'obtention du : ***DOCTORAT***

Structure de Recherche: ***Équipe de Sciences de la Matière et du Rayonnement***
Discipline: ***Physique***
Spécialité: ***Physique médicale***

Présentée et soutenue le 12/06/2019 par:

Rahal SAAIDI

Validation of a Monte Carlo Simulation of Three Siemens Clinical PET/CT Scanner Using GATE and Optimization of Scanner Performance

JURY

Yassine HASSOUNI	PES, Faculté des Sciences, Université Mohammed V, Rabat	Président
Mustapha BOUGTEB	PES, Faculté des Sciences et Techniques, Université Hassan I, Settat	Examinateur
Rajaa CHERKAOUI EL MOURSLI	PES, Faculté des Sciences, Université Mohammed V, Rabat	Directeur de Thèse
Driss BENCHEKROUN	PES, Faculté des Sciences Ain Chock Université Hassan II, Casablanca	Rapporteur/ Examinateur
Yahya TAYALATI	PES, Faculté des Sciences, Université Mohammed V, Rabat	Rapporteur/ Examinateur
Rachid MAZINI	Docteur, Institute of Physics, Academia Sinica, Taipei, Taïwan	Invité

Année Universitaire : 2018/2019

... To the memory of my father Ibrahim... who always believed in me. Miss you. ... to my mother! Love you! to my brothers and sisters

...

Acknowledgements

This thesis is realized under direction of my supervisor, Professor Rajaa CHERKAOUI El Moursli, at the " Research Group of Matter and Radiation Science (ESMaR: Équipe de Sciences de la Matière et de Rayonnement)" Faculty of Sciences, Mohamed V University, Rabat.
First of all, I would like to express my sincere gratitude to my supervisor, Rajaa CHERKAOUI El Moursli from Faculty of sciences, Mohammed V University, Rabat for the continuous support of my Ph.D study and related research, for her patience, motivation, and immense knowledge. Her guidance helped me in all the time of research and writing of this thesis. I deeply appreciate her never ending encouragements.
I would like to thank professor Yassine HASSOUNI from Faculty of Sciences, Mohamed V University, Rabat for accepting to judge my thesis work and being president in my thesis defense.
I would like to thank professor Driss BENCHEKROUN from faculty of Science Ain Chock, Hassan II university, Casablanca for reviewing my thesis report and accepting to judge my thesis work.
I would like to thank the lab director professor Yahya TAYALATI from Faculty of Sciences, Mohamed V University, Rabat for reviewing my thesis report and accepting to judge my thesis work and your encouragement your enlightened advices and your assistance during this PhD period.
I would like to thank professor Mustapha BOUGTEB from Faculty of Science and Technology, Hassan I University, Settat for accepting to judge my thesis work.
I would like to thank Doctor Rachid MAZINI, Senior Research Scientist from Institute of Physics, Academia Sinica, Taiwan for reviewing my thesis report and accepting to judge my thesis work.
I would like to thank all members of the E-Science team, especially Santiago Gonzalez de la Hoz and Salt Cairols, José F of the Instituto De Física Corpuscular (IFIC) and Professor Farida Fassi from Mohamed V University for the financial support and the training course in the GRID Computing in IFIC in the frame of the coperation under the agreement I-COOP mode B Reference COOPB20247 between IFIC Instituto Fisica Coruscular of Valancia (Spain) and the University Mohammed V in Rabat entitled: Launching a platform of GRID computing in Morocco to meet the new challenges of physics research.
The help of Dr Yassine TOUFIQUE, is worth mentioning. Thanks a lot for your fruitful discussions and the proof-reading of paper.
I thank all the members of the ESMaR for their warm welcome and their encouragement their enlightened advice and their effective help us allowed to structure and carry out this project. Also, to everyone else that I might have forgotten.

Abstract

In this thesis work, we used GATE platform (Geant4 Application for Tomographic Emission), based on GEANT4 Monte Carlo code, to validate the clinical PET scanner ECAT EXACT HR+, $Biograph^{TM}$ True point (True V) and $Biograph^{TM}$ mCT 20 Excel according to the NEMA NU 2-2001 protocol and the NEMA NU 2-2012 protocol. Our results showed good agreement with experimental data. The first validated model ECAT EXACT HR+ is used to study the influence of the coincidence timing windows(CTW) and dead time (DT) on the Count rate performance. The obtained results show that the minimizing coincidence time windows increase the NECR and True count rate performance. Moreover, the NECR is increased when non paralyzable dead time is mployed instead of paralyzable one. The validated model of $Biograph^{TM}$ mCT 20 Excel is used to study the effect of the coincidence time window along with the block gap and the intercrystal gap on the count rate performance and the spatial resolution. The results showed that a decrease in the coincidence time window and the block gap and an increase in the intercrystal gap increase the count rate performance and improve the spatial resolution. In addition, the both scanner $Biograph^{TM}$ mCT 20 Excel and the $Biograph^{TM}$ True point (with True V option) scanner validated using GATE were used to perform the image quality, Accuracy of attenuation, and scatter correction according the NEMA/IEC body phantom. The obtained images show a good image quality.

Keywords__ PET Scanner; NEMA; GATE; dead time; Coincidence Windows time.

Résumé

Dans ce travail de thèse, la plate-forme GATE (Application Geant4 pour émission tomographique) a été utilisée pour valider la simulation des scanners PET (Positron Emission Tomography) clinique suivants ECAT EXACT HR+, $Biograph^{TM}$ True point (True V) et $Biograph^{TM}$ mCT 20 Excel selon le protocole NEMA NU 2-2001 et NEMA NU 2-2012. Nos résultats montrent un bon accord avec les données expérimentales. Le premier modèle validé ECAT EXACT HR+ est utilisé pour étudier l'influence des fenêtres temporelles de coïncidence et du temps mort sur le rendement du taux de comptage. Les résultats obtenus montrent que la Minimisation les fenêtres de temps de coïncidence augmentent la performance du taux de comptage NECR et vrai. De plus, le NECR est augmenté lorsque nous utilisons un temps mort non paralysable au lieu de paralysable. Le modèle validée de $Biograph^{TM}$ mCT 20 Excel est utilisée pour étudier l'effet de la fenêtre temporelle de coïncidence avec l'écart de bloc et l'écart entre cristaux sur les performances du taux de comptage et la résolution spatiale. Les résultats obtenues montrent que la diminution de fenêtre temporelle de coïncidence et l'écart de bloc ainsi qu'une augmentation de l'écart intercristal augmentent les performances du taux de comptage et améliorent la résolution spatiale. Pour les deux scanners $Biograph^{TM}$ mCT 20 Excel et $Biograph^{TM}$ True Point (True V), cette simulation permet d'améliorer la qualité d'image, la précision de l'atténuation et correction de dispersion selon le fantôme de corps NEMA / IEC.

Mots-clés :__scanner PET ; NEMA; GATE; temps mort; fenêtre temporelle.

Résumé détaillé

Dans ce travail de thèse,le but est de valider la plate-forme GATE (Application Geant4 pour émission tomographique) pour la simulation de trois scanners de tomographie par émission de positrons (TEP) selon le protocole NEMA NU 2-2001 et NEMA NU 2-2012. Ce qui inclut le développement de softwares, les déploiements des logicielles sur la grille de calcul et la comparaison avec les données expérimentales.
En effet, depuis quelques décennies, les simulations Monte Carlo pour le transport de rayonnement ont été largement utilisées en dosimétrie et en physique médicale comme alternative aux calculs analytiques. Des résultats très précis sont maintenant obtenus avec ces techniques grâce aux puissantes ressources informatiques distribuées sur la grille.
GATE est un logiciel Open source de type orienté objet C++, qui a été développé par la collaboration internationale OpenGATE pour la simulation en médecine nucléaire. L'objectif initial (en 2004) était consacré à la tomographie par émission de positrons (TEP) et à la tomographie par émission de photons uniques (SPECT), mais a été étendu par la suite à la radiothérapie. Développé à base de la boîte à outils de simulation GEANT4, GATE hérite de tous les modèles de physique bien validés, et fournit aux utilisateurs des composants spécifiques intégrés polyvalents, pour gérer facilement une géométrie complexe, des sources, l'interaction rayonnement matière, et enfin extraire et traiter les informations pertinentes de la simulation. Ces fonctionnalités ont participé à la croissance et à l'évolution rapide de GATE pour les applications en physique médicale. GATE dans ses versions récentes joue maintenant un rôle clé dans la conception de nouveaux dispositifs d'imagerie médicale, dans l'optimisation des protocoles d'acquisition et dans les calculs de dose pour la radiothérapie.
C'est dans cette perspective que mon travail de thèse a été consacré principalement au développement d'un modèle de calcul numérique utilisant le logiciel Monte Carlo GATE pour la simulation des scanners TEP cliniques suivants ECAT EXACT HR+, $Biograph^{TM}$ True point (True V) et $Biograph^{TM}$ mCT 20 Excel selon le protocole NEMA NU 2- 2001 et NEMA NU 2-2012. Le modèle développé comprend les principaux composants du scanner et un fantôme selon le protocole NEMA.
Les performances des données expérimentales mesurées sont reproduites avec précision par GATE, en particulier les données expérimentales concernant le taux de comptage maximal de coïncidences vraies, le taux de comptage équivalent de bruit (NECR), la fraction diffusée, la sensibilité et la résolution spatiale. Le travail de simulation a été validé avec succès par comparaison avec les distributions expérimentales. En effet, un bon accord entre les simulations et les mesures a été observé pour tous ces paramètres. Le modèle de simulation validé pour ECAT EXACT HR+ a permis d'étudier l'influence des fenêtres temporelles de coïncidence et du temps mort sur le rendement du taux de comptage et le taux de comptage équivalent le bruit (NECR). Les résultats obtenus montrent que la minimisation des fenêtres de temps de coïncidence augmente la performance du taux de comptage. Le modèle validé pour le scanner $Biograph^{TM}$ mCT 20 Excel a été exploité pour analyser l'effet de la fenêtre temporelle de coïncidence avec l'écart de bloc et l'écart entre cristaux sur les performances du taux de comptage et la résolution spatiale. Cette

analyse montre que la diminution de fenêtre temporelle de coïncidence et l'écart de bloc ainsi qu'une augmentation de l'écart inter-cristal augmentent les performances du taux de comptage et améliorent la résolution spatiale. Pour les deux scanners $Biograph^{TM}$ mCT 20 Excel et $Biograph^{TM}$ True point (True V), la simulation permet de définir les paramètres qui permettent d'améliorer la qualité d'image, la précision de l'atténuation et la correction de dispersion selon le fantôme de corps NEMA/IEC. Le but est d'obtenir la meilleure image nécessaire pour un bon diagnostic et d'optimiser la dose administrée au patient.

La thèse est structurée de la manière suivante. Après une introduction générale, le chapitre I présente les notions fondamentales et les principes de fonctionnement du TEP ainsi que les différents modes d'acquisition et l'état de l'art de la technique des machines TEP cliniques actuelles. Le chapitre II est consacré à la reconstruction de l'image, une étape cruciale dans cette technique d'imagerie importante pour un bon diagnostic médicale. Différentes techniques mathématiques complexes sont utilisées pour la reconstruction d'une image à deux ou trois dimensions. Ces simulations nécessitent beaucoup de temps de calcul et de mémoire. Les méthodes décrites sont divisées en deux catégories : les méthodes analytiques et les méthodes itératives. La reconstruction de l'image est complétée par différentes corrections tenant compte d'effets secondaires et de biais expérimentaux, afin d'améliorer la qualité de l'image finale servant pour le diagnostic. Le chapitre III est dédié à la description des principes des simulations de Monte Carlo, et des codes de simulation des performances des machines PET-Scan. Une liste des outils développés au cours des dernières années et exclusivement dédiés à la technique TEP, contrairement aux outils plus complets et traitant de manière générale l'interaction rayonnement matière, est dressée avec les avantages et les inconvénients de chaque outil. Une description détaillée des différentes étapes de la simulation sous GATE est Faite dans ce chapitre. Une liste des différents systèmes modélisés dans le simulateur est également dressée, ainsi que les techniques de parallèlisation, la simulation sur la grille de calcul et l'algorithme du reconstruction du code STIR (Software for Tomographic Image Reconstruction). Enfin dans le chapitre IV, les résultats des calculs de simulation et leur validation par comparaison avec des données expérimentales pour chaque PET/CT sont exposés. S'en suit par la suite une étude de l'effet de fenêtres temporelle de coïncidence et le temps mort et de l'intervalle de bloc et de l'inter-cristal sur le taux de comptage et la résolution spatiale, donc sur la qualité de l'image.
En conclusion, la plate-forme GATE un outil fiable et compétitive aux logiciels commerciaux de l'imagerie médicale PET. Les résultats obtenus peuvent être utiles pour la conception et l'amélioration du PET/CT.

Mots-clés :__ Tomographie par émission de positrons (PET); NEMA; Application Geant4 pour émission tomographique (GATE); temps mort; fenêtre temporelle de coïncidence.

Contents

List of Figures

List of Tables

List of Abbreviations

AMIDE	**A**mide is a **M**edical **I**magine **D**ata **E**xaminer
ACF	**A**ttenuation **C**orrection **F**actor
BGO	**B**ismuth **G**ermanate
CT	**C**omputed **T**omography
CTW	**C**oincidence **T**ime **W**indows
DT	**D**ead **T**ime
DOI	**D**epth of **I**nteraction
EGS	**E**lectron and **G**amma **s**hower
FWHM	**F**ull **W**idth at **H**alf **M**aximum
FDG	[^{18}F]**F**luoro-2-**D**eoxy-D-**G**lucose
FOV	**F**ield of **V**iew
FBP	**F**iltered **B**ackprojection
FORE	**FO**rier **RE**binning
Geant4	**G**eometry **A**nd **T**racking
GATE	**G**eant **A**pplication for **T**omographic **E**mission
GSO	Cerium-doped **G**adolinium **O**xyorthosilicate
IQ	**I**mage of **Q**uality
LOR	**L**ine of **R**esponse
LSO	Cerium-doped **L**utetium **O**xyorthosilicate
LYSO	**L**utetium **Y**ttrium **O**xyorthosilicate
LuAp	**L**utetium **Y**ttrium **A**luminate
LMF	**L**ist **M**ode **F**ormat
MLEM	**M**aximum **L**ikelihood **E**xpectation **M**aximization
MCNP	**M**onte-Carlo **N** **P**articles
NEMA	**N**ational **E**lectrical **M**anufacturers **A**ssociation
NaI(Tl)	**T**allium-doped **S**odium **I**odide
NECR	**N**oise **E**quivalent **C**ount **R**ate
OSEM	**O**rdered **S**ubset **E**xpectation **M**aximization
PET	**P**ositron **E**mission **T**omography
PMT	**P**hotomultiplier **T**ube
PENELOPE	**PEN**etration and **E**nergy **LO**ss of **P**ositrons and **E**lectrons
PSF	**P**oint **S**pread **F**unction
RAMLA	**R**ow **A**ction **M**aximization **L**ikelihood **A**lgorithm
ROI	**R**egion of **I**nterest
SF	**S**catter of **F**raction
STIR	**S**oftware for **T**omographic **I**mage **R**econstruction
SimSET	**S**imulation **S**ystem for **E**mission **T**omography
SPECT	**S**ingle **P**hoton **E**mission **C**omputed **T**omography
SSRB	**S**ingle **S**lice **R**ebinning
SBR	**S**phere-to-**B**ackground-activity-**R**atio

TOF **T**ime of **F**light

Introduction

Positron Emission Tomography (PET) system is a medical imaging technique used to diagnose cancer, based on a 3D distribution of a radiotracer in the target organ, by injecting a radioactively labeled molecule into the patient's body. The isotopes used in PET are positron emitters. After a short path in the surrounding tissues, the positrons emitted by the isotope attached to the radiotracer annihilate electrons inside the target organ and produce two 511 keV photons in opposite directions. The PET is based on coincidence detection of these two photons [1, 2]. It is realized in accordance with the specifications of the manufacturers via a coincidence time windows(CTW) and a dead time module for specific volume within the Sensitive Detector system. Modern PET scanners are coupled with computed tomography (CT) systems for more precise anatomical localization of cancer cells [2]. The combined PET/CT system is a major development in nuclear medicine and is capable of creating complex corrected PET images by multiplying the emission scan by the attenuation correction map generated by X-ray CT. This enhances the count rate, spatial resolution as well as upgrades clinical conditions, diagnostics, development and treatment planning [2]. The obtained images quantification reliability is affected by detector performance limits (spatial resolution and energy, sensitivity), physical effects such as attenuation and diffusion, disrupting the formation of images, physiological effects (movements of the patient) and effects related to tomographic reconstruction. In order to optimize the image quality, Monte Carlo simulations are used as a useful and effective tool for studying the influence of components, geometry and camera acquisition parameters to optimize best system configuration. Several Monte Carlo packages for designing complex configurations are available (e.g., PENELOPE, MCNP, GEANT4, EGSnrc) [3]. The free open-source software GATE is frequently used for simulating tomographic experiments for PET and single-photon emission CT (SPECT) systems because of its flexibility [4]. GATE includes specific modules required to perform realistic simulations of nuclear medicine experiments. These modules allow easy control of the most important parameters on which the precision of the Monte Carlo simulation depends, including the description of the detector geometry, the description of the source geometry, and the acquisition process. The user builds the geometry and activates a model of physics process needed for the simulation by executing a simple configuration file (a macro file) containing commands interpreted by GATE [5]. The main object of this thesis is the validation of the Monte Carlo simulation of three commercially available PET scanners and the study of the influence of several parameters such as the coincidence windows time, the dead time, the block/crystal Gap on count rate performance and spatial resolution to optimise the image quality. The realization of this work takes into account considerable Monte-Carlo simulations time. In order to reduce this time, we have used the local computer cluster in our laboratory.
This thesis presented here is structured as follows:

- Chapter I, introduce the important notions necessary for understanding the PET. It first briefly describes the Positron Emission Tomography (PET). Then, it sets out in more detail the physical context including its operating principle , the processing of its signals, as well as their characteristics. In addition, we introduce the different acquisition modes and a state of the art of the current clinical PET machines.
- In Chapter II, we will detail, 2D/3D acquisition methods in PET to record the data in an ideal format for reconstruction. In addition we will describe 2D and 3D reconstruction techniques. It is not a question here to make a complete and exhaustive review of the reconstruction techniques used in PET but to present the main methods, in particular those used for the images reconstruction. The various Data correction methods which make possible the optimization of images quantification are described in this chapter.
Chapter III presents the principles of Monte Carlo simulations that explain the fundamentals of Monte Carlo simulations developed in nuclear medicine and especially in PET. In addition, this chapter describes the platform of GATE simulation package, the parallelization techniques of Monte Carlo simulation for PET, the processing on the computing grid and briefly the reconstruction algorithm of STIR code which will be the basis of this work.
In the chapter IV, we present, the validation of a clinical PET called ECAT EXACT HR+ using GATE. The validation is done according the NEMA NU 2-2012 protocol[6]. On the other hand, we present a study of the effect of changing the CTW and dead time model on the Count Rate performance. An additional work focusing on the Siemens $Biograph^{TM}$ mCT 20 Excel PET/CT scanner will be presented in this chapter. First, we addressed the validation of GATE V7.1 simulation code according to the NEMA NU 2-2012 protocol [6]. The results were compared to the experimental data. Second, we studied the effect of the coincidence time window and the block gap and inter-crystal gap on the count rate and spatial resolution. The scanner $Biograph^{TM}$ mCT 20 Excel scanner is validated using GATE is used to perform the image quality, accuracy of attenuation ,and scatter correction using the NEMA/IEC body phantom simulated using GATE [6]. The output of these simulation is used to generate a sinogram that is used as input to Software for Tomographic Image Reconstruction (STIR) to reconstruct the image and correct the attenuation effect. We then use matlab code to calculate the contrast and the background variability also the lung insert relative errors. Other work presented in this chapter addresses the validation of the $Biograph^{TM}$ True point (with True V option) using GATE according to the NEMA protocol[6].

Chapter 1

Positron Emission Tomography Principle

1.1 Introduction

Positron emission tomography (PET), is a technique that uses radioactive emitters as tracers. The imaging of the tracers distribution is made possible with the use of tomographic imaging techniques (Chapter 2) applied to the data resulting from detection of the two photons emitted by the e+/ e- annihilation. In this chapter, we begin with the physics principles behind the PET techniques, the signals processing of PET scan, and their characteristics. Then, we will discuss its limitations which can alter the quantitative analysis of the image. Finally, we present the stat of the art of a different PET system.

1.2 Positron Emission Tomography

Positron emission tomography (PET) is a medical diagnostic method for cancers based on 3D-distribution of radio-tracer in the target organ. The radioactive elements most used in the PET exam are Fluorine 18 (^{18}F), Rubidium 82 (^{82}Rb), and the least used, Carbon 11 (^{11}C) Oxygen 15 (^{15}O) and Nitrogen 13 (^{13}N). They are produced by a cyclotron and are distinguished in particular by their radioactive period and by their average path in the material. These radio-tracers (^{11}C, ^{13}N, ^{15}O, ^{18}F, etc.) are used to mark compounds of biological interest. The radio-tracer is injected in the patient's body distributed in fabrics according to its biochemical properties. The concentration required by radio-tracers can be extremely low around to 10^{-9} mol, contrary to the technical of radio-graphic or magnetic which require concentrations much higher, in the range of 10^{-3} mol. These radioisotopes rich in protons, convert a proton into neutron through the weak interaction, with the emission of a β^+ particle (a positron) and a neutrino. After a short path in the patient, these positrons annihilate with electrons of the medium to produce two back to back 511 keV photons, which are detected in coincidence by the PET detectors[1, 2]. The Coincidence detection of gamma rays, which are very penetrating and can escape the detector, the reconstruction of the annihilation events location using analytical or statistical methods establishes the PET system basics. The result of the reconstruction process is a 3D image, where the signal intensity in a voxel of a particular image is proportional to the radionuclide quantity in this voxel. The concentration of radio-marked molecules in the tissue measured according to the time using a

temporal sequence of images. Also, a mathematical modeling is used to determine the specific biological processes.

1.2.1 radio-tracers production

- **radio-isotopes production**
  The main isotopes used in PET are: (^{11}C), (^{15}O), and (^{13}N) three isotopes of fundamental atoms consisting the living matter (carbon, hydrogen, oxygen and nitrogen). Halogens such as (^{18}F) or(^{76}Br) can also be incorporated into molecules without altering their biological properties.
  These isotopes are produced by nuclear reactions using charged particles (e.g. proton , deuteron, α particle, H^-, D^-) accelerated with the application of electromagnetic fields in cyclotron accelerators Figure 1.1 . The energies and intensities necessary for the medical use are low, allowing smaller cyclotrons size and to have machines specifically dedicated to nuclear medicine.

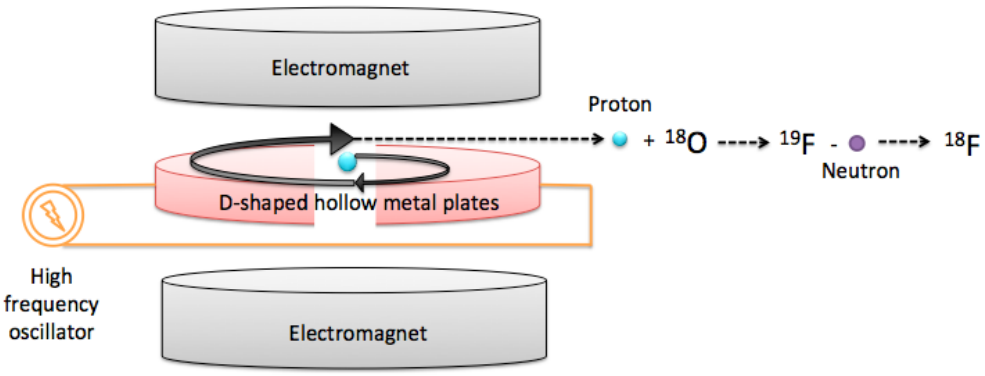

FIGURE 1.1: Synthesis of ^{18}F in a cyclotron. A proton is radially accelerated using D-shaped plates with alternating charges, and then deflected towards an 18-Oxygen (^{18}O) atom. This produces the 19-Fluorine atom (^{19}F), which loses a neutron to become the 18- Fluorine atom (^{18}F) of interest

The Cyclotrons accelerate the charged particles (e.g. proton , deuteron, α particle, H^-, D^-) to obtain a particle beam having a high kinetic energy. The incidental particles that reached the required energy hit then a target material, according to the desired nuclear reaction. The production of every radionuclide depends on the beam energy, the target material quantity (Various target materials are used, in the case of the fluorine 18 (^{18}F) and the nitrogen 13 (^{13}N); the target material is the water which was enriched by the isotope oxygen 18 (^{18}O). The carbon 11 (^{11}C) and the oxygen 15 (^{15}O) are produced from targets of gas nitrogen), the cross section of the reaction and the target bombardment time. The essential parameters for the radio-elements production of high purity radio-chemical and radio-nucleic are the control of the incident particles energy, the choice and the purity of the target material so that the conception

of the target (geometry, materials)[7].
For the production of isotopes previously mentioned, the beams intensity is between 50μA and 70 μA for energies ranging from 8 MeV to 20 MeV. While the previous generations of cyclotrons were accelerating positive ions most of the time, current machines accelerates negative charged particles H^- , D^- or positive ones(e.g. proton, deuteron, α particle). Cyclotron using negative ions have a low internal activation and allow the separation into two beam to bombard simultaneously two different targets. Table 1.1 shows the production reactions for the main isotopes used in PET.

TABLE 1.1: Examples of some classic reactions of radio-isotopes production

Radio-element	element target	Energies and type of incident particle	Reaction of production	Half life of radio-element
^{11}C		p-16MeV	$^{11}B(p,n)^{11}C$	20.4 min
	CO_2	p-16MeV	$^{12}C(p,d)^{11}C$	
^{13}N	H_2O	p-16MeV	$^{16}O(p,\alpha)^{13}N$	10 min
	$^{14}N_2$	p-16MeV	$^{14}N(p,pn)^{13}N$	
^{15}O	H_2O	p-16MeV	$^{16}O(p,pn^{15}O$	2 min
	$^{15}N_2$	p-16MeV	$^{15}N(p,pn)^{15}O$	
^{18}F	^{20}Ne	d-8MeV	$^{20}Ne(d,\alpha)^{18}F$	110 min
	$H_2{}^{18}O$	p-16MeV	$^{18}O(p,n)^{18}F$	

Currently, The ^{18}F is the most used isotope in TEP. It allows to mark the fluoro-deoxy-glucose, 2-[^{18}F]fluoro-2-deoxy-D-glucose](FDG) which represents 90 % of radio-pharmaceuticals used in PET. The production of ^{18}F is realized according to reactions:

The reaction $^{20}Ne(d,\alpha)^{18}F$ produce the fluorine $[^{18}F]F_2$. A one hour irradiation by a deuteron beam of 8 MeV and 20 μA of intensity, allows to obtain approximately 7.5 GBq of $[^{18}F]F_2$. The water enriched in oxygen 18 (^{18}O) (usually enriched from 97 to 99 % by (^{18}O)) used to produce $[^{18}F]$ according to the reaction $^{18}O(p,n)^{18}F$. The obtained fluorine is in ^{18}F-Fluoride form. It is recovered by trapping an ion exchange resin. A one hour irradiation by protons of 16 MeV and 20 μA of intensity allows producing at least 1 Ci of ^{18}F. Actually this reaction is the most used. If the enrichment of water by ^{18}O is lower, more ^{13}N is produced from the nuclear reaction $^{16}O(p,\alpha)^{13}N$. Therefore some potential problems of radionuclide contamination appear in the finished FDG. The enriched water can be collected after irradiation and cleaned for re-use. Most installations use only the water once, then discard or return them for reprocessing by the manufacturer.

- **radio-synthesis**
  The radio-synthesis allows marking a biological compound by a beta emitting isotope. The $[^{18}F]$ – Fluoro-2-Deoxy-D-Glucose (Figure 1.2 right) is the most widely used radio-tracer.

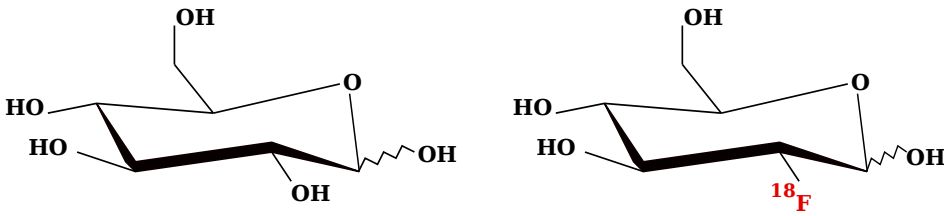

FIGURE 1.2: molecule D-Glucose (left) , [^{18}F] -Fluoro-2-Deoxy-D-Glucose (rihgt).

These radio-tracer [^{18}F]FDG is structurally a glucose analog. The various radio-syntheses aim at introducing the radioactive Fluorine-18 atom instead of grouping hydroxylate on a carbon in the second position of the molecule of D-glucose (Figure 1.2 left). The hydroxide groups of the other positions will be masked and protected by an acetyl group. In order to avoid interference with the synthesis. This operation is classic and perfectly mastered in sugar chemistry[8].

1.2.2 The different radio-tracers used in PET

The reconstruction of organ's three-dimensional images to be studied by PET, based on the 3D-distribution of the radio-tracers, are obtained by the incorporation of organic molecules and radio-nucleus beta-emitting (Carbon 11 ^{11}C, Fluorine 18 [^{18}F]) and are injected into patient's body. This technique requires to understand the in-vivo biological processes (the study of the bio-distribution, the metabolism and the elimination of chemical entities).
Most tissues use free fatty acids to meet their energy needs. The brain always uses glucose as a substrate, as well as many other cells sometimes use glucose. In oncology, [^{18}F]-FDG is used as a tracer of regional glucose consumption for the cancerous tumors diagnosis. while in cardiology, it is used to identify the patients at risk from a myocardial revascularization after an infarctus. In neurology, the same tracer is used to estimate the epileptic patients susceptible to benefit from a surgery, or to help in the early diagnosis of neuro-degenerative diseases (Alzheimer's disease, Parkinson).
Here are some examples of radio-tracers most used in PET[9].

- The [^{18}F] FDG used to monitor the glucose metabolism in pathology such as epilepsy, degeneration or cardiac involvement, cancer tumors.
- The [^{18}F] FluoroDOPA is used to monitor the dopamine synthesis in the cerebral cores that control movement and is used in studies of Parkinson's disease and in neuroendocrine digestive tumors.
- The [^{18}F] NaF (sodium fluoride) has an excellent fixation at the skeleton, adapted to the osseous tumors study and different cancers osseous metastases.
- The [^{18}F] -fluorocholine: A very effective tracer for the imaging of diverse human brain tumours, the lung or the prostate.

- The $[^{18}F]$ -Fallypride: usually used for the imaging of the receivers of dopamine D_2/D_3.
- The $[^{18}F]$ allows the osseous image.
- The $[^{11}C]$Methionine is an amino-acid indicative of protein synthesis, used in PET for studies of tumor metabolism.
- The $[^{11}C]$ Raclopride used in the study the degenerative diseases of patients presenting disorders movement, for example in the Parkinson's disease.
- The $[^{11}C]$-Acetate: allows imaging the oxidative metabolism in the myocardium.
- The $[^{15}O]H_2O$ Water marked in the oxygen. It allows us to map the blood supply of the brain and the exploration of its functions, as well as to appreciate the tumors hypoxia degrees.
- The $[^{13}N]NH_3$ is captured by the myocardium. that used in cardiology as a tracer for the blood flow.
- The $[^{82}Rb]$: is used for Myocardial perfusion imaging.

1.2.3 Positron emission and annihilation with an electron

- **Positron emission**
  Positron emission is a form of unstable nuclei β disintegration with a protons excess. In this case, a proton is converted into a neutron through the weak interaction [10]. A β^+ particle (positron) and a neutrino are emitted as the following equation.

$$ {}^{1}_{1}\mathbf{P} \rightarrow {}^{1}_{0}\mathbf{n} + {}^{0}_{1}\mathbf{e}^{+} + \bar{\nu} \tag{1.1} $$

  The creation of nucleus son and the emission of positron and neutrino from a nucleus father according to isobaric transmutations (Z change, conservation of A) as shown in equation (1.2), this reaction takes place if the mass difference between the atom son ${}^{A}_{z-1}\mathbf{Y}'$ and the atom father ${}^{A}_{z}\mathbf{X}$ a is larger or equal to $2m_eC$.

$$ {}^{A}_{z}\mathbf{X} \rightarrow {}^{A}_{z-1}\mathbf{Y}' + {}^{0}_{1}\mathbf{e}^{+} + \bar{\nu} + Q \tag{1.2} $$

  Where e^+ is a positron, $\bar{\nu}$ is an electron anti-neutrino and Q is the energy released by transmutation, transferred to the reaction products as kinetic energy. For other transmutations, Electron Capture(CE) and β^+ are competitive reactions, CE represents the majority for heavy atoms (e.g ^{68}Ge) and β^+ in the majority for the light atoms (^{11}C, ^{13}N,^{15}O, ^{18}F). In PET, the β transition is of particular interest that explains why the majority of the used isotopes are light elements. Although Q is constant for a given β^+ transmutation reaction, it is randomly distributed between the e + positron and the anti-neutrino $\bar{\nu}$ (the positrons energy spectrum is therefore continuous). In PET, the ^{18}F is the most used radioisotope, The disintegration of ^{18}F obeys the following transformation:

$$ {}^{18}\mathbf{F} \rightarrow {}^{18}\mathbf{O} + \beta^{+} + \bar{\nu} \tag{1.3} $$

- **annihilation** e^+/e^-
  The emitting positron interacts with matter, and loses all its kinetic energy by multiple collisions. In this energy range, the positron energy is lost exclusively by ionization and excitation. Positrons can interact with atomic structures of much larger masses, resulting in high deviation for low energy loss. As a result, the positrons trajectory is a succession of small sections whose deflection angles can be very large. The positrons flight distance in the material is therefore always much less than the length of its trajectory. The calculation of the lost energy (equation (1.4)) during the positron - electron interactions was made by Möller:

$$\left[\frac{dE}{dx}\right] = \frac{2\pi e^4}{m_e c^2} NZ[2ln\frac{2m_e c^2}{I} + 3ln\gamma - 1 \cdot 95] \tag{1.4}$$

  Where: $\gamma = \frac{1}{\sqrt{1-\beta^2}}$, $\beta = \frac{v}{c}$.
  When the positron is thermalized (lost all its kinetic energy), it can combine with an electron to give a hydrogen atom known as positronium, a metastable element with a duration life less than 10^{-7} seconds. The e^+/e^- annihilation is a complete disintegration releasing an energy $2m_e c^2 = 1022keV$. In practice, the only allowed configuration associated with a non-negligible probability is the emission of two photons, Produced by annihilation e^+/e^- where e^+ and e^- are at rest. The two 511 keV photons annihilation are emitted at 180 ° from each other [10]. Figure 1.3 illustrates various steps from the emission of β^+ until its annihilation with an electron of the medium.

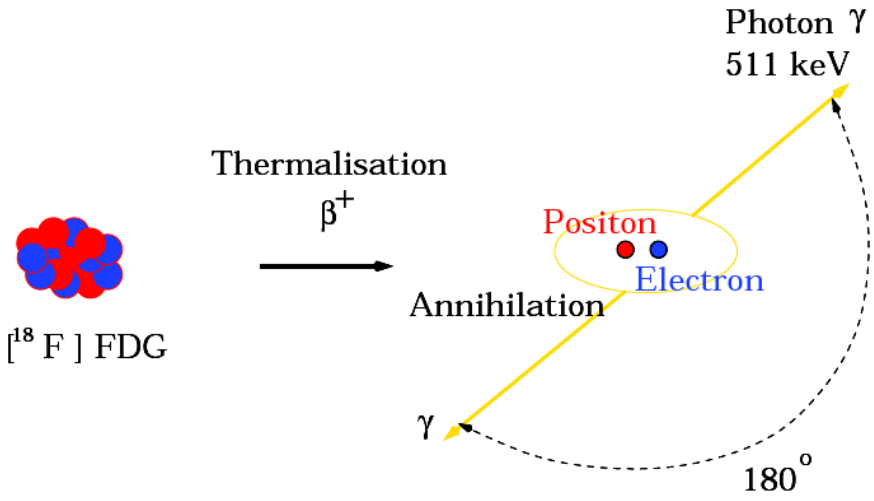

FIGURE 1.3: Disintegration of the positron emitting nucleus, emission, thermalization and annihilation of β^+ with electron and generation of two photons.

1.2.4 Non-linearity and positron range

There are two effects in PET imaging systems that produce errors in the determination of the response line from the positron emitting radionuclide location. These effects lead to a loss of spatial resolution and appear as a blur of the reconstructed images.
The first is the positron range. As shown in Figure 1.4, this effect come from the distance between the positron emission point and the place of its annihilation. The PET scan detects the annihilation photons that define the line in which it takes place, not the line on which the decomposition atom is located. Because positrons follow a tortuous path into the tissue before annihilation (direction change by multiple interactions with electrons). Then, the positron path is considerably longer than its positron range. In PET imaging, the positron range causes an uncertainty on the positioning of the event, which is the perpendicular distance from the emission position to the line defined by the annihilation photons. Some radionuclide emit higher positron energy than others, which makes the positron range effect depends on the radionuclide through its initial kinetic energy. For example: the ^{15}O emit a positrons with high energy Emax= 1.72 MeV compared to ^{18}F emits a positron of Emax=0.64 MeV. The PET positron range effect, varying from a few tenths of a millimeter to several millimeters, depends on the radionuclide and its Emax [9, 10].
The second effect is known as noncolinearity (figure 1.4) which states that the

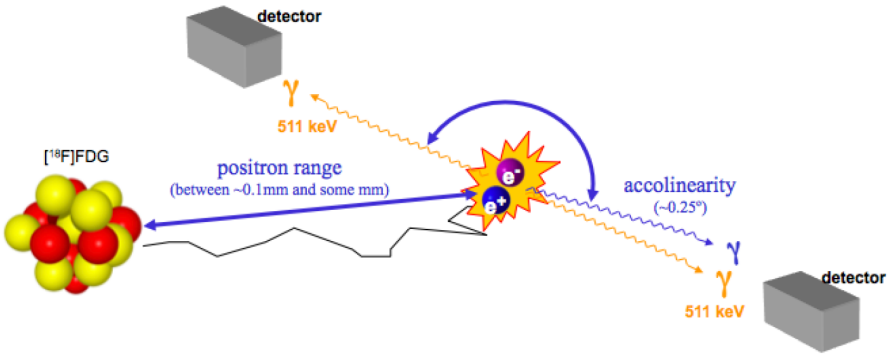

FIGURE 1.4: Positron range and photon non-linearity errors.

positron and the electron are not completely at rest when they annihilate. Then the annihilation photons will not be emitted exactly with 180° and will actually be emitted with an angular distribution about 180°. This effect is independent of radionuclide because the positrons must lose most of their energy before annihilation. Therefore, the initial energy is irrelevant. The distribution of the angles emitted is approximately Gaussian,with a Full Width at Half-Maximum (FWHM) of 0.5 ° (The two photons are actually emitted at 180° ± 0.25° from each other) [11, 12]. After detecting the annihilation photons, PET assumes that the emission was exactly back to back, which resulted in a small error in annihilation line location. Assuming a Gaussian distribution and using the fact that the angles are small, the blurring effect due to the noncolinearity can be estimated as follows:

$$\triangle_{nc} = 0.0022 \times D \tag{1.5}$$

Where D is the diameter of the PET scanner. The error increases linearly when the PET scanner diameter increases [10, 13].

1.2.5 Detection of gamma photons

The gamma annihilation detection is done mainly by the photons γ attenuation in scintillators coupled to PMT. For the 511 keV gamma photons, the only possible interactions between photons and matter are essentially: photoelectric effect, inelastic scattering or Compton effect, elastic scattering or Rayleigh effect [10, 11, 13]. The Pair production is not concerned in clinical nuclear medicine because it requires an energy threshold of $1.022MeV$ $(2 \times 0.511MeV)$ to create the two photons.
The total cross section attenuation of a 511 keV gamma in the material is given by:

$$\sigma_{total} = \sigma_{Photoelectric} + \sigma_{Compton} + \sigma_{Rayleigh} \tag{1.6}$$

All interactions leading to a loss energy cause the photon disappearance according to absorption in the matter.

$$I = I_0 e^{-\int_0^x \mu(x)\mathrm{d}x} \tag{1.7}$$

where, x is the medium-depth and μ is the linear attenuation coefficient. It represents the photon interaction probability per unit length and is expressed in cm^{-1}.
The linear attenuation coefficient and the interaction cross-section σ are linked by the relation

$$\frac{\mu}{\rho} = \frac{N_A}{A} \times \sigma \tag{1.8}$$

Where ρ represents the medium density (g/cm^3) , N_A Avogadro number $(atom/mol)$, A the atomic mass of the medium $(atom/mol)$, and σ the total cross section $(cm^2/atom)$.
The total absorption coefficient is given by:

$$\mu_{total} = \mu_{Photoelectric} + \mu_{Compton} + \mu_{Rayleigh} \tag{1.9}$$

where $\mu_{Photoelectric}$, $\mu_{Compton}$, $\mu_{Rayleigh}$ represent the linear attenuation coefficients corresponding to the photoelectric effect, the Compton and the Rayleigh effect, respectively.

1.2.5.1 Photoelectric Effect

The photoelectric effect is the ejection of an electron from the atom by an incident photon of energy $E_\gamma = h\nu$; Figure 1.5 illustrates this process. The atom and the outgoing electron absorbs all the photon energy and kinetic momentum. (The incident photon undergoes an interaction with an absorbing atom in which the photon completely disappears followed by the emission of a photo-electron with a photoelectric energy $E_i - El$, in which, E_i is the incident photon energy and E_l the electron binding energy capable of interacting with the incident photon).
The photo-electron is ejected by the atom from one of its layers (K or L). This electron leaves the atom with a kinetic energy equal to its binding inside the atom minus than the incident photon energy. the electron outer layer L fills the inner layer K and

emit a excess energy as X-ray characteristics called fluorescence photons or Auger electrons which carry the excitation energy. The probability of photoelectric absorption per depth distance unit depends strongly on the atomic number in which the photon propagates. The photoelectric effect is the dominant interaction in higher atomic numbers materials, such as lead (Z = 82) [9]. Moreover, the probability of photoelectric interaction increases resonantly when Ep approaches the electron binding energy [14]. There is no exact analytical formula for the photoelectric cross-

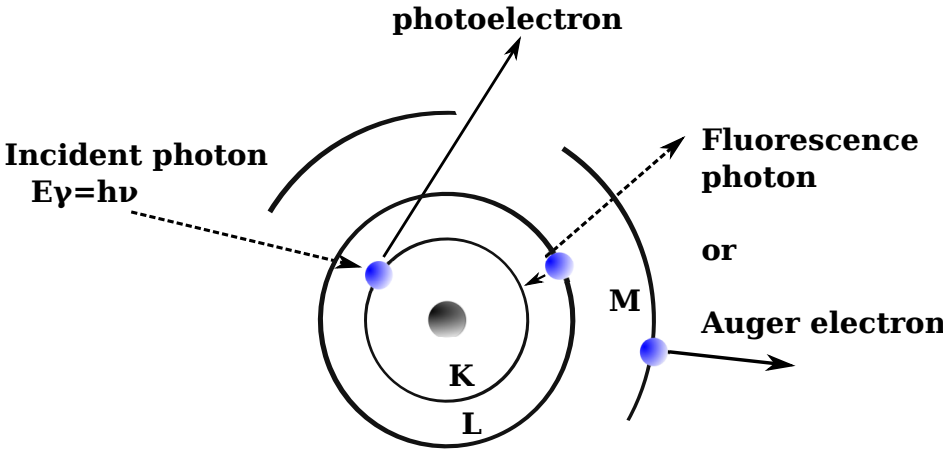

FIGURE 1.5: Graphical representation of the Photoelectric effect principle.

section as a function of incident photon energy. However an approximate formula often used valid outside the resonant peaks[15]:

$$\tau \propto \frac{z^5}{\mathbf{E}p^{3.5}} \tag{1.10}$$

Where Z is the atomic number.
The exponent n varies between 3 (low energies with respect to the binding energy of the layer K) and 5 (high energies) according to the incident photon energy. This formula indicates that the photoelectric effect is predominant at low energies and in dense medium.

1.2.5.2 Compton Effect

In Compton scattering, the incident photon transfers some of its energy to an outer layer or essentially a "free" electron, and eject it from the atom (Compton electron). The photon is released with an angle which can vary from about 0° to 180°(Figure 1.6). This angle depends on the amount of energy transferred from photon to electron. The conservation of the kinetic energy leads to a simple relationship between the original photon energy E_γ, the scattered photon energy E_c, and scattering angle θ :

$$E_c = \frac{m_e c^2}{\frac{m_e c^2}{E_\gamma} + 1 - \cos\theta} \tag{1.11}$$

In this equation, m_e is the electron mass and c the light speed ($2 \cdot 998 \times 10^8 m/s$). Using electron volt units for energy, the term $m_e c^2$ is equal to 511 keV. In PET, the incoming photon has an energy level of 511 keV, consequently Equation (1.11) further reduces:

$$E_c = \frac{511}{2 - \cos\theta} \tag{1.12}$$

The maximum energy transfered to electron occurs when the photon is dispersed by 180° equation (1.13). The Compton scattering probability per absorbing medium length unit is linearly proportional to the medium atomic number [9, 16] .

$$\mathbf{E}\gamma^{max} = E_\gamma - E_\theta(\theta = 180) = \frac{2 \times 511}{3} \tag{1.13}$$

The Compton scattering cross section of a photon and an electron is given by the Klein-Nishina formula:

$$\sigma_c{}^e = 2\pi r_e^2 [\frac{1+\varepsilon}{\varepsilon^2}(\frac{2(1+\varepsilon)}{1+2\varepsilon} - \frac{1}{\varepsilon} ln(1+2\varepsilon)) + \frac{1}{2\varepsilon} ln(1+2\varepsilon) + \frac{1+3\varepsilon}{1+2\varepsilon^2}] \tag{1.14}$$

where r_e the classic electron ray, $\varepsilon = \frac{E_\gamma}{m_e c^2}$

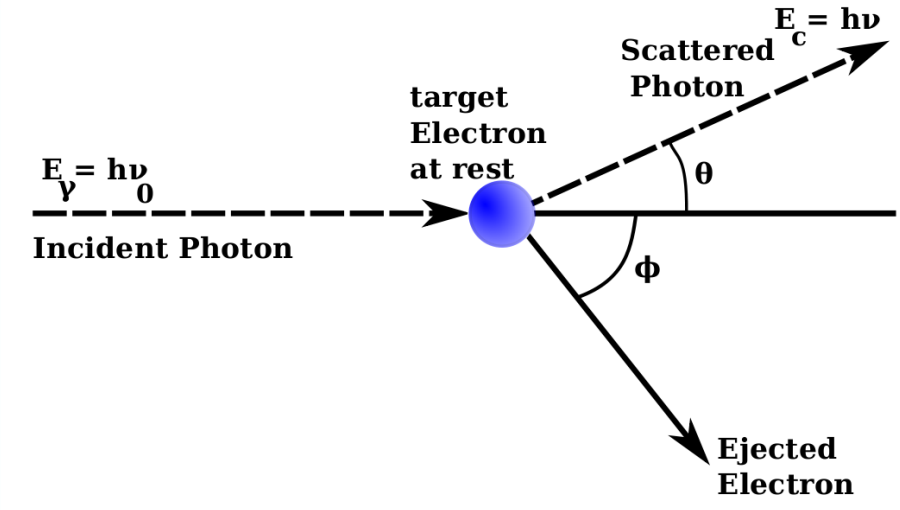

FIGURE 1.6: Gamma photon deviation with electron by Compton scattering.

The photons angular distribution in the solid angle $d\Omega$ around the relative direction θ to the incident photon direction is given by the differential cross section of Klein-Nischina equation [13]. It is independent on the diffusion medium but heavily dependent on the photons energy. Theoretically, Klein-Nishina equation is expressed as:

$$\frac{d\sigma_c}{d\Omega} = r_e^2 [\frac{1}{1+\varepsilon(1-\cos\theta)}]^2 [\frac{1+\cos^2\theta}{2}][1 + \frac{\varepsilon^2(1-\cos\theta)^2}{(1+\cos^2\theta)[1+\varepsilon(1-\cos\theta)]}] \tag{1.15}$$

1.2.5.3 Elastic scattering (Rayleigh Effect)

The Rayleigh effect states that a low energy photon has its trajectory deviated while passing near an electron which is strongly linked to an atom. This effect can be achieved in case of incident energies lower than the electron binding energy in the internal orbital layers. The photon energy transferred to the atom is considered negligible. Since the atom is heavier than the electron, the energy scattered in this case is very close to the incident energy and the Rayleigh scattering is essentially an elastic scattering. The distribution of deviation angle is very different from the Klein-Nishina distribution (equation (1.14)) because all the electrons in the layers strongly linked to nucleus and coherently to the Rayleigh diffusion process [3, 13]. As the Compton and photoelectric cross sections are higher around the 511 keV Rayleigh scattering cross section in biological tissues, the influence of the Rayleigh effect on the annihilation photons detected in PET is low, indicating that this effect is not significant in PET.

1.3 γ Coincidence Detection and Electronic Collimation

1.3.1 γ Coincidence Detection

The coincidence detection of 511 keV annihilation photons requires a detection system that is sensitive to the relatively high photon energy to make it possible to determine precisely the energy of each photon detected with a high counting rate. The PET system consists of crystal rings, separated by lead or tungsten Septa(2D mode) used to reduce the number of Scattered coincidences and Random ones in the data (axial collimation); only small axial tilt of coincidences are detected [10, 11, 13]. Contrary to 3D mode (no septa used), all coincidences are detected independently of their axial tilt as shown in Figure 1.7.

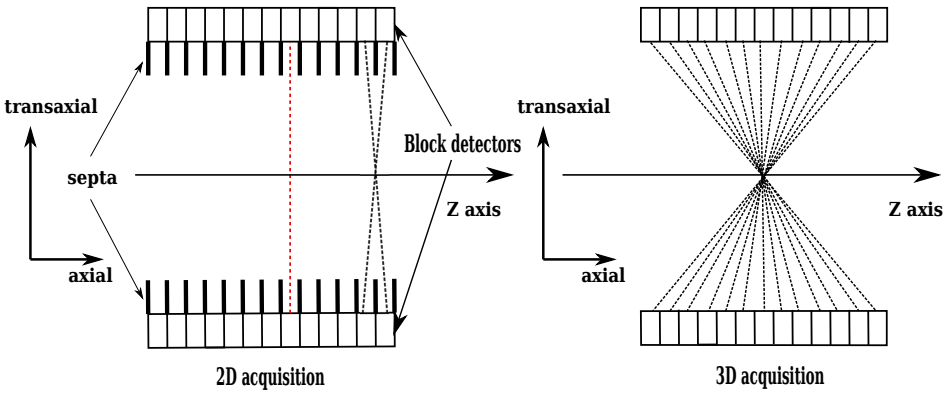

FIGURE 1.7: 2D (axial collimation) and 3D acquisition modes (no axial collimation) of a PET scanner.

The individual detector contains either several large segmented crystals or a collection of small crystals. The most used detection system consists of several scintillator crystals coupled to one or more photomultiplier tubes (PMT). All incoming photons in the detection chain are analyzed individually. They lose some or all of their

energy by interacting with the electrons of the crystal that will excite other electrons and generate scintillation mechanisms. The light energy thus created, proportional to the energy deposited in the crystal, will then be directed to the photo-cathode of the PMT through an optical guide. An electrical pulse is proportional to light energy, will appear at the anode of the PMT and will be processed by the following acquisition electronics system:

- The amplification, the shaping, the energy discrimination and the localization through the detection chains more or less integrated in PET according to the PET system detectors' architecture design.

- The time discrimination is based on a coincidence circuit that only allows the event recording if two photons are detected on two detectors opposite to each other in a time windows of a few nanoseconds (coincidence Time window). In ideal case, only the disintegration between the two detectors can contribute to the counting. The elementary volume assimilated to a response line (LOR) carried by these two detectors determines the direction of two photons γ annihilation emission (electronic collimation). Figure 1.8

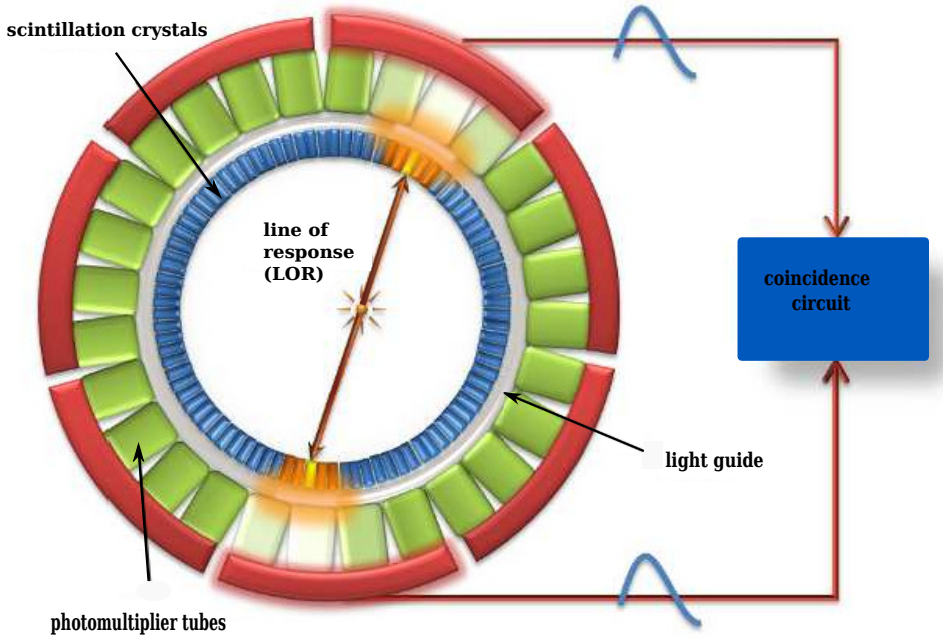

FIGURE 1.8: photons Coincidence detection of PET

1.3.2 PET detection chain

1.3.2.1 Scintillators

The sensitivity, spatial resolution, energy and time resolution, manufacturing constraints and the cost are the basis to choose a scintillator. The recent PET scintillators developments lead to different solutions. The detection system performance

depend on the choice of the scintillator crystal that ideally corresponds to the following characteristics: High Stopping Power coupled with high fraction photon, resulting in high atomic number and high density, High light conversion efficiency (photons / keV), the emission should be compatible with the photo-detectors, Fast Emission (A low decay constant thus allowing a good temporal resolution of the detection system and decreasing dead time relative to the scintillation), transparent for its emission wavelength, refraction index is close to that of glass (1.5) in order to ensure an optimal transfer of visible photons in the photomultiplier tubes, non-hygroscopic, insensitive to temperature, and finally easy to manufacture in dimensions to build a detector and Low manufacturing cost.
Table 1.2 presents the characteristics of the main PET scintillators [3].

TABLE 1.2: Characteristics of the main scintillators used in PET

Crystal	NaI(Tl)	BGO $Bi_4(GeO_4)_3$	LSO $Lu_2(SiO_4)O:Ce$	GSO $Gd_2(SiO_4)O:Ce$	LYSO $Lu_{1.8}Y_{0.2}(SiO_4)O:Ce$	LuAP $Lu(AlO_3):Ce$
Density	3.67	7.35	7.13	6.76	7.1	8.3
Z effectif	50	73	65	58	64	64.9
μ at 511 KeV (cm^{-1})	0.38	0.90	0.8	0.8	0.83	0.91
Percentage Photo-pic	18	44	34	26	-	-
λ emission max. (nm)	410	480	420	440	420	365
Refractive index	1.85	2.15	1.82	1.85	1.81	-
Scintillation decay constant τd (ns)	230	300	42	60	40	17
Light intensity at 511 keV (photons/ns)	84	14	320	57	-	-
Hygroscopic	Oui	Non	Non	Non	Non	Non
Energy resolution at 511 keV ($\Delta E/E$)	10	16	12.4	19	11.5	-
luminous efficiency (photons/MeV)	38000	8000 to 10000	25000	8000 to 10000	30000	14000

1.3.2.2 Light Guide

The optical coupling between the crystals and the photo-multipliers Tubes (PMTs) is provided by a light guide. It is made of a material having a refractive index close

to crystal, a guide shape and thickness are carefully matched to the photo-cathode shape of the PMT in order to optimize the light transport to the PMT [17]. The light guide also helps to reduce the variations in light collection efficiency by the PMT. The light loss caused by dead spaces that do not cover the PMTs entrance face, which collects the light emitted in these dead spaces and directs it to PMT photo-cathode.

1.3.2.3 Tube Photomultiplier

The vast majority of commercial PET scanners use PMTs as a photon detector to convert scintillation light into an electrical signal. A typical photomultiplier tube is shown in Figure 1.9. A PMT consists of a series of dynodes (electrode) each of which is maintained at a higher voltage with a resistance chain. Each dynode is coated with emissive material in evacuated glass tube. The inner surface of the entrance window (the photo-cathode) is also coated with an emissive material [10, 11, 13].

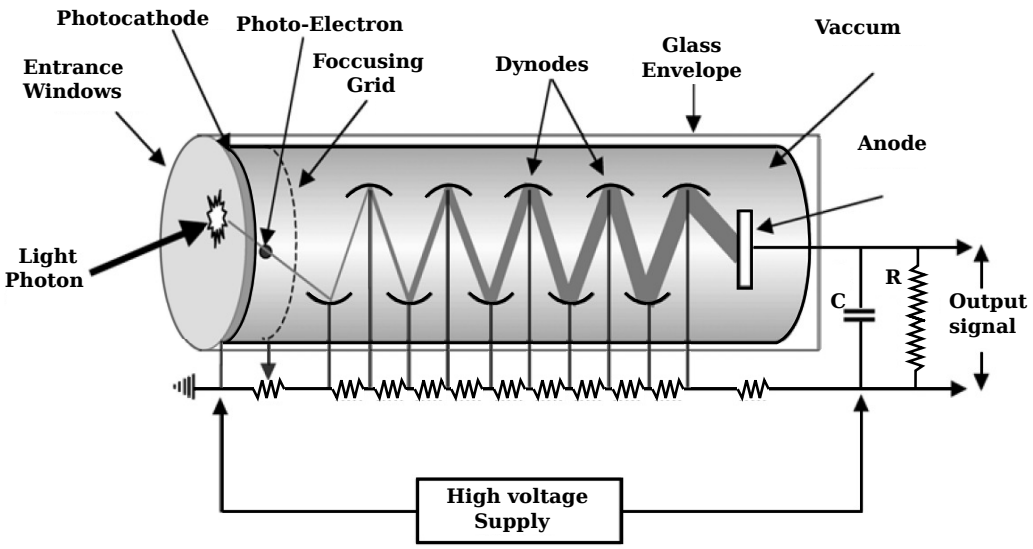

FIGURE 1.9: Diagram showing the main elements of a PMT.

The light photon coming from the scintillator is transmitted through the PMT glass entrance window and by photoelectric effect, the scintillation photons eject electrons from the photo-cathode (excites the photo-cathode). The photo-cathode is made from a thin layer of material(Bi-alkaline metal alloy) that can easily release electrons when the energy is deposited . Each photon has a probability about a 15% to 25% of producing a Photo-electron defining the quantum efficiency η of the photo-cathode. The focusing optic formed by a charged electrodes group is found between the photo-cathode and the multiplier to direct the photoelectrons towards the first dynode (positively charged electrode). The photoelectrons collection efficiency has to be as high as possible and the photoelectrons transit time from the photo-cathode to the first dynode must be independent of the photo-electron emission location. The multiplier is formed of dynodes (10 to 15 depending to the PMT) carried with higher electrical potentials. When an electron hits a dynode, it exerts its

energy to excite the electrons of the medium thus leading to an emitted secondary electrons on the order of 3 to 5 electrons from the dynode under normal conditions of use. These electrons are in turn accelerated to the second dynode and so forth, until creating an photo-electrons avalanche. After 10 amplification steps, each initial electron has created approximately 10^6 electrons, over a period of a few nanoseconds, which leads to a readily detectable current in the milliampere range (mA). Most PET scanners use round or square single-channel PMTs in the range of 1 to 5 cm in diameter. The advantages of PMTs are their high gain (amplification), which leads to their signal-to-noise pulses, stability, and fast response.

1.3.2.4 Electronic circuit

The electronic circuit, in the majority of current clinical PETs, is made of the following main parts:

- Signal energy discrimination: This step involves rejecting all low energy signals, considered as noise signals that saturate the electronics and contribute to the image noise[10, 11, 13].

- Analog-to-digital conversion: Each signal accepted during sorting at the discriminator level will be digitized individually, while keeping as information of the location, the energy and the signal detection time.

- Coincidence detection: Time discrimination is based on a coincidence circuit connecting two detectors opposite to each other, which permits the event registration only if the two photons are detected in a time window of a few nanoseconds (coincidence windows time: defines the time interval during which two photons are identified as forming a pair, called coincidence. Each pair including 2 photons supposed to come from the same annihilation). Thus, only the disintegration between the two detectors can theoretically contribute to the counting. The Figure 1.10 shows an implementation where by each timing signal opens a gate of duration τ ; if gates on two channels are open at the same time, a coincidence is recorded. If there is a timing signal on channel i at time T, there will be a coincidence on the relevant line-of-response L_{ij} if there is a timing signal on channel j at any time between $T - \tau$ and $T + \tau$. Therefore, the total time during which a coincidence may be recorded with the event on channel i (the coincidence time window) is 2τ [18].

- The calculation of the events location and energy: for each event of the coincidence chain, we have the position of the PMT and the energy deposited by each of them. The event location is calculated as the gravity center of these PMTs weighted by the energy deposited in each of them.

$$X_G = \frac{\sum_i X_i E_i}{\sum_i E_i}, Y_G = \frac{\sum_i Y_i E_i}{\sum_i E_i}, Z_G = \frac{\sum_i Z_i E_i}{\sum_i E_i} \tag{1.16}$$

  Where, X_i and Y_i respectively represent the transverse and axial coordinates of the PMTs in the scanners, each weighted by an energy E_i. X_G and Y_G Represent respectively the transverse and axial coordinates of the scintillation gravity

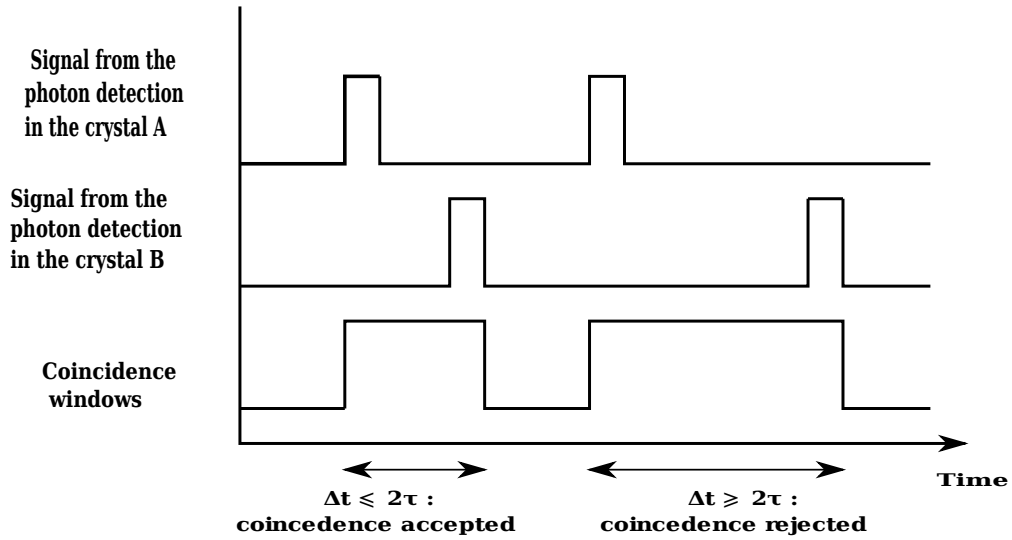

FIGURE 1.10: Principle of the coincidence time window.

center. The event energy is the sum of the deposited energy in each PMTs. $E = \sum_i E_i$

1.4 Limitations of PET systems

1.4.1 Limits of the architecture in detector blocks

Most PET detectors are designed in the same way. The detection modules are composed of inorganic scintillating crystal block, cut into elementary detectors, each group of crystals typically coupled to photo-multipliers (figure 1.11). The crystal convert the γ-radiation into a less energetic light radiation. The photo-multipliers collect the visible light energy and transform it into an electrical signal enable decoding the energy and identify the photon γ location.

1.4.1.1 Detector ring

The PET is a detector blocks assembly. These detector blocks , are a 2D array of crystals are attached to PMTs via a light guide and arranged in a ring around a tomographic axis. In some PET scanners, several crowns are aligned to form a larger cylinder. On the other hand, in rare cases, the blocks outer rings can be tilted and aligned in a spherical shape. By placing a source of radioactivity inside these rings, signals are detected from the source [13].

1.4.1.2 Shielding

The PET scan generally has ring-shaped shields, juxtaposed to the ring limits to avoid any contamination γ photons coming from the outside of the PET ring. These

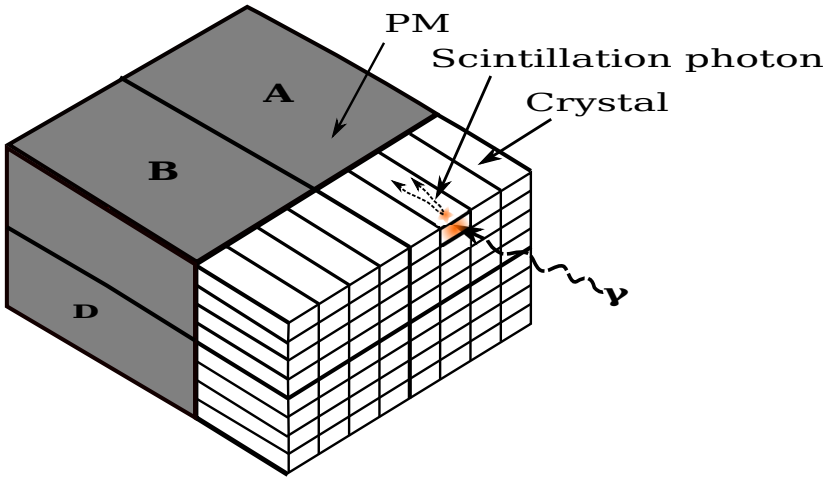

FIGURE 1.11: Scheme of a detection module, consisting of a scintillator crystal block and 4 photomultipliers.

shields are made of materials with high atomic number to maximize the probabilities of photo-electric interaction and thus stop the photons. Very often, lead is used. Tungsten and gold are more efficient but more expensive.

1.4.1.3 Dead time

The detector blocks systems composed by the crystals having a no null response time and PMTs with response depending on the Electronic chain. These components have a limited events analyze processing. The electronics chain will have a finite maximum rate at which it can process data, with typical maximum rates for pulse-processing electronics being around 1 MHz. It means that some events will be missed. In addition, for some time after detection, the PMT or detector block will not detect any interaction. When light pulses from separate photon interactions overlap to a significant extent, only one pulse will be measured by the PMTs. Since nuclear decay is a random process, there will always be a finite probability that some events will occur too close together to be distinguished even at very low average count-rates. At high count-rates, such losses can become very significant. These losses are known as dead-time losses. There are two types of dead time: the first is absolutely nothing happening (non-paralyzing dead time) – in the second each interaction prolongs the dead time of the same duration (paralyzing dead time)[13]. Those dead time types explained in detail in the section 1.4.3.

1.4.1.4 Energy resolution

The crystals used in PET have a limited energy resolution and can detect energy only with a finite precision [10, 11, 13]. The energies measured distribution of photons of energy E follow a Gaussian shape centered on E and characterized by its FWHM, defining the energy resolution. This depends on the material used and the energy E actually transfered by the photon γ in the crystal.

1.4.1.5 Depth of interaction

The most PET scans have a crystal much deeper (about 30 mm) their width ($<(6 \times 6mm^2)$). This architecture makes it possible to maximize the photon interaction in the crystals and thus to increase the sensitivity. The depth of interaction (DOI) can vary widely. It is not always possible to measure the DOI. However, some tomographs have a detector blocks composed of several layers of less deep crystals and made of different materials. The crystals composed by the different layers having different response times that one is able to discern, and obtain an estimated DOI with uncertainty value [19].

1.4.1.6 Pile up

The pile-up occurs when two photons from different annihilation interact quasi-simultaneously in the same crystal. The deposited energy is the sum of two photon energies, which will in general exceed the upper energy discriminator[13]. In this case, even the event is accepted with false energy deposited, or it is rejected because the energy associated with it is not compatible with the expected energy for an annihilation photon. In order to reduce the pulse pile-up at high count rate it is essential to use a scintillator with short decay time.

1.4.1.7 Photons scattering in the crystal

The γ -photons scattering in the crystals [20] is another error source. Indeed, when a photon arrives in the scintillators, it interacts with them by photoelectric effect or by Compton scattering effect. If this photon undergoes a Compton scattering, as a first interaction in the crystal, it will deposit some of its energy before changing direction and depositing some or all of its energy to another point of the same or another crystal. This induces a error location equivalent to the distance between the photon first interaction point in crystal and the barycenter of the light scintillation calculated electronically after the light signal reading by the photo-multipliers (figure 1.12).

1.4.1.8 Light sharing

The detector block is affected by light-sharing because the PMT is interfaced with several crystals, when the two γ -photons interact in different crystals but are associated with the same PMT [10, 11]. The different energy deposits are seen by the PMT as one interaction located is the weighted barycenter of these deposits. This results in loss of a detector block sensitivity as well as a poor positioning of the recorded interaction. This phenomenon also happens when a γ single photon interacts in several crystals at the same time.

1.4.2 Types of recorded events

1.4.2.1 Single Events

The singles events represent the vast majority (typically 90% or more) of photons detected by the PET scanners, among them only one of two annihilation photons is registered. The partner photon may be on a trajectory which does not intersect with

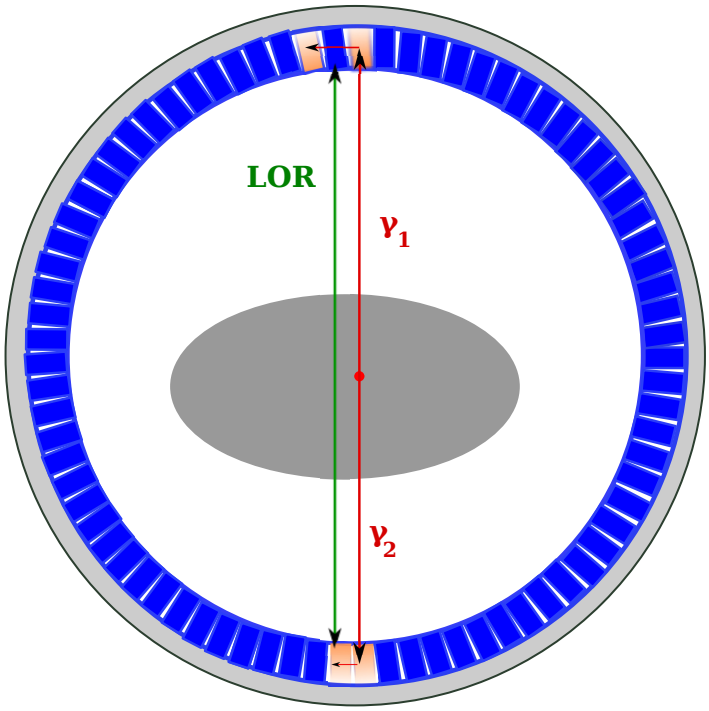

FIGURE 1.12: LOR location error due to photon Compton scattering in the crystals detector.

the detector, or the photon does not deposit sufficient energy (lower than the upper threshold of 511 keV) in a crystal detector. These single events are rejected by the PET scanner, but they are responsible for random and multiple coincidence events [11, 13].

1.4.2.2 Coincidence Events

The events recorded in PET contain coincidences directly coming from the annihilation photons, Called "true coincidences", which constitute the signal to be reconstructed. During the signal acquisition, three noise sources are added: the scattered coincidences, random coincidences and multiple coincidence [11, 13].

- **True coincidence:**
  The true coincidence results from two annihilation photons coming from the same disintegration without any interaction before being completely absorbed by PET detectors (Figure 1.13). True coincidences constitute the signal which contains the exact information of the radioactive distribution.

- **Scatter coincidences:**
  The scatter coincidence is related to the coincidence detection that's one or two annihilation-photons interacts with the scatter phantom or the bed-scanner before reaching the detector (Figure 1.13). These photons have an energy less than 511 keV and change their direction. Then Response Line (LOR) has a wrong direction. The recording of these scattered photons depends on the detector energy resolution, the choice of spectrometric acquisition window and

the shielding on PET camera either side, to avoid any events coming from outside the field of view (FOV).

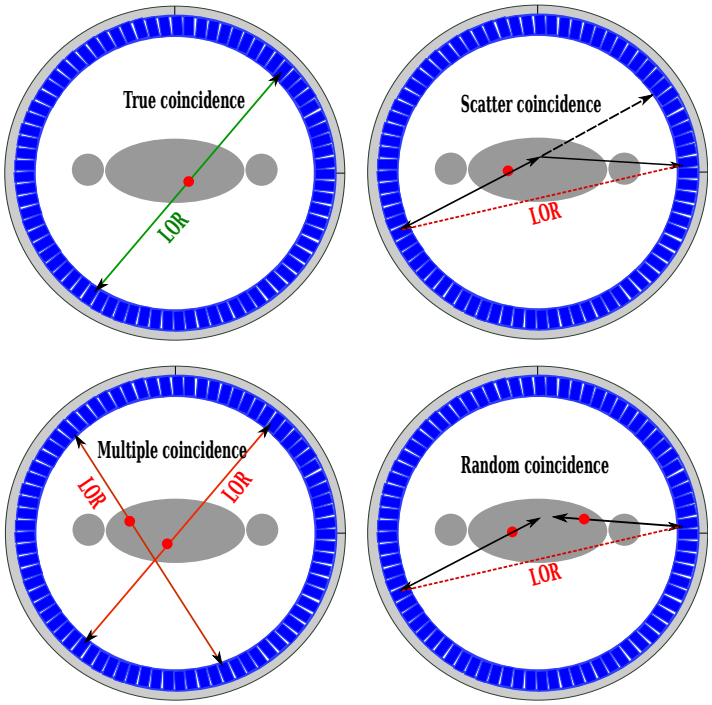

FIGURE 1.13: Illustration of the main coincidence event types in PET imaging shown on a single detector ring.

- **Random coincidence**
  The random event occurs when two photons coming from two independent annihilation events can be detected and registered within the same coincidence window time (Figure 1.13). The random coincidences number in a given LOR is closely linked to the single events rate measured by the detectors joined by that LOR and the random coincidences rate increase with the square of the activity in the FOV. This phenomenon degrades the image quality and reduces its contrast since it generates a bad radioactive concentration estimated in the analysis region.

- **Multiple coincidences:**
  If more than 2 photons are detected in the same time window coincidence, coming from several positron-electron annihilation, it is impossible to know on which response lines the annihilation took place. These multiple coincidences are shown in the (Figure 1.13). The simplest strategy for dealing these coincidences type is to reject them systematically.

1.4.3 Dead time

The PET detection chain will be saturated, for high radioactive concentrations.The resulting events are then lost. This phenomenon is called "dead time" [21, 11, 13].

There are two dead time types : Non-paralyzable dead time and paralyzable dead time.

1.4.3.1 Non-paralyzable dead time

Non-paralyzable dead time occurs when a particle arrives at a time t and the detector has dead time τ. The detector ignores any other particle arriving at time t_1 less than $t + \tau$. The count loss due to this effect is proportional to the particle flow hitting the detector and the time window t where the detector will be paralyzed[13]. The lost particles rate , defined by $(n - m)$, is expressed by equation 1.17.
Where, n is the particle flow rate arriving at the detector and m is the particle flow rate registered by the detector.

$$n - m = nm\tau \implies m = \frac{n}{1 + n\tau} \tag{1.17}$$

This case is illustrated on the top of Figure 1.14. For seven events, only three events are recorded.

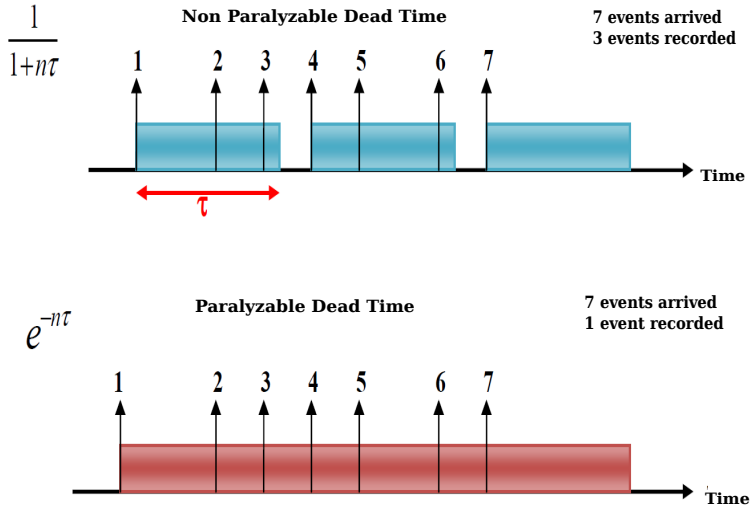

FIGURE 1.14: Counting events according to the two Dead time types.

1.4.3.2 Paralyzable dead time

In the case of paralyzable dead times, if a particle arriving at the detector during the time τ, subsequently with a second event occurs before this time, then a new period is launched where the detector is paralyzed again (the dead-time is extended by τ). This causes the subsequent events undetected. The paralyzable dead time is unable to provide a second output pulse unless there is a time interval equal to, at least the time resolution between the two successive true events. In this case, the relationship between the rate m of recorded events and the particle flow rate arriving at the detector n is explained by the equation 1.18:

$$m = ne^{-n\tau} \tag{1.18}$$

This case is illustrated on the lower part of Figure 1.14 where it can be seen that out of seven incident events, only one event is recorded.

The count difference between the two dead time types is shown in Figure 1.15.

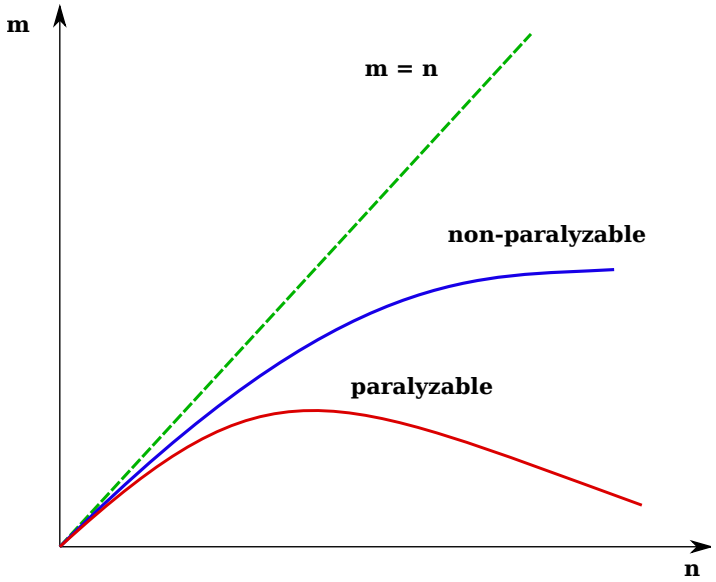

FIGURE 1.15: Count difference between two types of dead time (paralyzable and non-paralyzable)

For high counting rates, it is noted that for the paralyzed dead time the loss of events is greater than in the non-paralyzable case.

Finally at low activity $(n << (1/t))$, the two models give the same result on the losses related to the dead time:
In the non-paralyzable dead time case, the relationship between the rate m of recorded events and the particle flow rate arriving at the detector n is as shown in equation 1.19:

$$m = \frac{n}{1+n\tau} \simeq n(1-\tau) \tag{1.19}$$

In the paralyzable dead time model, the relationship between the rate m of recorded events and the particle flow rate arriving at the detector n is as shown in equation 1.20:

$$m = ne^{-n\tau} \simeq n(1-\tau) \tag{1.20}$$

In the detection chain, the sum of paralyzable and non-paralyzable dead time generates a paralyzable dead time.

1.4.4 Time of flight

On recent PET Scanner, it is possible measure the detection time of each single photons and determine the difference time between them forming a coincidence. This

information is called time of flight(TOF). It shows the annihilation position along the LOR. Since the two photons propagate with light speed C, the time difference between their arrival to the two detectors indicates the distance they have traveled $\Delta x = c\Delta t/2$, and thus the annihilation event location along the LOR between the two detectors (Figure 1.16).

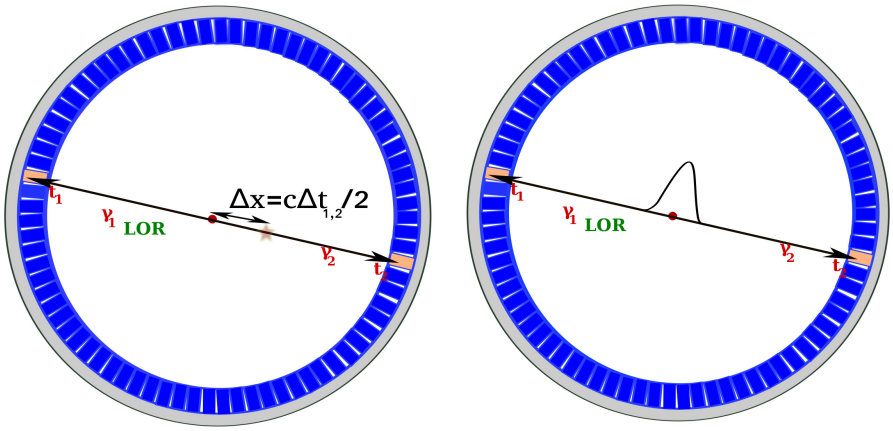

FIGURE 1.16: The estimated time-of-flight difference (Δt) between the arrival times of photons on both detectors in TOF-PET.

As same as the energy resolution, there is a time resolution characterizing the measurement inaccuracy. Its distribution is also estimated by a Gaussian centered on the exact value and FWHM defining the time resolution. This time resolution is determined by the different components involved in the detection process: the scintillator, the photomultiplier tubes, and the processing electronics. This technology, only integrated in the latest generations of clinical TOF-PET/CT systems, have a time of flight resolution in the range of 500–600 ps[22].

1.4.5 Field of view

The field of view is characterized by an axial dimension FOV_a defined by the number of rings, and the size of the crystals along this axis and transverse FOV_t determined by the acceptance angle of individual detectors in a PET scanner. Each detector is connected in coincidence with (N/2) detectors as many as half the total number of detector (N) in a ring and the data for each detector are acquired in a fan beam projection [9, 21]. All possible fan beam acquisition are made for all the detectors, which define the FOV as shown in Figure 1.17. Most current PET systems are whole-body systems, e.g., they have a typical transverse FOV between 60 cm and 70 cm. This FOV is adequate to handle the most patients. The axial FOV of most PET systems today is to approximately between 15-21.6 cm .

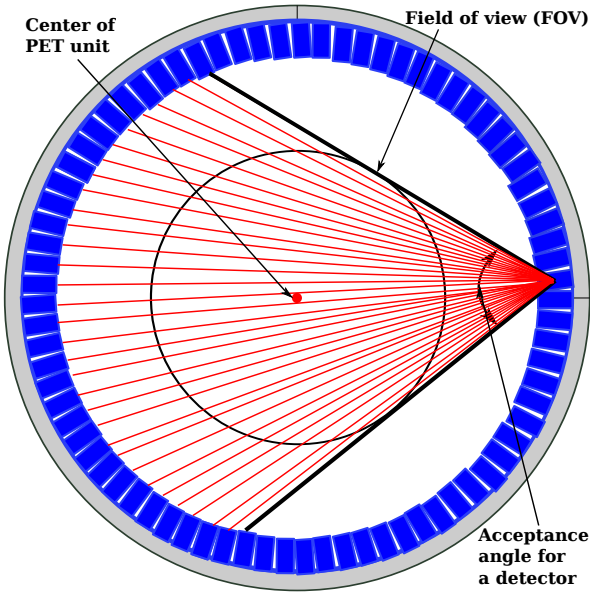

FIGURE 1.17: Transverse Field of View.

1.5 Data acquisition

There are two acquisition modes, 2D and fully 3D PET which are shown in Figure 1.18. The mode name only specifies the type of acquired data; both acquisition modes lead to 3D images [23, 24].

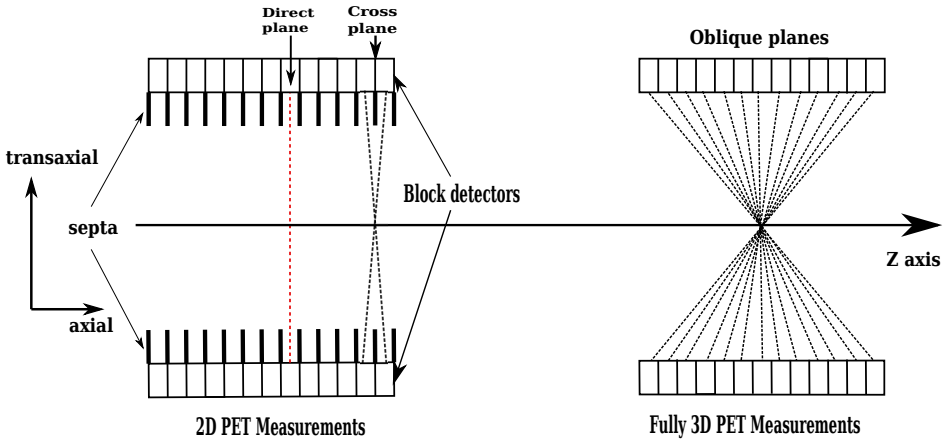

FIGURE 1.18: Comparison between 2D PET measurements and fully 3D. In 2D mode direct and cross planes (organized into direct planes) are collected, but in 3D mode all oblique planes are collected.

In 2D acquisition mode, an inter-plane of lead or tungsten septa is placed between detector rings as shown in Figure 1.18. These septas rings are used to improve resolution by reducing the number of scatter photons coming from outside the crystal's rings. Usually, the septa length is adjusted to accept the LoRs between detectors in the same ring and the LoRs between detectors in adjacent rings, so that axial data can still be combined in cross-planes. For the 2D PET, LoRs in a specific

imaging plane are considered and the volumetric image is reconstructed by repeating independently the 2D acquisition and reconstruction for multiple axial slices.
In the three-dimensional (3D) scanner, the septas are retracted, therefore any detector's ring can coincide with the other rings. Thus a direct LoRs as well as a LoRs located in oblique planes are acquired. The 3D mode allows to improve the detection sensitivity by a factor of 4 to 6 and reduces the statistical noise with respect to the influence of dead time, scattered events included in the data and the influence of radioactive sources located outside the FOV. Nevertheless, this 3D PET scan requires a huge storage capability and high computing performances. Despite the utility of 3D reconstruction methods, they are more complicated and need more computational time than 2D methods. Thus, several methods of data rebinning have been developed in order to reconstruct 3D data with 2D algorithms.

1.6 Storage data

1.6.1 List mode format

The List Mode Format(LMF) consists of recording a list of pairs photons detected in coincidence in a sequential mode. For each photon, the stored information is the two locations at which the annihilation photons interacted, deposited energy [13]. Therefore, this format result in a file of variable size, which increases with an increasing number of detection. Then, the data can be binned in histogram and reconstructed with conventional algorithms. Alternatively, iterative statistical algorithms that have been developed for list mode data can be used. This format only store the counts of coincidences number events detected by LOR during the acquisition. An array containing many line equal to possible LORs contains these values. This storage format is also used for singles, although it is not used in clinical practice.

1.6.2 Sinogram

The sinogram format is the only one allowing a visualization of the coincidence events. This format consist of space coordinates system, that's allowed to represent the response line contained in FOV scanner.

1.6.2.1 Two-dimensional sinogram

In 2D mode, only the LORS formed in crystals belonging to the same crown are used in the image reconstruction. The 2D sinogram associated with any transverse plane perpendicular to the axis detector is formed using the line of response in this plane which is characterized by two coordinates i.e. its distance x_r from the center of FOV, and its angular orientation Φ with respect to the horizontal axis (X axis) as shown in the Figure 1.19. The coincidences detected during 2D acquisition mode can be stored as a histogram contain the LORs. Each LOR is organized in a table with three entries thats contain the distance from the center x_r, angular orientation Φ and axial position z. Coincidence events in PET scanner are categorized by plotting each LOR as function of its angular orientation versus its displacement from center of FOV [13].

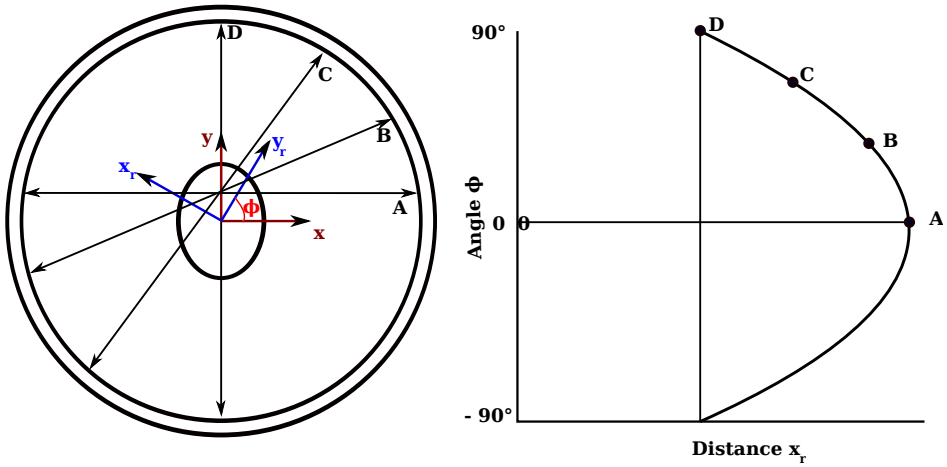

FIGURE 1.19: (left) A coordinate system for representing a 2D sinogram. Cartesian system (x,y) in red, and polar system (x_r, Φ) in blue. (Right) LOR as function of its angular orientation versus its displacement from center of FOV

The transition from the Cartesian system (x, y) to the cylindrical system (x_r, Φ) is given by the equation 1.21:

$$\begin{bmatrix} x \\ y \end{bmatrix} = \begin{bmatrix} \cos\Phi & -\sin\Phi \\ \sin\Phi & \cos\Phi \end{bmatrix} \begin{bmatrix} x_r \\ y_r \end{bmatrix} \tag{1.21}$$

The projection of a function $f(x, y)$ along a line with coordinates (x_r, Φ) and over a length y_r) is then written:

$$P(x_r, \Phi) = \int_{-\infty}^{+\infty} \mathrm{f}(x, y)\, \mathrm{d}y_r \tag{1.22}$$

This function $f(x, y)$ represents, the radioactive distribution in the transverse plane.
The set of projections given by equation 1.22 for all distances x_r and all angles Φ form the sinogram.
Projections are stored for $0 < \Phi < \pi$ being given the symmetry described by the equation 1.23:

$$P(x_r, \Phi + \pi) = P(-x_r, \Phi) \tag{1.23}$$

The projections $P(x_r, \Phi)$ correspond to the definition of the 2-dimensional Radon transform of $f(x, y)$.

1.6.2.2 Three-dimensional sinogram

In 3 dimensions (3D), the response lines are identified by their coordinates(Figure 1.20). These coordinates are linked to Cartesian coordinates by the following equation 1.24:

$$\begin{bmatrix} x \\ y \\ z \end{bmatrix} = \begin{bmatrix} -\sin\Phi & -\cos\Phi\sin\theta & \cos\Phi\cos\theta \\ \cos\Phi & -\sin\Phi\sin\theta & \sin\Phi\cos\theta \\ 0 & \cos\theta & \sin\theta \end{bmatrix} \begin{bmatrix} u \\ v \\ w \end{bmatrix} \tag{1.24}$$

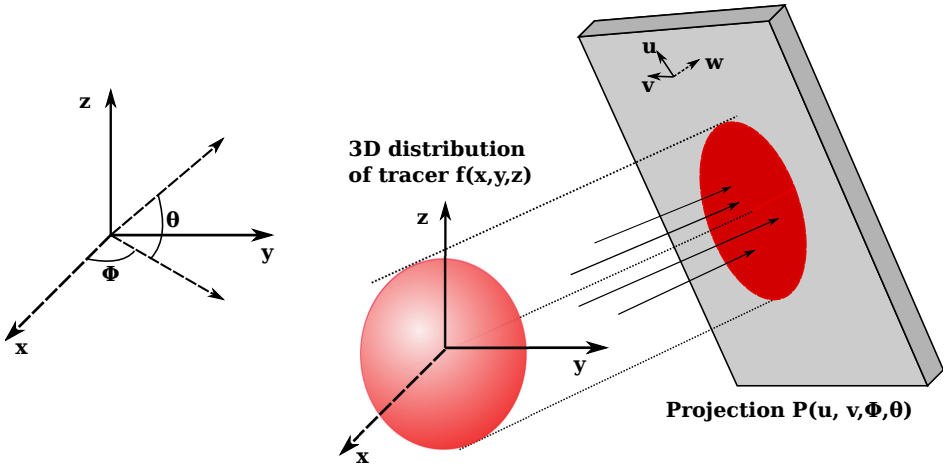

FIGURE 1.20: Definition of a 2D projection as the collection of all LORs having the same angles Φ and θ.

The 2D projections of the radioactive distribution $f(x,y,z)$ are computed in the perpendicular plane to the axis w by the equation 1.25:

$$P(u,v,\Phi,\theta) = \int_{-\infty}^{+\infty} \mathrm{f}(x,y,z)\,\mathrm{d}w \tag{1.25}$$

The sinograms containing these projections are indexed by the coordinates (v,Φ).

1.7 State of Art of Different Clinical PET scanner

The new-generation of commercial Combined PET/CT scanners considered a major development in nuclear medicine and play a major role in vivo imaging in oncology, neurology, cardiology, and psychiatry. There are several clinical PET/CT scanners mainly present in the current market offered by three companies as Philips, Siemens, and General Electric (GE). Table 1.3 gives a non-exhaustive list of the various machines currently in existence. The parameters presented in this table have been collected in the following references [4, 25, 26, 27, 28, 29, 30, 31, 32, 33].

1.8 Conclusion

In this chapter we have discussed the principles of positron emission tomography. Then we have presented the technological and physical limitations that may alter the quantitative analysis of the image. In addition to that the data acquisition types and their storages as well as the state of the art in PET scanner have been presented.

In the next chapter, we will present the different methods of image reconstruction and the correction methods available to correct physical and geometrical phenomena.

TABLE 1.3: Non-exhaustive list of different clinical PET / CT and there characteristics

Company	Philips		Siemens			General Electric	
Name of machine	Gemini GXL	Gemini TF	Biograph TruePoint (TrueV)	Biograph mCT	Biograph mCT Flow 64-4R	Discovery RX	Discovery 680
Crystals	17864	28336	24336 (32448)	24336 (32448)	32448	15120	13824
$Ring \times block$	1×28	1×28	3×48 (4×48)	3×48 (4×48	4×48	4×70	4×64
Crystal/block $(trasaxial \times axial)$	22×29	23×44	13×13	13×13	13×13	9×6	9×6
Size of crystals $(trans \times axial \times depth)$ (mm)	4×6×30	4×4×22	4×4×20	4×4×20	4×4×20	4·7×6·3×30	4·25×6·3×25
materials	GSO	LYSO	LSO	LSO	LSO	LYSO	LYSO
Ring diameter (mm)	820	900	842	842	842	886	818
FOV axial (mm)	180	180	162 (216)	162 (218)	221	157	157
Coincidence Windows (ns)	8	?	4·5	4·1	4·066	5·85	4·9
Energy windows(KeV)	410-465	440- ?	425-650	435-650	435-650	425-650	425-650
FWHM transverse resolution NEMA at 1 and 10 cm (mm)	$5{\cdot}5 - 5{\cdot}7$	$4{\cdot}8 - 5{\cdot}2$	$4{\cdot}1 - 4{\cdot}8$	$4{\cdot}3 - 4{\cdot}8$	$4 \cdot 4 - 4 \cdot 4$	$5 \cdot 0 - 5 \cdot 6$	$4 \cdot 9 - 5 \cdot 5$
FWHM Axial resolution NEMA at 1 and 10 cm (mm)	$5 \cdot 6 - 7 \cdot 5$	$4 \cdot 4 - 5 \cdot 3$	$4 \cdot 7 - 5 \cdot 7$	$4 \cdot 4 - 5 \cdot 8$	$4 \cdot 95 - 5 \cdot 9$	$5 \cdot 8 - 6 \cdot 5$	$5 \cdot 6 - 6 \cdot 3$
TOF (ps)	-	573	500	550	555	-	600

Chapter 2

Tomographic Image Reconstruction

2.1 Introduction

After photon detection in coincidence using the PET detectors and storing the output data, a new step is needed to obtain an image estimating the radio-activity distribution whithin the FOV. This step is called tomographic image reconstruction. It is done using high computer's performance because the methods used require a large number of operations. Therefore, this chapter is devoted to image reconstruction and is classified into three sections. The first section will be devoted to 2D/3D acquisition methods in PET to put the data in an ideal format for reconstruction. The second section will describe 2D and 3D reconstruction techniques. Doesn't make a complete and exhaustive review of the reconstruction techniques used in PET but to see which are the main methods and in particular those used for the image reconstruction. The third will be devoted to various Data correction methods which make the optimization of the image quantification possible.

2.2 2D - 3D acquisition in PET and correlation with reconstruction

Most PET scanner, dedicated to humans, have two acquisition modes. They use retractable collimators (called septa) of lead or tungsten [34], according to their acquisition mode. Septa are used only in the 2D acquisition mode. The acquisition type will set the reconstruction mode 2D or 3D. Irrespective of the acquisition mode, the image will give a volumetric information on the reconstructed object. In 3D mode, the PET sensitivity is greater due to a high solid angle.

2.2.1 2D acquisition and 2D reconstruction

The PET scanner have septa between detection rings to stop annihilation photons whose direction correspond to a high solid angle (Figure 2.1). This scanner, thus only validates the coincidences formed between two crystals belonging to the same ring (direct plane) or to two neighboring rings (crossed plane) (Figure 2.1); the output data is then acquired in 2D. The reconstruction is carried out in 2D for each of the 2N-1 plans (with N is the number of rings, there are N direct planes and N-1 crossed planes). The 2D images are then concatenated, or rearranged to form

a volume composed of 2N-1 cuts or less. The illustration of the image formed is shown at the right hand side of Figure 2.1.

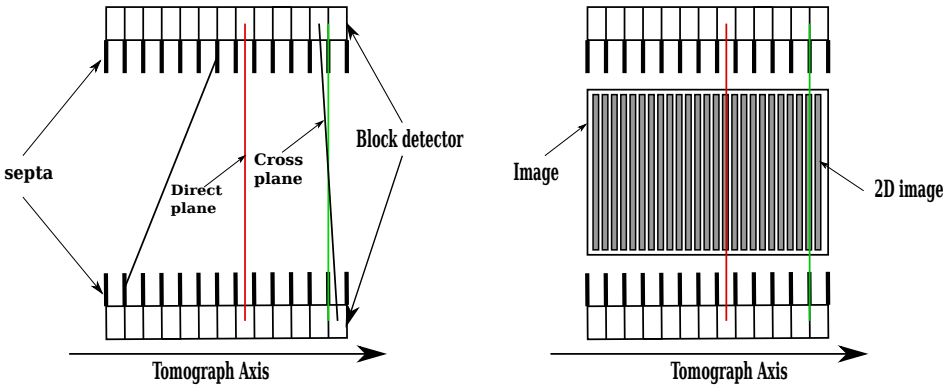

FIGURE 2.1: (Left) Illustration of a 2D acquisition for direct and crossed plans can form coincidences, pairs photons having a high solid angle are stopped by septa. (Right) Illustration of the 2D reconstruction from the direct and cross plans to form the image.

2.2.2 3D acquisition and 2D reconstruction ($2D_{1/2}$)

In the three-dimensional (3D) scan, any detector's ring can coincide with the other rings (Without septa). Thus a direct LoRs as well as LoRs located in cross planes crossing the direct plan are acquired and stored in 3D output Data. Moreover, 3D reconstruction methods are more complicated and demand high computing performances than 2D methods. The $2D_{1/2}$ reconstruction approach consists of rebinning the 3D data to be reconstructed using 2D reconstruction methods. There are different methods for rebinning data which have been developed in order to reconstruct 3D data with 2D algorithm, and also reducing the size of 3D data and minimizing the computing reconstruction time. The best known are Single Slice Rebinning (SSRB [35]), Multi Slice Rebinning (MSRB, [36]) and Fourier Rebinning (FORE,[37]). Since the scanner has no septa, data are acquired in 3D mode, with rebinning of the 3D data into standard 2D sinograms via SSRB algorithm. A cross LOR is associated with the plan located between the two axial positions of the crystals involved. Where z_1 and z_2 the axial coordinates of two rings associated with this LOR. Afterwards, the LOR is associated with the coordinate plan $\frac{(z_1+z_2)}{2}$ (Figure 2.2). The detector gaps lead to the missing sinogram regions. A threshold is often associated with this gap, in order to reject the LORs formed between two rings which has a high solid angle. This makes it possible to limit the bias provided by this rebinning. After rebinning, we proceed to the same reconstruction approach as for an acquisition 2D, starting from the set of sinograms corresponding to direct or crossed plans.

The FORE rebinning technique [38] is currently the most used for rebinning the data in the Fourier space more precisely, exploiting the frequency-distance principle in the ($2D_{1/2}$) reconstruction.

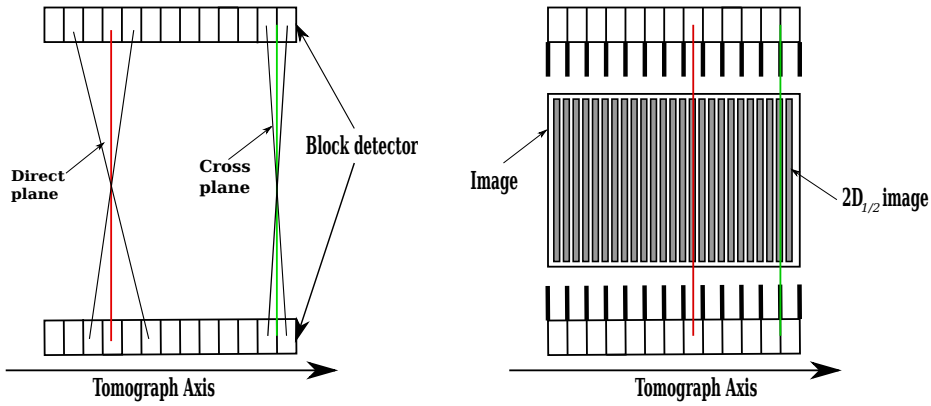

FIGURE 2.2: (Left)Illustration of a 3D acquisition when two crossed plans, formed a LOR between the two neighbor crystals involved in the coincidence. (right) Illustration of a 2D reconstruction for rebinning data

2.2.3 3D Acquisition and 3D reconstruction

In 3D acquisition, the PET septa are not used or retracted. Afterwards a direct plan constituted by LORs defined by two crystals belonging to the same ring, and cross plan are acquired. The 3D output data is used to reconstruct a 3D image (Figure 2.3). In order to reduce the number of possible LORs, a threshold should be set on the inclination of the cross plans as in the case of a $2D_{1/2}$ reconstruction. Finally, a single 3D image of the estimated radio-activity distribution in FOV, and the interpreted 2D images are deduced from this 3D image.

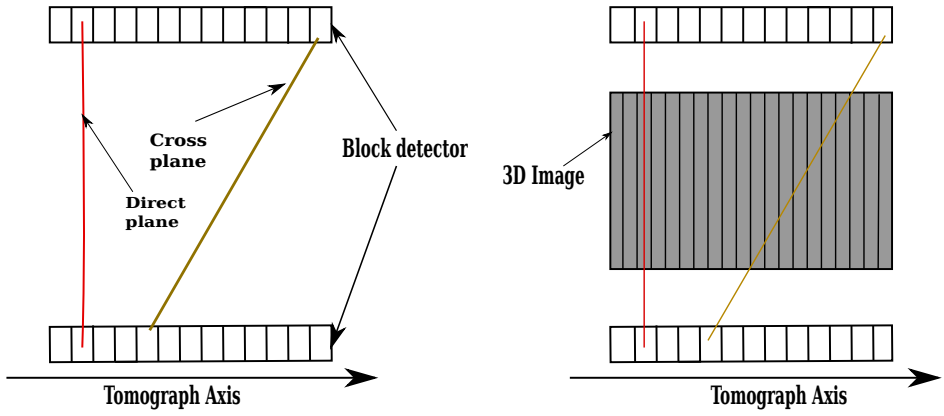

FIGURE 2.3: (Left) Illustration of a 3D acquisition in which all LORs belonging to direct and cross plans are recorded. (Right) Illustration of a 3D reconstruction where all the plans (direct and cross) are taken into account.

2.3 Reconstruction Methods

There are two basic image reconstruction approaches. The First approach is analytic which uses the mathematics of computed tomography to measure the linear integral of the activity distribution in the object. The second approach deals with the iterative methods to modulate the data collection process in a PET scanner and trying a series of successive iterations, to find the image that is most consistent with the measured data.
In the following section, we will detail different mathematical and algorithmic aspects associated with these image reconstruction principles in tomography.

2.3.1 Analytical Reconstruction Methods

2.3.1.1 Simple back-projection

The simple Back-projection is the first method which is used to obtain an estimated radio-activity distribution [39]. This method consists of back-projected projections measured from LOR acquired one by one without any other treatment. The sum of all back-projected views allows a final back-projected image. While back-projection is conceptually simple, it however provides very blurred images. Therefore, the Filtered back-projection is suggested to correct the blurred images.

2.3.1.2 2D Filtered Back-projection

The back-projection gives a blurred image of the estimated radio-tracer distribution f(x,y) in the FOV. Therefore, the Filtered Back Projection (FBP) is a proposed technique to correct the blurring in the image. This method uses the central section theorem to reduce these blurring by convolving the projection $P(x_r, \Phi)$ in the image space or by multiplying them with a ramp filter.
The Filtered Back Projection (FBP) method is applied to reconstruct the image following the steps given bellow:

According to the equation 1.22, the Fourier transform $P(v_{x_r}, \Phi)$ of the projections $P(x_r, \Phi)$ according to variable x_r is given by:

$$\begin{aligned} P(v_{x_r}, \Phi) &= \int_{-\infty}^{+\infty} \int_{-\infty}^{+\infty} \mathrm{P}(x_r, \Phi) e^{-2\pi j x_r v_{x_r}} \, \mathrm{d}x_r \\ &= \int_{-\infty}^{+\infty} \int_{-\infty}^{+\infty} \mathrm{f}(x, y) e^{-2\pi j x_r v_{x_r}} \, \mathrm{d}x_r dy_r \\ &= \int_{-\infty}^{+\infty} \int_{-\infty}^{+\infty} \mathrm{f}(x, y) e^{-2\pi j v_{x_r} (x \cos \Phi + y \sin \Phi)} \, \mathrm{d}x dy \\ P(v_{x_r}, \Phi) &= F(v_{x_r} \cos \Phi, v_{x_r} \sin \Phi) \end{aligned} \tag{2.1}$$

Where $F(v_x, v_y) = \int_{-\infty}^{+\infty} \int_{-\infty}^{+\infty} \mathrm{f}(x, y) e^{-2\pi j (v_x x + v_y y)} \, \mathrm{d}x dy$ is the 2D Fourier transform of the radioactivity distribution $f(x, y)$, $v_x = v_{x_r} \cos \Phi$, $v_y = v_{x_r} \sin \Phi$.

The 2D central section theorem, described by equation 2.1, can be formulated as follows: for an angle Φ, the Fourier transform of the 1D projection is equal to the

profile at the same angle Φ passing through the origin of the 2D Fourier transform of radio-activity distribution:

$$P(v_{x_r}, \Phi) = F(v_x, v_y) \tag{2.2}$$

Using the central section theorem and performing the variable change:
$x_r = x\cos\Phi + y\sin\Phi$ and $v_{x_r} = \sqrt{{v_x}^2 + {v_y}^2}$, $v_x = v_{x_r}\cos\Phi$, $v_y = v_{x_r}\sin\Phi$.

The inverse Fourier transform of $F(v_x, v_x)$ is written as:

$$\begin{aligned} f(x,y) &= \int_{-\infty}^{+\infty}\int_{-\infty}^{+\infty} \mathrm{F}(v_x, v_y) e^{2\pi j(v_x x + v_y y)}\, \mathrm{d}v_x dv_x \\ &= \int_{-\infty}^{+\infty}\int_{-\infty}^{+\infty} \mathrm{P}(v_{x_r}, \Phi) e^{2\pi j(v_x x + v_y y)}\, \mathrm{d}v_x dv_x \\ &= \int_{-\pi}^{+\pi}\int_{0}^{+\infty} \mathrm{P}(v_{x_r}, \Phi) e^{2\pi j v_{x_r} x_r}\, \mathrm{v}_{\mathrm{x_r}} dv_x d\Phi \end{aligned} \tag{2.3}$$

$$f(x,y) = \int_{\frac{-\pi}{2}}^{\frac{\pi}{2}}\int_{-\infty}^{+\infty} |v_{x_r}| \, P(v_{x_r}, \Phi) e^{2\pi j v_{x_r} x_r}\, \mathrm{d}v_x d\Phi \tag{2.4}$$

By decomposing the $P(v_{x_r}, \Phi)$ transformation according to v_{x_r}, we finally obtain:

$$f(x,y) = \int_{\frac{-\pi}{2}}^{\frac{\pi}{2}}\int_{-\infty}^{+\infty}\int_{-\infty}^{+\infty} |v_{x_r}| \, P(v_{x_r'}, \Phi) e^{2\pi j v_{x_r}(x_r - x_r')}\, \mathrm{d}v_{x_r} dv_x' d\Phi \tag{2.5}$$

By posing $P^F(x_r, \Phi) = \int_{-\infty}^{+\infty} P(v_{x_r'} h(x_r - x_r') dx_r'$
and $h(x_r) = \int_{-\infty}^{+\infty} |v_{x_r}| \, e^{2\pi j v_{x_r} x_r} \mathrm{d}v_{x_r}$
we can simplify equation 2.5:

$$f(x,y) = \int_{\frac{-\pi}{2}}^{\frac{\pi}{2}} P^F(x_r, \Phi) \mathrm{d}\Phi \tag{2.6}$$

$P^F(x_r, \Phi)$ represents the projections filtered by the ramp filter $h(x_r)$. Thus, equation 2.6 describes FBP. The ramp filter amplifies the high frequencies. The amplification of high frequency therefore increases the image noise. The optimal way to resolve this problem is to introduce an apodization window w into the FBP equation, to attenuate the high frequencies. This term w is introduced in the definition of the total filter $h(x_r)$:

$$h(x_r) = \int_{-\infty}^{+\infty} |v_{x_r}| \, w(v_{x_r}) e^{2\pi j v_{x_r} x_r} \mathrm{d}v_{x_r} \tag{2.7}$$

There are many low-pass filters; the best known and the most used are the filters of Hamming, Hann, Butterworth, Gauss.

An example of an apodization window is the Hamming filter, defined by the following equation:

$$w(v) = \begin{cases} \frac{1+\cos\frac{\pi v}{v_c}}{2} & \text{at } \mid v \mid < v_c \\ 0 & \text{at } \mid v \mid > v_c \end{cases} \tag{2.8}$$

where v_c is the cut-off frequency of apodization window. The choice of the cutoff frequency v_c of apodization window. Thus determines the frequency lower limit that will not be taken into account in the Back-projection.

2.3.1.3 3D Filtered Back-projection

The Filtered Back-projection (FBP) can be written in 3 dimensions by adding the dimension θ in projection calculations. However, filtered 3D projection requires parallel and non-truncated projections. This is not the case in PET, as illustrated in Figure 2.4. In order to solve this problem, a Back-projection method of missing data from a first 2D filtered back-projection reconstruction as proposed in [40]. More recently, a method for estimating truncated projections and thus using 3D filtered back-projection has been proposed in [36]. Another approach is to rearrange the 3D response lines in 2D, as described (SSRB, MSRB or FORE)[35, 36, 37, 41]. Then, 2D filtered back-projection can be used on these reorganized projections.

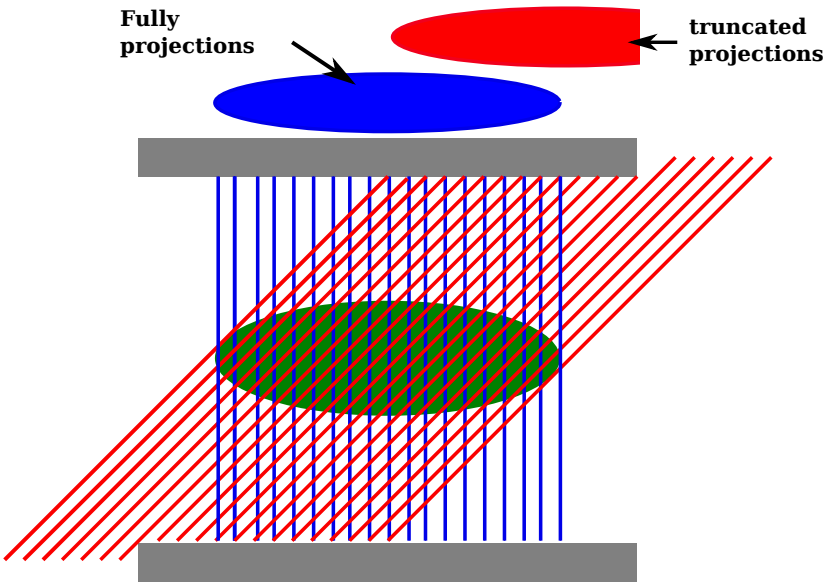

FIGURE 2.4: Illustration of PET truncated projections . In blue, the object in the PET FOV is fully projected on the detectors. In red, the object projections at 45 ° angle are partially recorded by the detectors

- **3D FBP for full parallel projections**
  Suppose that we have complete 2D parallel projection data of the radio-activity distribution $f(x, y, z)$. In this case, the projection $S(u, \Phi, z, \theta)$ is known for $0 < \Phi < \pi$ and $\mid \theta \mid \leq \Psi$ for all the values of (u, v).
  The main steps required for 3D FBP reconstruction are:
  1. Projection filtering for each (Φ, θ)

- a. Calculate the 2D Fourier transform $P(\rho_u, \rho_v, \Phi, \theta)$ such that:

$$P(\rho_u, \rho_v, \Phi, \theta) = \int_{-\infty}^{+\infty} \mathrm{P}(u, v, \Phi, \theta) e^{-2\pi i(u_{\rho_u} + v_{\rho_u})} \mathrm{d}u dv \tag{2.9}$$

- b. Multiply by a 2D $H_c(\rho_u, \rho_v, \theta)$ filter and a low-pass filter function W:

$$P^F(\rho_u, \rho_v, \Phi, \theta) = P(\rho_u, \rho_v, \Phi, \theta).H_c(\rho_u, \rho_v, \theta).W(\rho_u, \rho_v) \tag{2.10}$$

the filter function $H_c(\rho_u, \rho_v, \theta)$ was developed by Colsher [42], its expression, expressed in polar coordinates (r, α), by the following equation:

$$H_c(r\cos\alpha, r\cos\alpha, \theta) = \begin{cases} \frac{\pi r}{\arcsin(\frac{\sin\Psi}{Z})} & \text{at } Z \geq \sin\Psi \\ 2r & \text{at } Z < \sin\Psi \end{cases} \tag{2.11}$$

With $(\rho_u, \rho_v) = (r\cos\alpha, r\sin\alpha)$, $Z = \sqrt{\cos^2\alpha + \sin^2\alpha.\sin^2\theta}$ and $\theta \leq \Psi$, $W(\rho_u, \rho_v)$ is the apodization filter whose role is to restrict the amplification of the noise due to the Colsher filter.
In general, the filter $W(\rho_u, \rho_v)$ is used as the product of 2 Hamming filters $W(\rho_u, \rho_v) = W(\rho_u).W(\rho_v)$
a symmetrical radial Hamming filter $W(\rho_u, \rho_v) = \sqrt{\rho_u^2 + \rho_v^2}$

- c. Apply the inverse Fourier transform to deduce the projections filtered:

$$P^F(u, v, \Phi, \theta) = \int_{-\infty}^{+\infty} \int_{-\infty}^{+\infty} \mathrm{e}^{2\pi i(u_{\rho_u} + v_{\rho_u})} P(\rho_u, \rho_v, \Phi, \theta) \mathrm{d}\rho_u d\rho_v \tag{2.12}$$

2. 3D Back-projection of filtered projections

$$f(x, y, z) = f(x, y, z) + (\cos\theta.\Delta\theta.\Delta\Phi) P^F(u, v, \Phi, \theta) \tag{2.13}$$

3. Repeat steps 1 and 2 for each angle $\Phi : 0 < \Phi < \pi$
4. Repeat steps 1, 2 and 3 for each angle θ: $-\Psi \leq \theta < \Psi$

- **The 3D Back-projection algorithm for the truncated data restitution**
The 3D back-projection method (3D BP) is the most used method for reconstructing 3D truncated PET data [40]. This is method used to reconstruct the 3D object $f(x, y, z)$, cut by cut, using the 2D FBP method, then projecting this reconstructed object according to the angles (Φ, θ) allowing to reconstitute the truncated parts of projections, before applying the 3D FBP reconstruction algorithm to the complete data.
The main steps of this method are as follows:
1. Sort the 2D projections required for 2D reconstruction
2. Reconstruct a first image $f_2D(x, y, z)$ by applying the 2D FBP method in each z-section .
3. For each projection (Φ, θ), where $0 < \Phi < \pi$ and $\theta \leq \Psi$:

– a. Estimate the truncated projections data using Equation 1.25:
$P(u, v, \Phi, \theta) = \int_{-\infty}^{+\infty} f(x, y, z)\, dw$
b. Complete the truncated projections with the estimated data.
c. Calculate the 2D Fourier transform $P(\rho_u, \rho_v, \Phi, \theta)$.
d. Multiply the projections by the Colsher filter $H_c(\rho_u, \rho_v, \theta)$.
e. Apply the inverse Fourier transform to deduce the projections filtered $P^F(u, v, \Phi, \theta)$.
f. Apply 3D back-projection of filtered projections according to equation 2.13.

2.3.2 Iterative reconstruction Methods

The processes of emission and interaction of photon with matter follow a Poisson distribution. In PET, the analytical Reconstruction Methods based on Fourier reconstruction methods are inadequate and provide blurred image often biased by inconsistency between projections, when the number of events recorded per projection is very low. The optimal way to reconstruct the image with good quality from a noisy data is to use an iterative algorithm. Iterative reconstruction methods are exclusively designed for projections as well as discrete images. They therefore apply in 3D in the same way as in 2D.
There are two iterative reconstructions categories, algebraic methods and statistical methods.

- **Algebraic methods:**
  These are conventional iterative methods capable of solving a system of linear equations such as ART (Algebraic Reconstruction Technique), MART (Multiplicative Algebraic Reconstruction Technique) and SMART (Simultaneous Multiplicative Algebraic Reconstruction Technique) [43, 44, 45]. Despite their rapidity, algebraic reconstruction methods are rarely used in PET.

- **Statistical methods:**
  These are iterative methods that use a probabilistic formulation of image reconstruction, such as the Maximum Likelihood Expectation-Maximization (MLEM) method [46]. It is an accelerated version Ordered-Subsets Expectation-Maximization (OSEM)[47], and the Row Action Maximization Likelihood Algorithm (RAMLA)[48, 49, 50].
  They converge on a solution f that maximizes the likelihood $proba(p \mid f)$, which minimizes the difference between calculated projections and observed, compared to the chosen probabilistic model. These three methods are the most used in PET and will be detailed below.

The statistical reconstruction methods are generally preferred that can model the statistical properties of the measured data from the object. The emission of annihilation photons can be modeled by Poisson's laws. Therefore, the distribution of the projections recorded by the PET according to a Poisson distribution can be used which are then in statistical reconstruction methods. In the following of this chapter, only the statistical methods will be described.

The object projection in the FOV on the detection modules can be represented by the following equation 2.14:

$$p = Rf \tag{2.14}$$

Where,f represents radioactivity distribution in the PET FOV, p represents its projection on the detection modules and R is the projection matrix. The discretization of the radioactivity distribution f on a set of P pixels in 3D is described by the following equation:

$$f(x,y,z) \approx \sum_{i=1}^{m} f_i b_i(x,y,z) \tag{2.15}$$

Where,$(b_i)_{i=1...m}$ is a set of spatial basic functions that define the radioactive distribution sampling in pixels.
In emission tomography, for each response line, we measure a random variable p_j which describes the number of annihilation photon pairs detected on a response line j. These variables $(p_j)_{j=1...L}$ follow a Poisson distribution whose likelihood is written:

$$proba(p \mid f) = \prod_{j=1}^{L} e^{-<p_j>} \frac{< p_j >^{p_j}}{p_j!} \tag{2.16}$$

The objective of the iterative reconstruction algorithm is to estimate the distribution f leading to the set $(< p_j >)_{j=1...L}$. Equation 2.14 is then written as:

$$< p_j >= \sum_{i=1}^{m} R_{ji} f_i \tag{2.17}$$

The matrix $(R_{ji})_{j=1...L,i=1...m}$ is the system matrix which represents the projection operation of the image in the measurement space.

2.3.2.1 Maximum Likelihood Expectation Maximization

The Maximum-Likelihood Expectation Maximization (MLEM) reconstruction algorithm was proposed by Dempster [46], and used in PET for the first time by Shepp and Vardi (1982)[51]. This algorithm has several advantages over the conventional filtered back-projection (FBP) for image reconstruction, particularly its implementation simplicity. This method assumes that the projections contain a statistical Poisson noise including radioactive emission noise and measurement noise when photons are detected. Indeed, in PET, the radioactivity distribution follows the Poisson law of expectation $\sum_{j=1}^{m} R_{ji} f_i$, in which, the measured signal p_j consists of a random variable:

$$P(p_j \mid \sum_{i=1}^{m} R_{ji} f_i) = \frac{e^{-\sum_{i=1}^{m} R_{ji} f_i} (\sum_{i=1}^{m} R_{ji} f_i)^{p_j}}{p_j!} \tag{2.18}$$

Where f_i is the estimated value of the pixel i in the image f, p_j the projection j and R_{ji} is the pixel projector element i of the image projection j.
The maximum likelihood purpose is to maximize the likelihood function, which represents the probability that an image f may generate the measured projection data.
Taking into account the statistics Poisson nature in the projection data, the MLEM

algorithm proposes to estimate the image to be reconstructed by finding the maximum likelihood function given by the equation 2.19, obtained by combining equations 2.16, 2.17 and 2.18:

$$L(f) = ln\left\{\prod_{j=1}^{L} P(p_j \mid \sum_{i=1}^{m} R_{ji} f_i)\right\} = \sum_{j}^{L}\left\{p_j ln(\mid \sum_{j=1}^{m} R_{ji} \mid f_i) - \sum_{i=1}^{m} R_{ji} f_i - ln(p_j!)\right\} \tag{2.19}$$

Therefore, the MLEM algorithm can be written in the following form:

$$f_i^{n+1} = f_i^n \frac{1}{\sum_{j=1}^{L} R_{ji}} \sum_{j=1}^{L} R_{ji} \frac{p_j}{\sum_{i=1}^{m} R_{ji} f_i^n} \tag{2.20}$$

The estimate f_i^{n+1} is thus obtained from the estimate f_i^n corrected by a multiplicative factor which corresponds to the back-projection of the measured projections ratio on the estimated projection. Therefore, there are two steps during the reconstruction with MLEM: the first is a projection$\sum_{j=1}^{m} R_{ji} f_i^n$ and the second is a back-projection $\sum_{j=1}^{L} R_{ji} \frac{p_j}{\sum_{i=1}^{m} R_{ji} f_i^n}$

The MLEM algorithm has several advantages. The most important is that can be applied to both 2D and 3D projections, even if they are truncated. In addition, the MLEM reduces the artifact around areas with high radio-activity concentration and improves signal-to-noise ratio in low activity concentration areas.
The MLEM algorithm applied in PET requires a high number of iterations before converging and then high computational time, which is the major disadvantage. This constraint makes its practical implementation very limited in the the clinical application.

2.3.2.2 Ordered Subsets Expectation Maximization

The Ordered Subsets Expectation Maximization (OSEM) method, proposed by Hudson [47], was created to improve the convergence speed of MLEM algorithm [47, 52]. It consists of grouping the projections in K subset before applying the MLEM method.

$$f_i^{n+1} = f_i^n \frac{1}{\sum_{j \in Sb}^{L} R_{ji}} \sum_{j=1}^{L} R_{ji} \frac{p_j}{\sum_{j=1}^{m} R_{ji} f_i^n} \tag{2.21}$$

Where, j belongs to the subset Sb.
The Subsets are organized in such a way that they contain a maximum information following to the LOR angle Φ or the angle θ with the PET axis. The estimated distribution on the first subset f^1 used f^0 as initialization to the MLEM algorithm are applied to the second subset and so on. The image is updated K times during an iteration, after each pass on the elements of a subset, instead of updating the image after a passage over the N elements of iteration. This makes it possible to obtain a convergence K times faster than the algorithm MLEM [51].

2.3.2.3 Row Action Maximization Likelihood Algorithm

The Row Action Maximization Likelihood Algorithm (RAMLA) method is developed to accelerate the MLEM method. This is a special case of the OSEM method in which the subsets number is equal to the number of projections. The image is updated after each projection, wich is controlled using a parameter called "relaxation parameter" [48, 49, 50]. This parameter consists of accelerating the convergence progressively and preventing the images noise by imperfect data during the first iterations.

The RAMLA method algorithm is written as follows:

$$f_i^{n+1} = f_i^n + \lambda_n f_i^n \left(\frac{p_j}{\sum_{j=1}^{m} R_{ji} f_i^n} - 1\right) R_{ji} \tag{2.22}$$

Where λ_n is the relaxation parameter, f^n is the image at iteration n, p is the projection and R represents the probability matrix that photons pair emitted by the voxel i is detected on the LOR j.

2.4 Data correction

The PET images quality is necessary to make a good diagnosis cancer. In order to optimize the images quality, it is necessary to correct the following phenomena: Random, Scatter, attenuation, dead time and the LORs variable efficiency.

2.4.1 Normalization

The PET scanners are composed of the detectors arranged around the rings. Therefore, the detection sensitivity of a uniform source varies from one response line to the other, thus resulting in a uniformity problems in the reconstructed image. Several physical and geometrical phenomena are involved in these variations. Such as the crystal ability to detect the annihilation photon (depends on its detection angle and energy), the size and shape of the crystal, and the electronics ability to detect the light resulting from the absorption of a part or all photon energy.

The simplest method to correct this problem is to perform the acquisition using cylinder uniformly filled with high radioactivity concentration. The normalization coefficients are then proportional to the inverse of the recorded coincidences number on each response line. This correction method requires measuring a very large coincidences number, which generally imply acquisition of several hours. It is also important that the radio-activity concentration in the phantom placed in the FOV is homogeneous, which is generally difficult to control. Finally, the presence of scattered coincidences can bias the normalization coefficients measurement. Despite these difficulties, this technique is the most used in generating the needed data to compensate the sensitivity differences between the LORs [53, 54].

2.4.2 Attenuation correction

Among the various physical factors that degrade PET images, photon attenuation is considered that one of those factors can introduce most of the artifacts and distortions in reconstructed images. Indeed, the Attenuation is the most important phenomenon which demand correction. Various strategies were developed are presented below [55].
- The first method employs a radioactive source emitting positrons such as Germanium 68 (^{68}Ge) provides images of patient transmissions as well as "blanks scans" (empty acquisitions) used for calculating correction factors called ACFs.
- The second method uses a photon source such as Cesium 137 (^{137}Cs) which may improve in the acquisition of transmission scans. Indeed, for the same activity the source of ^{137}Cs offers a higher count rate and a lower acquisition time than the source of ^{68}Ge. In addition, the photon energy emitted by ^{137}Cs (662 keV) reduces interference with patient activity but requires the use of an adjustment when calculating ACFs. As well as, the ^{137}Cs has a very long half-life that requires no replacement, unlike the ^{68}Ge source which must be regularly changed.
- The third attenuation correction method is the segmentation use that allows the linear attenuation coefficient assignment to a region particular corresponding to a given tissue.
- The fourth methods is based on the introduction of mixed devices such as PET/CT makes attenuation correction using the acquired data from the distribution of attenuation coefficients measured by X-ray CT examination. Therefore, concerning the PET/CT or PET/MRI, the attenuation correction factors can be computed from images of the patient acquired with different types as CT or MRI. The CT data actually represent transmission scans and can be appropriately scaled to the correct energy of 511 keV. The MR images can only be used indirectly, for example by segmentation and assignment of specific values to different tissue types, or with the use of template-based methods [56].

2.4.3 Random correction

There are two approaches to correct the random events in PET. Figure 2.5 gives an illustration of the two methods.

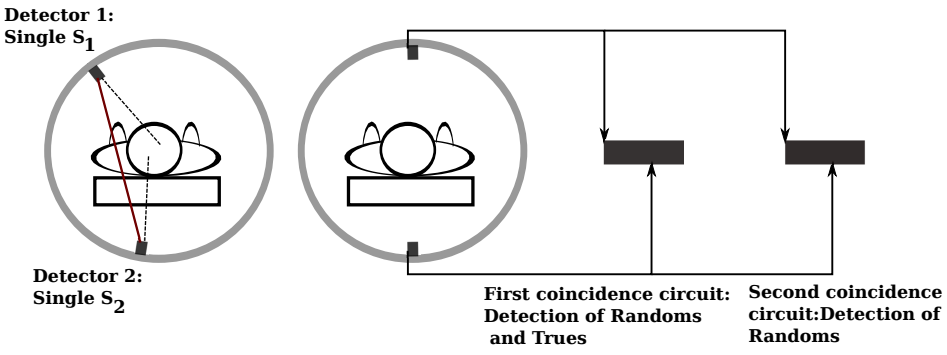

FIGURE 2.5: Methods for random correction events using non-coincident events (left) and using the two coincidence circuits (right).

- The first is an analytical method based on the total number of – by coincidence or not – γ photons detected Figure 2.5. This method consists of estimating the random events number R_{i_1,i_2} detected between two detectors 1 and 2 following the equation 2.23 :

$$R_{i_1,i_2} = 2\tau S_{i_1} S_{i_2} \tag{2.23}$$

  where i_1 and i_2 are the two crystals forming the LOR, S_{i_1} and S_{i_2} are the singles events respectively detected by these crystals, and τ is the duration of the coincidence window.
  This method has two disadvantages: it overestimates in most cases the random coincidences number [57], and it does not take into account the coincidence detection chain characteristics (dead time and multiple coincidence processing). In addition, the rates singles vary along the acquisition [58].

- The second method is the most used, it consists of using two coincidence circuits at different times. The first circuit used to measure the true and random events number, and the second to measure only the random events number Figure 2.5. The difference makes it possible to estimate the true coincidence number between the two detectors. The advantage of this method is that the random coincidences estimation depends on the detection chain in the same way as true coincidences. On the other hand, it generates additional dead time due to treatments it adds to the electronic chain. This method also generates an estimated random coincidences distribution strongly noisy. Therefore, it's recommended to filter this estimate in order to reduce the variance in the random coincidences distribution.

2.4.4 Scatter correction

The detected scatter events falsify the reconstructed images contrasts and distort the relationship between pixel intensity of the image and activity concentration. Therefore, the scatter event is a problem in PET due to the large energy window (from 250 to 600 keV) used to maintain a high detectors' sensitivity.
There are many methods for estimating the scatter coincidences distribution in the PET Scan FOV.

The simplest method exploit the detected photons energy which is 511 keV without Compton scattering. These methods consider that there is a critical energy threshold below which only scattered photons are detected. These techniques use 2, 3 or multiple energy windows for estimating the scattered photons number [59, 60, 61].
The second correction methods estimate the scatter photon distribution from coincidences detected outside the patient or object, whose limits are determined on CT images or by PET images reconstruction . After subtracting random coincidences, all the coincidences detected outside the object or the patient are scatter coincidences. The scatter coincidences distribution with low energy and outside the object or patient are adjusted by a polynomial function [62] or Gaussian [63] to deduce the scatter coincidences distribution within the object or patient. These methods assume

that the scattered coincidences distribution is independent of the radio-tracer distribution. Although it is often verified, this hypothesis is no longer valid when the radioactive distribution is highly heterogeneous [64] .
Another approach is the Direct estimation of the scatter events distribution obtained by Monte Carlo simulation of the imaging system. At last, Diffusion compensation approaches are based on methods of Iterative reconstruction and also use Monte Carlo simulation techniques.

2.4.5 Dead time correction

Dead time is a phenomenon that occurs at several levels of the PET detection chain. The first dead time source comes from the electronic circuits. Each PET detectors response line is not associated with a single electronic circuit. Some coincidences are lost if they arrive at the same electronic circuit as another coincidence formed shortly before. Multiple coincidences are also a dead time source. Another dead time source occurs in the photomultiplier-crystal pair. The dead time represents the minimum time required for 2 photons which arrive successively at the detectors (in the same crystal or in the same photomultiplier tube) and are detected separately.
The overall dead time of the PET detection system depends only on the activity in the PET FOV, and can be considered invariant depending of response lines positions.
The method used to correct the dead times effect is to apply a global multiplicative factor on the acquisition data. It is necessary to determine the factor to be applied according to radioactivity in the FOV. For this, an acquisition of a cylindrical phantom filled with water and homogeneous activity is performed. A large amount of activity is introduced at the start of the acquisition and then data are recorded in period of a few minutes and at regular intervals, until almost total decay. This allows obtaining a factors series (knowing the events number that should have been detected) associated with different amounts of activity. A more appropriate method is to apply block-by-block (or PMT-by-PMT) relative corrections before applying the overall factor. Indeed, the dead time may differ from a block to another (or from PMT to another) [65]. Thus, an equalization of dead times block by block is included included in their general normalization method.

2.5 Conclusion

In this chapter, we have presented the 2D/3D acquisition methods in PET and its correlation with reconstruction as well as the different 2D and 3D reconstruction algorithms used in PET, such as the FBP, MLEM, OSEM, RAMLA methods. Also, the effects of physical phenomena on the reconstructed image , such as attenuation, scattering, and variability of detector response, have been discussed as well as their impacts on PET images along with their various correction methods , which make it possible to optimize the images quality.

Chapter 3

PET Monte Carlo Simulation and Tomographic Image Reconstruction Tools

3.1 Introduction

Monte Carlo simulations are of major interest in various applications, particularly in medical physics and high energy physics. In this chapter, the basic concepts underlying Monte Carlo simulations used in PET imaging will be briefly described. Firstly, the presentation of Geant4 and applications that are of interest optimized the medical applications. Specifically the softwares for Positron Emission Tomography (PET), such as GATE (Geant4 Application for Emission Tomography) software used this thesis. The GATE Realistic simulations remain excessively expensive in regard to computing time. To reduce the calculation time and resolve the storage data management problems, the computing grid is the solution proposed. We therefore, present a realistic and fast Monte Carlo simulation strategy for PET data that used in the thesis work. Finally we present briefly the reconstruction algorithm of STIR (Software for Tomographic Image Reconstruction) software.

3.2 Monte Carlo Simulation using GATE

3.2.1 Monte-Carlo simulation Principle

The Monte Carlo simulation method is a statistical approach that consists of generating random numbers, according to probability laws, to describe given physical phenomena. The randomness of these methods known since 1944. The first uses of Monte-Carlo methods as research tools originated from work on the atomic bomb during the Second World War. This work involved a direct simulation of probabilistic problems involving the neutron random diffusion into fissile material. Around 1948, Fermi, Metropolis, and Ulam estimated the eigenvalues of the Schrödinger equation by Monte Carlo methods [66]. This method is particularly well suited to nuclear physics because the nature of the emission, transport and detection processes is stochastic. It benefits from the various advances in theoretical models in nuclear and particle physics, and the ever-increasing domain of computing performance. These techniques today find many application fields including physics, imaging, meteorology, economy,etc.

3.2.2 Monte Carlo simulations Software in nuclear medicine

The Monte Carlo softwares used in nuclear medicine and especially in PET can be divided into two categories [67] : general softwares and Dedicated softwares

3.2.2.1 General softwares

General Softwares for simulating particle transport are developed in high energy physics and dosimetry application. These software are publicly available through the open licence system.They are well maintained, fully documented and widly used. Their disadvantages are due to the complexity of their use and the computing time. General softwares such as PENELOPE (PENetration and Energy LOss of Positrons and Electrons), EGS (Electron and Gamma Shower) and GEANT4 (GEometry ANd Tracking) , MCNP (Monte-Carlo N Particles) are the must used softwares.

- EGS (Electron Gamma Shower) was developed in 1963 at Stanford Linear Accelerator Center (SLAC, USA) [68]. This software is used to model the passage of electrons and photons through matter and an energy range between few keV to TeV. Several versions are available, the most recent being EGS5 [69] and EGSnrc [70]. This latest version has cross section tables for low energy photons and allows a more accurate simulation of charged particles, with energies ranging from 1 keV to 10 GeV. It is particularly well-suited for medical physics purposes, such as the research and development of devices that allow medical professionals to detect radiation, image a patient's anatomy using x-rays, or deliver a prescribed radiation dose to a tumor while sparing healthy tissue. In addition, EGSnrc is trusted by researchers worldwide for its simulation accuracy and speed.

- MCNP (Monte Carlo N-Particle Transport software) [71] was developed at Los Alamos National Laboratory (LANL, USA). This software was developed during the project Manhattan during the Second World War. It simulates the transport of electrons, photons and neutrons. The simulation software MCNPX (Monte Carlo N-Particle eXtended), also developed at LANL [72] allows to simulate the transport of electrons, photons, neutrons and also heavy charged particles. Their are many application fields of this software, such as radiation protection, dosimetry, medical imaging, reactor calculations and many other nuclear facility.

- PENELOPE (PENetration and Energy LOs of Positrons and Electrons in Matter) has been developed at the University of Barcelona (Spain) [73, 74, 75]. This software allows simulating the transport of electrons, positrons and photons in the matter with complex geometries and for energy ranging from a few hundred eV to 1 GeV.

- GEANT (GEometry ANd Tracking) is a tool developed and maintained by the Geant4 collaboration which consist of several major physics research institutes around the world for particles physics experiments and beyond. The latest version of this software is available at https://geant4.web.cern.ch/.It use the C ++ object-oriented programming language [76]. This software toolkit is

widely documented and used by a broad community of physicists. On the other hand it is difficult to implement in the case of more specific simulations because of their complexity. This is one of the reasons which may explain the development of simulation softwares dedicated to nuclear imaging.

3.2.2.2 Dedicated softwares

Dedicated softwares are specifically developed for PET and / or SPECT. They are easier to implement and use but have incomplete maintenance and documentation because they are often developed by small research groups. In addition, the dedicated software was developed too specifically, and they don't always have the flexibility to study new phenomena. The dedicated softwares specially are developed for PET/SPECT as PETSIM (PET Simulation) [77], Eidolon [78, 79] , SimSET (Simulation System for Emission Tomography) [80] and Geant4 Application to Emission Tomography (GATE) [81, 5].

- PETSIM is a PET Monte Carlo software, developed by C.Thomson (McGill University) to simulate the propagation of gamma photons in simple distributions described analytically as well as in the septa and the organized detector in blocks and crystals. PETSIM contains dead-time simulation modules and random coincidences [77].

- Eidolon software dedicated to PET simulations is developed by H. Zaidi and C. Morel (University of Geneva) [78, 79] available for free online `https://github.com/ericspod/Eidolon`, it is a biomedical visualization and analysis framework designed to render spatial biomedical data and provide facilities for image reconstruction, analysis, and computation. Eidolon can model activity distributions and any discrete attenuation, except the modeling of gamma photons propagation in the detector, the random coincidences and the dead time. In addition, the software is not accelerated by variance reduction methods.

- SimSET is a software developed by R. Harrison, S. Vannoy and D. Haynor (University of Washington) available for free online `http://depts.washington.edu/simset/html/simset_main.html` dedicated to PET/SPECT simulations [80]. It allows to modulate the discrete and analytical attenuation and activity distributions and simulates the gamma photons propagation in the septa and detector. SimSET is a well-validated software and has the major advantage of containing variance reduction methods to significantly accelerate simulations. However, it does not contain a realistic model of PET scanners organized in blocks and crystals (the detector is modeled by a cylindrical crown), or dead time and random coincidences.

- Geant4 Application to Emission Tomography (GATE) is a free software dedicated to the simulation of PET/SPECT scanners [81, 5]. GATE used the Geant4 software and thus allows to simulate the propagation of photons and electrons as well as many other particles in a much higher energy range than TeV. GATE uses a flexible hierarchical description of scanner to model a large number of

acquisition geometries. In addition, this software contains simulation modules for dead time, Random coincidences, and loss of resolution and energy in the blocks. It simulates discrete and analytic activity and attenuation distributions. GATE is a very widely used and validated simulation tool.

Many other PET simulation softwares exist but are less commonly used than those mentioned above, for example PET SORTEO [82] , PeneloPET and GeoPET.

3.2.3 Choice of the Monte Carlo software for thesis work

The softwares mentioned in the section 3.2.2 have advantages and disadvantages, and are therefore more or less suitable for specific applications.The dedicated softwares are certainly easier to use than generic oness but present some disadvantages due to their lack of flexibility. They have limitations in development and support because they are less documented and used only the generic softwares. It is important that we use a well validated realistic simulator so that any quantification method developed and tested on this simulated data, then be applicable to real data. The simulator used must be able to model activity distributions and discrete attenuation, the block and crystal geometry of the detector as well as dead-time and random coincidences. As we will use this simulator to generate virtual acquisitions containing a large cut number, it is necessary that the chosen software is fast in order to be able to simulate a large number of photons in a reasonable time.
The GATE software allows, a better modeling of the interactions occurring in the detector, compared to the other dedicated softwares. In addition, this program can manage the time during a simulation. This makes it possible to simulate the tracers kinetics, to take into account the sources movement and / or the system during a simulation and to reconstruct coincidence events, which is necessary in the PET simulation. In addition, this software has been widely validated for SPECT and PET applications [81, 83, 84] and more recently for computed tomography and radiotherapy [85].
In this thesis work, we chose to model variety clinical PETs with the GATE simulation platform because this software benefits from both generic softwares and specific softwares. Indeed, it uses the Geant4 library, extensively tested and validated by users. This software is also widely used in the field of particle physics and allows, among other things, accurate modeling of the interactions of radiation with matter. Geant4 library updates can easily be integrated with GATE software. Moreover, compared to all the other dedicated softwares that can be used in SPECT and PET, GATE has a complete support and documentation regularly updated by the members of the OpenGATE collaboration gathering about twenty laboratories. In addition, the platform software is easy to use and does not require precise programming knowledge.

3.2.4 GATE Simulator

The Geant4 Application for Tomographic Emission(GATE), is a Monte Carlo simulation toolkit for PET, SPECT and radiotherapy developed by OpenGATE collaboration. It is based on generic Monte Carlo software Geant4. Contrary to GEANT4

and other general simulation programs, which require programming in the original program language, the GATE user doesn't need to write a simulation program in software language.
The GATE software is written in C++ programing and providing a scripting interface with a number of advantages for the simulation of SPECT and PET systems, including the description of source decay phenomena, moving detector components and time management [86, 87]. This language scripting interface make the GATE software easy to use. At the same time, the scripting interface provides a convenient platform for most of the users to create their own simulation of emission tomography experiments and complicated emission tomography system designs. Indeed, the use of GATE facilitates the description of different components necessary to accurate PET system modeling, starting from the geometry configuration, up to the creation of a processing chain for the detected events. Since the software is based on Geant4, it profits from the validation of the underlying physics components including testing from a very large scientific community such as validated physical models, complex geometry description and 3D visualization tools. The physics processes are based on Geant4 libraries including the models of radioactive source decays and particles interactions for a wide range of energies. Therefore, Users interactively select which gamma-ray interactions should be considered (Compton scattering, Photoelectric effect, Rayleigh and gamma-ray conversion), and may specify the energy cuts applied to the production of secondary gamma-rays and electrons. In addition, Geant4 material libraries in combination with user defined material tables are used to cover all of the object's compositions necessary for the system modeling. Several modules are available for modeling the detection process, going from the gamma-rays detection by the scintillating crystals to the coincidences detection in PET and storage of the Simulation data results into standard or specific output files.

3.2.4.1 Software Architecture

The GATE design is a modular structure built on three fundamental layers organized into nested layers in each other (Figure 3.1).
The GATE developer layer consists of the core layer and the application layer. It is built from the various classes that provide the most general features of GATE.

- The core layer includes the Geant4 core and Gate, these layer contain some basic classes that are common or even mandatory in all Geant4 based simulations, such as those involved in the geometry construction, the event generation, the physics process interaction, and the visualization management. In addition the core layer defines the basic mechanisms available in GATE for the time management, geometry definition, sources, digitizer and the processing of simulation products (Data output). This is where the radioactive decay of multiple sources is managed as well as construction, positioning, replication and movement of volumes geometry.

- The application layers are described concrete classes derived from basic classes that allow, for example, defining the shape of new volumes, operations on these volumes (rotation, translation) and the digitizer model of simulation events (energy resolution, dead time, windows coincidences).

- The upper layer (user level), is a scripting language that has been extended to all operations of the lower layers, allowing to build interactively its simulation. Therefore, the user does not need to code directly into Gate: it can only use the script language interactively or through the macro execution [87].

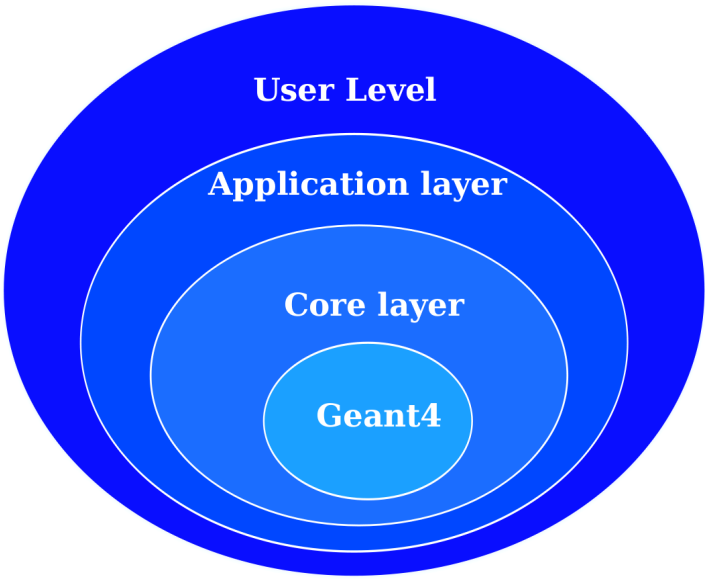

FIGURE 3.1: the layered architecture of GATE

3.2.4.2 Different steps of Gate simulation

Several steps are needed to build a GATE simulation. They are shared between the geometries construction, sources (activity, geometry, energy, type), movement (nature, speed), physical processes, acquisition time and output file type.

- **Geometry description**
  To create a PET system in GATE, We must decompose this system and describe it according to a hierarchy of volume starting from a global system, called "World", which is broken down into parts which, in turn, will be broken down into parts as well, and so on if necessary.
  The world volume is the only volume already defined in GATE when starting a macro. All volumes are defined as daughters of the world volume that has predefined properties as a typical example of a GATE volume(box centered at the origin). For any particle, tracking stops when it escapes from the world volume. This latter must take a large size enough to include all the volumes involved in the simulation. A logical volume is defined by its properties including name, shape, size, and material composition, except its position in the world. When logical volumes are placed at specific positions and Repeaters replicate and then place logical volumes at multiple positions with orientations they form physical volumes. Repeaters are basically elementary geometrical transformations such as rotations and translations applied in succession.

We define the World volume dimensions in the three directions of space using the following script :

```
#     W O R L D volume}
/gate/world/geometry/setXLength 200. cm
/gate/world/geometry/setYLength 200. cm
/gate/world/geometry/setZLength 200. cm
```

To create a new volume we use the following script :

- give a name of the new volume:
  `/gate/world/daughters/name crystal`
- assign the form :
  `/gate/world/daughters/insert box`
- define its dimensions in the three directions of space:
  `/gate/crystal/geometry/setXLength 20. mm`
  `/gate/crystal/geometry/setYLength 4. mm`
  `/gate/crystal/geometry/setZLength 4. mm`
- positioned the new volume in the mother volume (physical volume), considering that the position must always be given by reference to the center of the mother volume:
  `/gate/crystal/placement/setTranslation 10. 0. 0. cm`
- Assign a material to the new volume:
  `/gate/crystal/setMaterial LSO`

The database (GateMaterials.db), is provided with GATE and includes the definition of materials commonly used in nuclear imaging (water, lead, air, plastic, BGO, GSO, LSO, NaI (Tl)...). The user can also easily introduce a new material if its physical and chemical characteristics are known (elements, density, mass fraction of each chemical element, ...). Similarly, GATE can create much more complex geometries by rotating and repeating the object along an axis or a curve.

- Replicate the new volume: linear repeater along an axis, angular repeater following a ring

```
  #Linear  repeater
   /gate/crystal/repeaters/insert linear
   /gate/crystal/linear/setRepeatNumber 4
   /gate/crystal/linear/setRepeatVector 0. 0. 5. cm
 # angular repeater following a ring
   /gate/crystal/placement/setTranslation 125. 0. 0. mm
   /gate/crystal/repeaters/insert ring
 /gate/crystal/ring/setRepeatNumber 18
```

A 3D visualization program, integrated in GATE, makes it possible to visualize the created objects and to debug the potential errors of simulation during geometry creation.

- assign visualization options

```
- color:          / gate / crystal / vis / setColor yellow
- lines:          / Gate / crystal / vis / forceWireframe
- zoom:           / vis / viewer / zoom 2
- angle of view:/ vis / viewer / set / viewpointThetaPhi 60 60
```

The user must respect the geometrical hierarchy to construct relatively flexible geometries. Most PET scanners are built according to the concepts, using one or more rings composed from crystal pixels organized in block detectors. This means that many different imaging systems based on these geometrical concepts. A predefined global systems are used, to facilitate the geometry definition process and to provide a specific output similar to the List Mode Format (LMF) related to the cylindrical PET or sinogram and ecat7 linked to the ecat system.

- **Systems**
  The Gate System is a key-concept which provides a predefined geometry template to simulate the scanner systems. These templates can be used by the systems sharing the same general geometrical characteristics. Each system can be described by specific components having its own specific role and organized in a tree level structure. As for an example, the ecat system is appropriate for modeling PET scanners from the ECAT family. Such scanners are based on the block detector principle, consisting of crystals' array, typically 8 x 8 read by 4 PMTs. The blocks are organized along a ring geometry to yield multi-ring detectors. An example of macro with an ecat definition is provided in:

  - `$GATEHOME/example_PET_Scanner/PET_Ecat_System.mac`

  Different systems are available in GATE : scanner, SPECTHead, cylindricalPET, ecat, CPET and OPET, which can be used to simulate most of the existing PET Scanner.
  From the user's point of view, the main property of a system is geometric hierarchy which is automatically accepted and linked to Basic or specific data output formats (Table 3.1)[88].

- **Phantom**
  Phantom - representing objects to be imaged - is also constructed using GATE. Phantom can be described either by analytical volumes or by voxelized volumes. Phantom is a daugther of the World volume. For a voxelized phantom, each voxel of a volume may consist of a specific material. Then, the sources can be defined inside this phantom.
  The following script command lines describe the NEMA scatter phantom defined as a cylinder filled with Polyethylene with a radius of 10.15 cm and a length of 70 cm placed in the center of world volume :

```
# P H A N T O M
/gate/world/daughters/name NEMACylinder
/gate/world/daughters/insert cylinder
/gate/NEMACylinder/geometry/setRmax 10.15  cm
/gate/NEMACylinder/geometry/setRmin 0. mm
/gate/NEMACylinder/geometry/setHeight 70. cm
```

TABLE 3.1: Different systems available in GATE and their characteristics

System	Components	Attach Keyword Argument	Shape	Available outputs
scanner	level1 level2 level3 level4 level5	level1 level2 level3 level4 level5	geometry not fixed	Basic output : Ascii or ROOT, coincidences only for PETscanner.
CT Scanner	block pixel	"module" "cluster_0...2" "pixel_0...2"	box box	Binary CT image; Basic output : Ascii or ROOT.
cylindri-calPET	rsector module submode crystal layer	rsector module submodule crystal $layer[i]_{i=1,3}$	box box box box box	Basic output : Ascii, ROOT and Raw. Specific: LMF.
CPET	sector cassette module crystal layer	sector cassette module crystal $layer[i]_{i=1,3}$	cylinder cylinder box box box	Basic output : Ascii, ROOT.
SPECT-head	crystal pixel	crystal pixel	geometrynot fixed	Basic output : Ascii, ROOT and Raw. Specific: PRO-JECTIONSET or INTERFILE, no coincidences.
ecat	block crystal	block crystal	box box	Basic output : Ascii, ROOT and Raw. Specific: SINOGRAM or ECAT7.
ecatAccel	block crystal	block crystal	box box	Basic output : Ascii, ROOT and Raw. Specific: SINOGRAM or ECAT7
OPET	rsector module submode crystal layer	rsector module submode crystal $layer[i]_{i=1,7}$	box box box box Wedge	Basic output : Ascii, ROOT and Raw. Specific: LMF.
Optical-System	crystal pixel	crystal pixel	geometrynot fixed	Basic Output: ROOT and Raw. Specific: PROJECTION-SET

```
/gate/NEMACylinder/placement/setTranslation 0.0 0. 0. cm
/gate/NEMACylinder/setMaterial Polyethylene
```

- **Radioactive source and time management**
  Time and movement management is the main characteristic that makes a difference between GATE and the other Monte Carlo softwares for medical physics [67, 86]. These aspects are not applicable in GEANT4 because detectors and sources don't move in high energy physics. On the other hand, they are essential parameters in medical imaging, because it is advantageous to be able to take into account the detectors movements, the patient moves (breathing, heart movements) and the radio-tracers distribution in target organ and time during an examination.
  Time management in GATE includes: definition of the movements associated with the physical volumes that describe the detector and phantom; describe the radioactive sources; and specification of the start and stop times of the acquisition (which are equivalent to the start and stop times in a real experiment).
  To manage and synchronize time-dependent processes, a virtual clock has been created. This clock increments the time as a simulation is launched. For example, if the camera moves during this time, the user must declare two states (2 "runs" or "time-slice") each corresponding to two positions of different geometries (one being obtained from the other by rotation and / or translation that the user defines in the construction of its geometry). The "time-slice" corresponds to a fixed position of scanner. This simulation step is called a "run". At each start of "run", the geometry is initialized following the movement predefined by user [87].
  The proper time of the particles, including their generation time ("decay time") and their transport time from the transmitter point to the detection point ("time of flight ").
  User defines the slice duration (setTimeSlice) using the following script:

```
gate/application/setTimeSlice  200. s
/gate/application/setTimeStart  0. s
/gate/application/setTimeStop     200. s
# S T A R T the A C Q U I S I T I O N
/gate/application/startDAQ
```

  The particle type, location, shape, emission direction, energy, and activity are the parameters used to define a radioactive source in Gate . The radioactive source lifetime generally obtained from the Geant4 database, but it can also be set by the user. The activity determines the decays number which takes place during a simulated acquisition time for a given source.

  To define a line source of ^{18}F we use the following script :

```
# S O U R C E
/gate/source/addSource F18LineSource
/gate/source/F18LineSource/setActivity 100000. becquerel
```

```
# particle
/gate/source/F18LineSource/gps/particle e+
/gate/source/F18LineSource/setForcedUnstableFlag true
/gate/source/F18LineSource/setForcedHalfLife 6586.2 s
/gate/source/F18LineSource/gps/energytype Fluor18
# TYPE= Volume or Surface
/gate/source/F18LineSource/gps/type Volume
# SHAPE= examples Sphere or Cylinder
/gate/source/F18LineSource/gps/shape Cylinder
/gate/source/F18LineSource/gps/radius .5 mm
/gate/source/F18LineSource/gps/halfz 35.0 cm
/gate/source/F18LineSource/gps/angtype iso
# Position
/gate/source/F18LineSource/gps/centre 0. -4.50 0. cm
/gate/source/list
```

- **Physics Process and particle tracking**
  GATE can manage all the electromagnetic physical processes through the GEANT4 libraries. For photons, the processes used are the Compton Scattering, Rayleigh Scattering, Photoelectric Effect, for low energy models; for electrons and positrons, the Ionization and Bremsstrahlung are the concerned processes.
  It is possible to enable and disable these processes. To select a given process one of several models (In the standard energy package "Standard", photoelectric effect and Compton scatter can be simulated at energies between 1 keV and 100 TeV, in "low energy" Rayleigh Scattering is simulated at low energies between 250 eV and 100 GeV, and "inactive" for disabling the process). concerning electrons or positron, the Ionization and Bremsstrahlung can be simulated with "standard" or "low energy" process. By default, the "low energy" physical processes are selected for the photons, and the "standard" processes are selected for the electrons and positron.
  To define the Compton Scattering, Rayleigh Scattering and Photoelectric Effect for low Energy in Gate, we used the following script:

```
/gate/physics/addProcess PhotoElectric
/gate/physics/processes/PhotoElectric/setModel StandardModel
/gate/physics/addProcess Compton
/gate/physics/processes/Compton/setModel StandardModel
/gate/physics/addProcess RayleighScattering
/gate/physics/processes/RayleighScattering/setModel LivermoreModel
```

  The production of secondary particles, energy cuts and range cut, can be defined in GATE for electrons, X-rays and secondary electrons. Concerning the cut in range, this is the definition of the minimal distance for allowing production. This cut is not applied close to the volume boundaries. The cut in energy defines the minimum energy for allowing production. This cut is always applied for low energy processes. Because low energy processes generate more secondary particles than standard Model energy processes, range cuts affect simulation speed more strongly when applied with the low energy

package. By stopping the secondary particles production (electrons, X-rays, and delta-rays) by setting high thresholds may result in a substantial increase in computing speed for a typical simulation of a PET scanner.

- **Sensitive detectors**
  A sensitive detector is attached to some geometry volumes after model definition for a PET scanner systems. These sensitive detectors are used to store information on particle interactions in the matter (hits) using information from steps along a particle track. GATE records and stores information related to the hits only for volumes which are attached to a sensitive detector. All the information regarding the interactions occurring in non-sensitive volumes is discarded. Two sensitive detectors types are defined in GATE: the crystal sensitive detector (crystalSD) and the phantom sensitive detector (phantomSD).

  – The crystalSD allows recording information on interactions inside the volumes belonging to a scanner as the crystals or collimator's. The recorded information of each hits contained include the energy deposit, interaction positions, origin of the particle (emission vertex), interaction type (photoelectric effect, Compton or Rayleigh scatter), volume name, and time information.

  – The phantomSD is used to record information on Compton and Rayleigh interactions taking place in the scanner FOV. This information is then used to estimate whether a photon reaching a detector is a direct or a Compton-scattered photon. Thus, in PET, the phantomSD is currently the only way to discriminate scattered from true coincidences.

  To perform the both series attachments, a volumes series is attached to the crystalSD. Another series of volumes is attached to the phantomSD which necessary to realize a complete definition of the simulation context.
  In GATE, the sensible volume declaration attached to phantom and crystal is done using the following command:

```
/gate/NEMACylinder/attachPhantomSD
/gate/crystal/attachCrystalSD
```

- **Digitizer chain**
  GATE has the ability to convert photon interactions into counts like a real scanner detectors signal processing chain. It enables the modeling of the signal processing chain to collect the data system output. A digitizer modules is followed to simulate the complete signal processing chain and allows to declare the criteria for saving data in the output file. Figure 3.2 shows the followed digitizer chain from hits to a yield output single file.
  When a particle arrives at the block detectors with crystals (sensitive detectors), it can undergo different interactions (Compton, photoelectric, Rayleigh). All the data concerning these interaction points are grouped by individual volume in a file called "Hits". Is contains interaction information as the deposited energy and the volume name where the interaction took place.

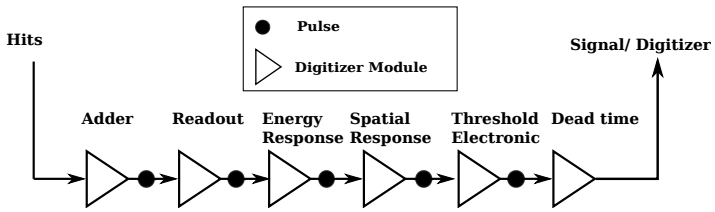

FIGURE 3.2: The digitizer chain of PET Systems.

The data stored in the "Hits" file through a process that removes the "hits" of zero energy deposit. The result file is called "Pulses". Then the "Adder" is sum of the energy deposit of the "Pulses" in a crystal and it may calculate the center gravity position of these "Pulses" positions weighted by their energy deposits according to the formula 3.1:

$$X_G = \frac{\sum_i X_i E_i}{\sum_i E_i}, Y_G = \frac{\sum_i Y_i E_i}{\sum_i E_i}, Z_G = \frac{\sum_i Z_i E_i}{\sum_i E_i} \tag{3.1}$$

X_G , Y_G and Z_G represent the center of gravity coordinates of scintillation in the crystal.
X_i , Y_i and Z_i are the respective coordinates of the different interaction points of the incident particle in the crystal, depositing each time an energy E_i.
At the "Adder" energy, the data arrives at the "Readout" which has the role of summing the deposited energy on the volume which the user defines in the macro. This volume is responsible for grouping the elementary volumes determined by the hierarchical level of the model system used. The interaction point position in a block calculated from the gravity center of different interaction points of the incident particle reconstructed in a crystal from the "Adder" according to the relation 3.2:

$$X_G = \frac{\sum_i X_{Gi} E_{Gi}}{\sum_i E_{Gi}}, Y_G = \frac{\sum_i Y_{Gi} E_{Gi}}{\sum_i E_{Gi}}, Z_G = \frac{\sum_i Z_{Gi} E_{Gi}}{\sum_i E_{Gi}} \tag{3.2}$$

X_G , Y_G and Z_G represent the coordinates of the scintillation gravity center in the volume defined in the macro.
X_{Gi} , Y_{Gi} and Z_{Gi} are the different interaction points coordinates reconstructed from the "Adder", weighted each time by energy $E_{Gi} = \sum_i E_i$

– Energy resolution: Following the hit adder and the pulse reader, which regroup the hits into pulses and then sum these pulses into larger pulses respectively, the remaining modules of the digitizer chain transform these counts into the physical observables of the scanner (singles). These modules are shown in Figure 3.2.
After the readout module Gaussian blurring of the energy spectrum of a pulse is simulated by the blurring pulse-processor module. This is accomplished by introducing a resolution $R_0(FWHM)$, at a given energy E_0. The full width at half maximum (FWHM in mm) of the Gaussian,

modeling the detector spatial response, is given by the user. E_0 is the photoelectric peak energy. A simple model assumes that the FWHM energy resolution R is inversely proportional to $\sqrt{E}$, and is given by equation 3.3:

$$R(FWHM) = \frac{R_0(FWHM)\sqrt{E_0}}{\sqrt{E}} \tag{3.3}$$

- Energy window: Upper and lower energy thresholds can be set for several energy windows by using multiple processor chains. These thresholds are applied to test whether the event energy is between these two threshold values . Then, this event is recorded , otherwise it is rejected.

- Dead-time : Both paralyzable and non-paralyzable dead times can be modeled on Gate. One of both model is inserted in order to apply a dead-time on the single events level.

Other user defined modules can be added individually to model more specific properties: pile-up, light yield, transfer and quantum efficiency.
Moreover, at the end of digitizer chain a single file is produced. Then a coincidence sorter module searches into the single list for the pairs of coincidence singles registered within the coincidence windows timing. Using the event number and the number of Compton, randoms and scatter events can be differentiated from trues. GATE also makes it possible to manage multiple coincidences in different ways, depending on the user's choice (rejection of multiple coincidences, selection according to the energy and position of photons, acceptance of all coincidences, conservation only the first two coincidences).

- **Output file formats**
  Their are several data output formats for saving information from a GATE simulation.

  - A ROOT file is a file that fills up during simulation. This root file contains 3 Trees for PET systems (Coincidences, Hits and Singles) in which several variables are stored. It also contains some information about "hits", called "Hits", others contain information about single events "Singles" at different steps. Other directories also contain the information corresponding the coincidences events "Coincidences" of the CTW and the delay window. All directories are filled in, but the user can choose the type of directory he would like to fill and keep the others empty.

  - ASCII files: during the simulation, four text files are generated: "gateHits.dat" (contains the information corresponding the "hits"), "gateSingleDigi.dat" (contains the information relating to the outputs of the "digitizer"), "gateCoincidenceDigi.dat" (contains the information of the simulations dedicated to the PET applications) and "gateRun.dat" "(contains the number of particles generated during the simulation). It should be noted that ASCII files are usually large files, and it is therefore preferable that the user activates the filling of the files containing the information that interest him without filling the other files .

– specific output formats to Applications: Output formats specific to certain applications (containing the necessary parameters for reconstruction) are also available: LMF (PET), ECAT (PET), Interfile (SPECT).

3.3 Grid Computing

The history of grid computing starts when the Internet was born, offering the access to a distant machine trough a network and giving the possibility to retrieve information anywhere at any time. Exactly in 1961 before network existed McCarthy concludes with his experience about Multiplexed Information and Computing Service Multics that the computing utility could become the basis for a new and important industry. Many years later and when the Web technology was introduced during the beginning of the 1990s researchers thought to develop a new mechanism and a secured sharing concept of computing resources located at different sites. This new concept was called Grid by analogy to the electrical grid providing power on demand.
The development of data transfer protocol like FTP and software controlling networked computers called Portable Bash System (PBS) pushed computer scientists to introduce distributed computing using computer controlling in a local network. At the beginning of 1995s, computers with high performance level called supercomputers compared to general purpose computers. These kind of machines are using today a massively parallel architecture. They play an important role in computational science used in a variety of fields like molecular modeling, quantum mechanics and many other disciplines.
In reality an efficient use of Grid computing capabilities could not be achieved without high speed network such as the US gigabyte testbeds.
Grid Computing is an evolution of Distributed Computing; its basics rely on the technologies which allow the organizations to share computing resources to face different kinds of needs. In general, these resources are geographically distributed and connected by Internet. This network gives the impression of working with a unique and virtual computing system. The common goal of developing such a shared structure is to provid a fast access to database, storage and CPUs establishing high availability computing system with powerful capabilities in order to perform extensive calculations.
This approach could well respond to the problem posed in medical settings, particularly for medical physics applications. Indeed, in the context of the planning of radiotherapy treatments or other techniques using radiation, one often needs to produce and manage medical images and to make precise complex calculations (distribution of doses in human tissues ...).

3.3.1 Local Cluster @ ESMAR

Monte-Carlo simulations, which are increasingly integrated in the planning of Diagnostic and treatments cancer, require a strong need for computing and storage capabilities. In our work, We have been particularly interested to run our simulation using the MaGrid infrastructure. Unfortunately, this did not work well in the last

years because the number of computer nodes was very low while the simulations require important computing resources. In order to reduce the overall computing time consumed by a GATE experiment, a parallel computing platform for running such heavy simulations comprising a local cluster of computers was used.

The local cluster used in our laboratory is managed by the open- source package TORQUE version 6.1.0 based on the original wrapper Portable Batch System PBS [89, 90] and made of 12 nodes with dual Intel XEON 3 GHz processors, each with 8 GB of memory. The Operating System installed on this cluster is scientific linux 6.5 developed by Red Hat Enterprise.

3.3.2 GATE Installation Process

The installation process of GATE comprises two steps: the installation of the Geant4 package and all helper tools are required (e.g. the CLHEP, a Class Library for High Energy Physics, and all the Geant4 libraries) and the GATE installation itself. It should be highlighted that tools needing external libraries or packages may only be activated if the corresponding external system is installed. Detailed information about the installation process and the environment variables definition, and more information about the Geant4 package and corresponding libraries can be found in [91]. To install GATE some care is needed about the required specific version for each dependency (CLHEP, Geant4, ROOT)[91].

3.3.3 Grid Computing for GATE Simulations

The simulation simulations capable of running on Grid Computing are made up of three steps: job splitting (pre-processing), the simulations running and file merging (post-processing).
To reduce the computing time consumed by a complete PET experiment simulation, tasks are split into several jobs by a job splitter. Taking into account the exponential radioactive decay of the used radioisotope, the acquisition time decomposition method (DTM) shown in the Figure 3.3 is the most natural, simple and general scheme, in which the length of the experiment is split into a number of equally long smaller experiments. The time-domain decomposition based on equal time intervals is inefficient. Each interval of time defines a partial simulation of the whole experiment and is associated to a single job set to be submitted to the Grid. A realistic PET experiment simulation task is then split into several smaller simulation jobs prepared to run simultaneously on the Grid. Each single job needs running GATE with an initial activity and partial acquisition time after merging the outputs obtained from each single job.

The decomposition-event method (DEM) (Figure 3.4), is another approach also used to split the simulation. In this approach, the total acquisition time of the simulation is divided into time intervals to produce a number constant of events per interval. In this case, for each task, the initial activity and the acquisition time must be determined . In other words, in the DTM method the acquisition time is forced to be constant, while in the DEM method, it is the number of simulated events produced that is forced to be constant.

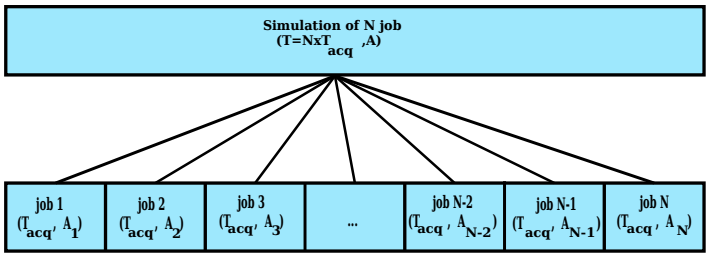

FIGURE 3.3: Decomposition-time method

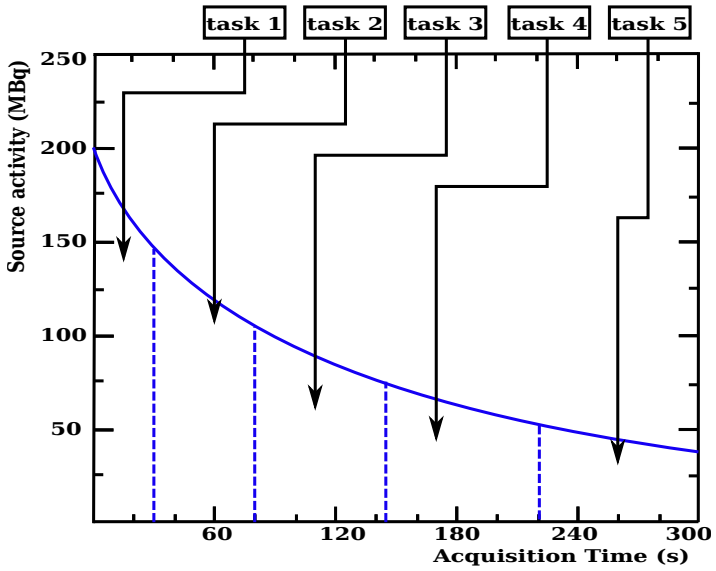

FIGURE 3.4: Decomposition-events method

The output data size can vary from a few megabytes to several gigabytes depending on the condition parameters used for the simulation (particularly the acquisition time and activity concentration). The data output (e.g. ROOT files) contains coincidence events in which the detected singles events for each single event, a detailed information such as the energy deposited, position of annihilation and the coordinates of detection within the modelled scanner geometry, the number of Compton interactions that have occurred during the tracking of each photon and the eventID are stored .
The output merger file uses the ROOT files from the parallelized simulations as input. The information of the split file, generated by the job splitter is used to merge the ROOT files into a single output file as shown Figure 3.5. The events ID will not be the same as in a single CPU simulation. This is solved by using the last event ID of each sub-simulation as an offset for the next. The output data is transferred from the local cluster to the local disk storage of the user interface computer while merging the output into a single file with corrected events ID. The ROOT platform can then be used to access the data for analysis.

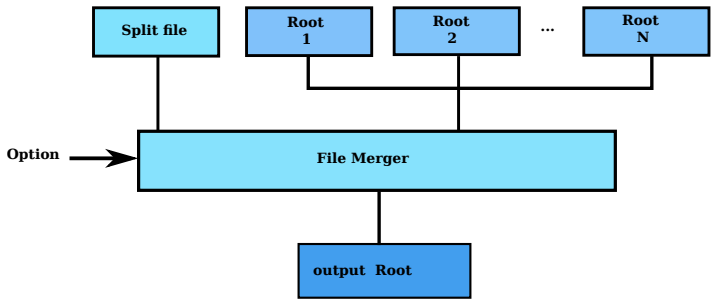

FIGURE 3.5: The output merger used to merge ROOT output data into a single output file.

3.4 STIR - Software for Tomographic Image Reconstruction

The software for Tomographic Image Reconstruction (STIR) [92] is a flexible open source software package which uses the object-oriented library for 3D Reconstruction of PET and SPECT data. The STIR software originated in the PARAPET project (1997-1999), which was a European Union funded collaboration on 3D PET reconstruction algorithms. The collaborators of the PARAPET project designed a library of classes and functions for 3D PET image reconstruction [93, 94]. This library was released as Open Source in June 2000. Following the completion of the project, the software was renamed to STIR and maintained occasionally. The first release of STIR remained restricted to reconstruction, simulation and manipulation processing of PET data in sinogram format. STIR is organized into three parts: the core library, several utilities providing command-line functionality and a framework for automatic testing. Many users of STIR only use the command-line utilities to estimate correction factors for the data, reconstruct the image, manipulate data or images.

The STIR offering both analytic 2D Filtered back projection (FBP2D) and 3D back-projection Algorithm (FBP3DRP) as well as iterative reconstruction algorithms (OSMAPOSL -Ordered Subsets Maximum A Posteriori One Step Late, which reduces to OSEM or MLEM for appropriate parameters). STIR has been widely used in the scientific community, especially for first evaluations of new scanner designs. The reconstruction is based on 3D sinograms with a corresponding header file defining the reconstructed image dimensions and scanner parameters.
For the conversion of GATE-simulated data to STIR sinograms, a c++ analysis code was used to build the sinogram from the simulated data output and import them into the software for tomographic image reconstruction where the reconstruction algorithm was applied. The parameters for the reconstruction (type and parameters of projector, number of subsets and iterations) are defined in a simple text file. Correction files for attenuation and normalization may be defined in this file as well.
For standard OSEM reconstruction, these data are back-projected to a sensitivity volume in image space, which is used during the image update in the reconstruction process. For convenient use of this code, a script was implemented which automatically performs the conversion of the simulation output to STIR sinograms, the

creation of sinogram header and parameter files and the subsequent reconstruction. A several scanner configurations may be tested and evaluated by this way with minimal user interaction necessary.

3.5 Conclusion

In this chapter, we have briefly presented various software based on Monte-Carlo methods used in nuclear imaging, distinguishing generic softwares from specific softwares. We have also presented the characteristics of the GATE simulation platform, based on GEANT4 and developed specifically for nuclear imaging applications. The GATE simulation platform has been described by detailing the main features used during the work of this thesis. We have also presented the GATE simulator's main advantages and its ability to model realistic configurations (source and phantom movement, time management, integration of voxelized volumes, modeling of dead time) and the different steps of Gate simulation. In addition, the parallelization techniques Monte Carlo simulation for PET on the calculation grid and briefly the reconstruction algorithm of STIR software are presented.

Chapter 4

Results and Discussions

4.1 PET system Validation according NEMA Protocol

The simulation code validation is based on comparing the experimental results of the real experimental acquisition protocol using a test object of form and known activities distribution or those published with those obtained by the simulation in the same conditions. To achieve a better validation result it is recommended to apply exactly the same treatment and analysis on the simulated data as the experimental raw data. The National electrical Manufacturers association (NEMA) performance measurements protocol NU 2-2012 [6] is widely accepted as the standard Methodology for assessment of PET system's performance. They describe precisely a set of protocols making it possible to measure reference figures. The description comprises the experimental protocol, from the Data acquisition to the calculation of reference figures parameter. The experimental results according to NEMA standards protocol are calculated by manufacturers of most Clinical PET systems available. The scanner performance parameters used in the validation of Monte Carlo code are calculated according NEMA protocol, which include spatial resolution, sensitivity, noise equivalent count rate, scatter fraction and the image quality measurement appropriate for whole-body imaging.

4.1.1 Spatial Resolution

The spatial resolution describes the degradation generated during the image acquisition of the ^{18}F point source, this degradation results in observation on the reconstructed image. It corresponds to the the minimum distance between two point sources allowing them to be discernible on the reconstructed image. This parameter is measured by the Full Width at Half Maximum(FWHM) of the Point Spread Function (PSF), obtained by assuming a point source. Several Factor contribute to the spatial resolution [21, 95]:
Intrinsic resolution scintillation detector, this factor is related to detector size (d) by $R_i = d/2$.
Positron range: the contribution of this factor R_p on the spatial resolution is determined from the FWHM of the positron count distribution (0.2 mm for ^{18}F).
Non-collinearity : the contribution of this factor R_a is related to scanner Diameter ring (D), R_a is calculated using the equation $R_a = 0.0022 \times D$.
Localization of detector : the error R_l corresponds to the inaccuracy on the photon interaction localization in the detector in mm.

Tomographic reconstruction methods used: This factor $1.2 \leq a \leq 1.5$ depends on the choice of reconstruction algorithm and the filter used. a worth typically 1.2 when using a filtered back-projection algorithm with filter ramp and is without unit.
The Full Width at Half Maximum of this resolution in mm is given by:

$$FWHM = a\sqrt{(R_i)^2 + (R_p)^2 + (R_a)^2 + (R_l)^2} \tag{4.1}$$

The spatial resolution varies with the source position in the scanner FOV and degrades depending on the source position from the scanner axial center. We distinguish 3 parameters characterizing the spatial resolution in image figure 4.1:

- Transverse Radial resolution: is determined by the FWHM of point spread function obtained from source profile measured in system plane in radial direction as shown in Figure 4.1
- Transverse Tangential resolution: measured FWHM of source profile reconstructed image PSF in the perpendicular direction on the line joining center of the point source transverse cut (Figure 4.1).
- Axial resolution : is determined by FWHM of point spread function of source profile measured in axial FOV.

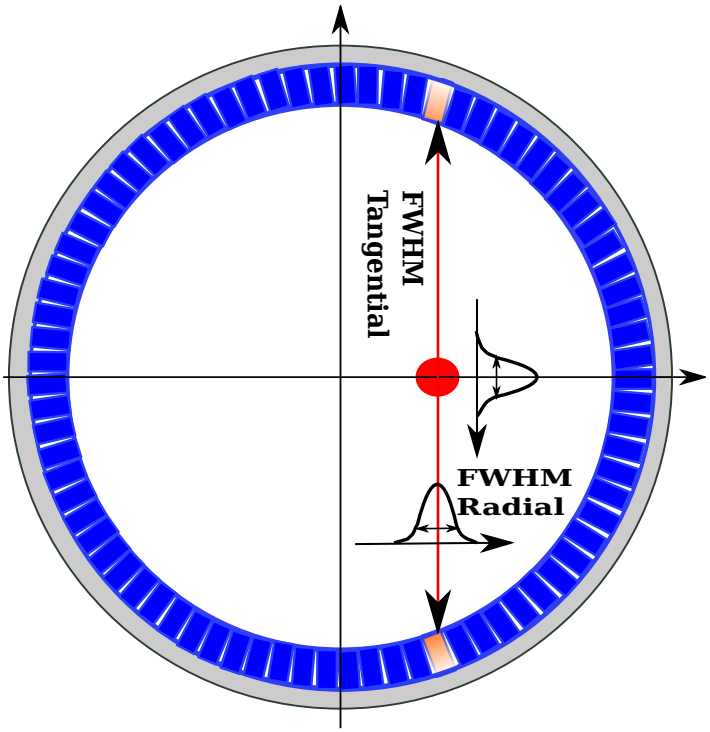

FIGURE 4.1: Transverse Radial and tangential spatial resolution of tomograph measured with punctual source placed in system FOV.

The NEMA NU2_2012 protocol proposed to calculate the spatial resolution with three point source of ^{18}F placed at the center of the axial FOV and three-eighths of

the axial FOV from the center of the FOV (i.e. one-eighth of the axial FOV from the end of the PET scanner). The figure 4.2 shown the source placement in the scanner transverse FOV.

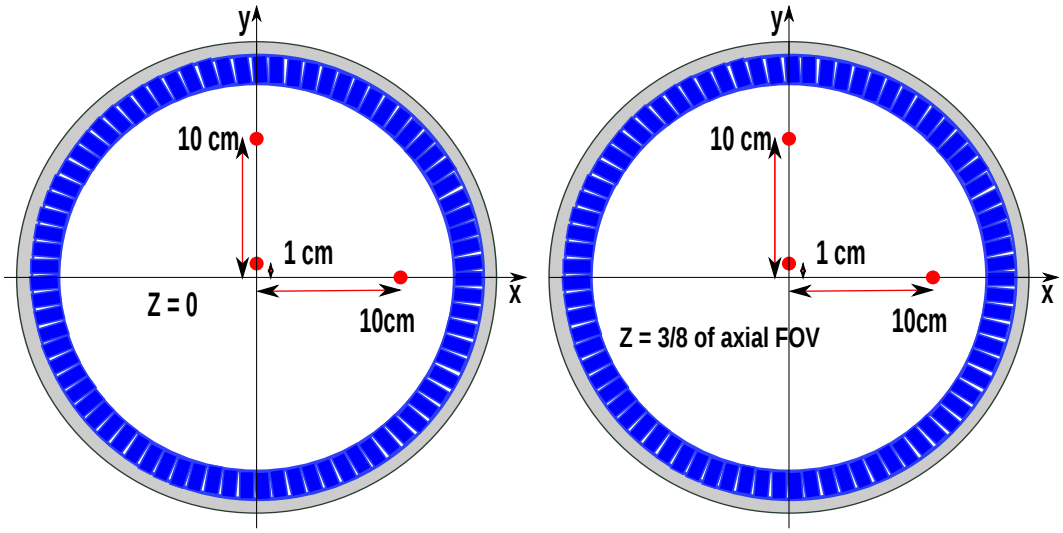

FIGURE 4.2: Transversal source placement for spatial resolution calculation in PET using NEMA NU2-2012 protocol.

4.1.2 Sensitivity

The PET scanner sensitivity is the detection efficiency of a coincidence event when a radionuclide located in the scanner FOV. That's defined by the number of events detected per second, for a given radioactive concentration source, and expressed in counts per second per unit activity concentration ($cps/MBq/cc$ *or* $cps/KBq/cc$). It depends on the detectors characteristics -detection efficiency- and the electronics acquisition, as well as the scanner geometry. Several parameters such as the scintillation decay time, density, atomic number, and thickness of the detector material can affect the detection efficiency. The 3D mode PET sensitivity profile is triangular with the maximum at the center of the tomographic axis and a decay away from the axis towards the edge of the system. For the PET sensitivity calculation, a positron emitting source is required without any gamma-ray attenuating medium prior to arrival at the detector, which is impossible in practice. Therefore the NEMA protocol NU2-2012 proposes to measure the sensitivity using the NEMA NU 2-2012 sensitivity phantom that comprises five concentric 70-cm-long aluminum tubes placed around the line source (Figure 4.3), which consists of a plastic tube containing the radioisotope ^{18}F. This plastic tube had an inner diameter of 2 mm and the outer tube had a diameter of 3.0 mm. The used radioactivity was sufficiently low such that the count losses and random events were negligible, with the single-event count losses and the random event rate at <5% and <1% of the true rate, respectively. The sensitivity was calculated with the phantom placed at two positions: in the center of the scanner and 10 cm from the center of the scanner field of view (FOV) [6].

The sensitivity is given by the equation 4.2

$$S = \frac{T}{A} \tag{4.2}$$

where T : count rate of True coincidences (cps), A : Source Activity (MBq/cc)

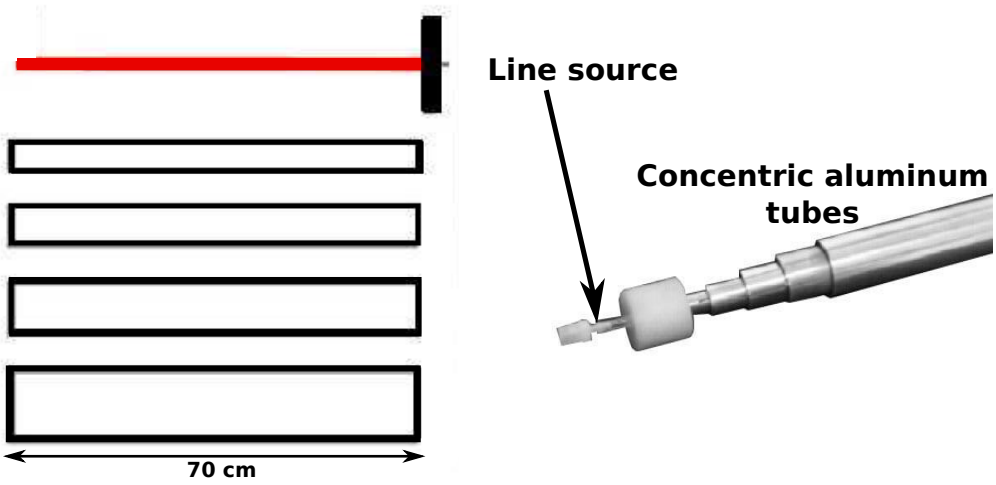

FIGURE 4.3: The sensitivity measurement phantom line source and sleeve concentric Aluminum tube placed around the line source

4.1.3 Scatter Fraction

The scatter coincidences rate is characterized, according to the NEMA NU2 protocol by the scatter fraction which corresponds to the ratio between the number of scattered coincidences and coincidences (true + scattered) measured from a linear source.
The scatter fraction (SF) is often used to compare the performances of different PET scanners. It is given by equation 4.3:

$$SF = \frac{S}{R_T} \tag{4.3}$$

where S and R_T are scattered and prompt count rates(scatters + Trues). The lower the SF value, involved better scanner performance and images quality.

The NEMA NU2-2012 protocol proposes, a cylindrical phantom used to estimate the scatter coincidence. This phantom is cylindrical 700 ± 5 mm tube with an outside diameter of 203 ± 3 mm, it is consist of polyethylene with a specific density of $0.96 \pm 0.01 g/cm$. A 6.4 ± 0.2mm hole is drilled parallel to the central axis of the cylinder, at a radial distance of 45 ± 1 mm (Figure 4.4) from the central axis of the phantom. The ^{18}F is inserted into the Plexiglas line source tube, which had an outer diameter of 4.8 ± 0.2 mm and an inner diameter of 3.2 ± 0.2, and positioned inside a 6.4 ± 0.2-mm-diameter hole. The acquisition is done at a low radioactive concentration, with the aim of having a rate of Random coincidences and lost dead time are negligible

less than 1%. The Scatter coincidences correspond to all the detected LORs and do not cross the linear source.

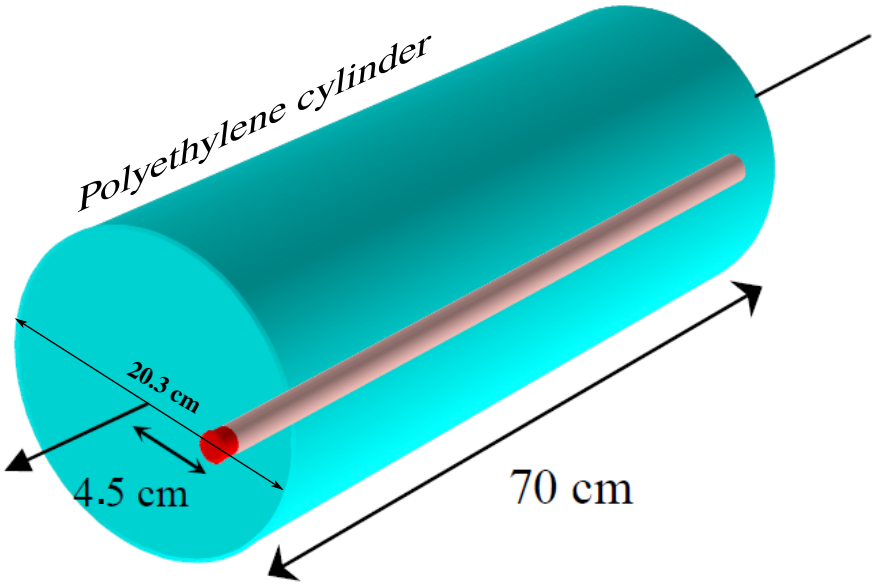

FIGURE 4.4: Geometric model of the phantom used to measure the scatter fraction and count rates for a whole body system.

4.1.4 Noise Equivalent Count Rate (NECR)

A more relevant variable has been developed to evaluate the image quality, it is the Noise Equivalent Count Rate (NECR). That used to give some insight into the quality of the primary data. Although this metric does not directly relate to final image quality, it does demonstrate the impact of dead time, randoms rates, and scatter on the overall ability of the scanner to measure the true events count rate and eliminate Random and Scatter coincidences completely during the acquisition. Generally, the NECR is defined as the equation 4.4:

$$NECR = \frac{T^2}{T + S + kR} \tag{4.4}$$

where : T is the trues count rate.
S the scatter count rate.
R the randoms count rate.
k is a factor equal to 1 or 2 depending to the method used to correct Random coincidences.

The value $k = 1$ is used when the randoms contribution is estimated from the singles count rates, whereas $k = 2$ is used when randoms are measured using a delayed coincidence window. The randoms and scatter rates are given by the equations 4.5 and 4.6:

$$R = R_T - \frac{T}{1 - SF} \tag{4.5}$$

$$S = \frac{SF}{1 - SF} \times T \tag{4.6}$$

Where SF is the intrinsic scatter fraction and R_T is the total count rate.
In general, the test phantom used to calculate the NECR is the the same phantom used in the section 4.1.3 .
Acquisitions are carried out at regular intervals until the source decays. The true coincidence rate is calculated as the difference between the total coincidences and the Random and Scatter coincidences rate. Knowing the scatter fraction, the Random coincidences rate and scatter coincidences rate are calculated.

4.1.5 Image Quality

The NEMA IEC Body Phantom is a form phantom thoracic, of length 18 cm and of volume 9.7 liters, contain cylinder of lung (filled with a low atomic number material with an average density of $0.30 \pm 0.10 g/cc$), with a diameter of 51 mm and a length 180 mm, was placed on the central axis of the phantom and 6 spheres with diameters 10, 13, 17, 22, 28 and 37 mm are centered in a perpendicular plane to the phantom lid and located 7 cm from the latter . The transverse position of the spheres shall be so that the centers of the spheres are positioned at a radius of 57.2 mm from the center of the phantom(Figure 4.5).

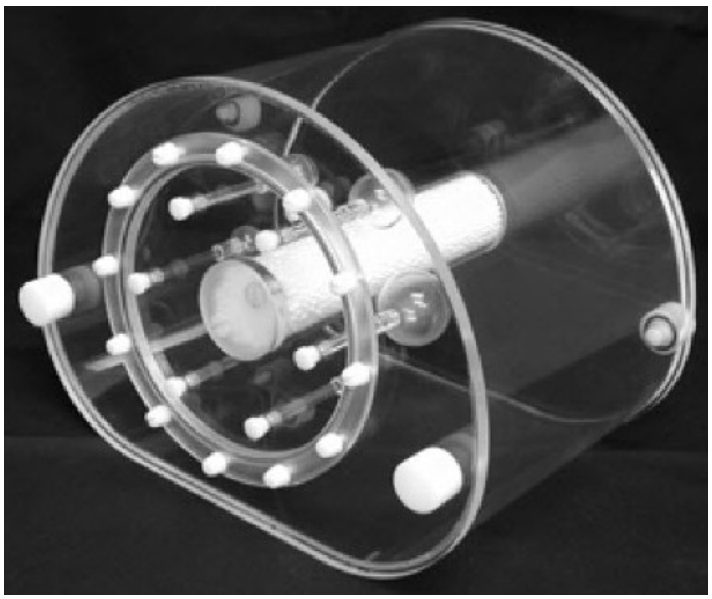

FIGURE 4.5: NEMA IEC Body Phantom.

The phantom was filled with a solution of $^{18}F - FDG$ diluted in water in such a way that the ratio of activity concentration between the four hot spheres -hot lesions- (10, 13, 17, 22 mm, $(^{18}F, 0.56 \mu Ci/cm^3)$ and the background activity in the phantom $(0.14 \mu Ci/cm^3)$ is equal to N=4 (if desired, the acquisition and analysis can be repeated with N=8). The cold lesions shall be filled with water containing no radioactivity for the two largest spheres 28 and 37 mm (cold spheres) and lung cylinder.

4.2 Simulation Study of Clinical PET ECAT EXACT HR+

In these simulation study, the clinical PET ECAT EXACT HR+ is simulated and validated using GATE. The validation is done according to the NEMA (National Electrical Manufacturers Association) NU 2-2001 protocol [6] with comparing the simulated and the experimental results including Scatter Fraction (SF), Sensitivity and system count rate performance extracted from [1, 96, 97, 98]. In the other hand, the validated model is used to study the effect of changing the CTW and dead time model on the scanner performance.

4.2.1 Scanner Model description

The PET ECAT EXACT HR + detection system consists of 4 crowns of 72 modules of Bismuth Germanate (BGO) defining an inner radius of 82.7cm. Each module is divided into a square matrix of 64 (4.05mm $\times$ 4.39mm $\times$ 30mm detection crystals $axial \times transaxial \times depthmm^3$) separated by 0.46$mm$ Gap. The GATE code makes it easy to generate geometrically complex structures using combinations of simple shapes (e.g., boxes, spheres, and cylinders, as defined in GEANT4). The geometrical details of the simulated ECAT Exact HR+ is summarized in the following Table 4.1 [1, 96]

TABLE 4.1: Characteristic of clinical PET ECAT EXACT HR+

Detector Material	Bismuth germinate (BGO)
Crystal Dimensions(mm^3)	$4.05 \times 4.39 \times 30$
Detector Ring Diameter (cm)	82.4
Number of crystal per detector	638
Number of detector per ring	72
Detector total number	18432
Axial Field of view (mm)	155

Figure 4.6 shows the geometry of ECAT EXACT HR+ as well as the NEMA Scatter fraction phantom. This phantom is used to calculate the scatter fraction, the true rate and noise equivalent count rate.

In addition to the specification parameters used for the design of scanner geometry, the physics process and the digital detection chain, summarized in table 4.2, are also taken into accounts in the simulation.

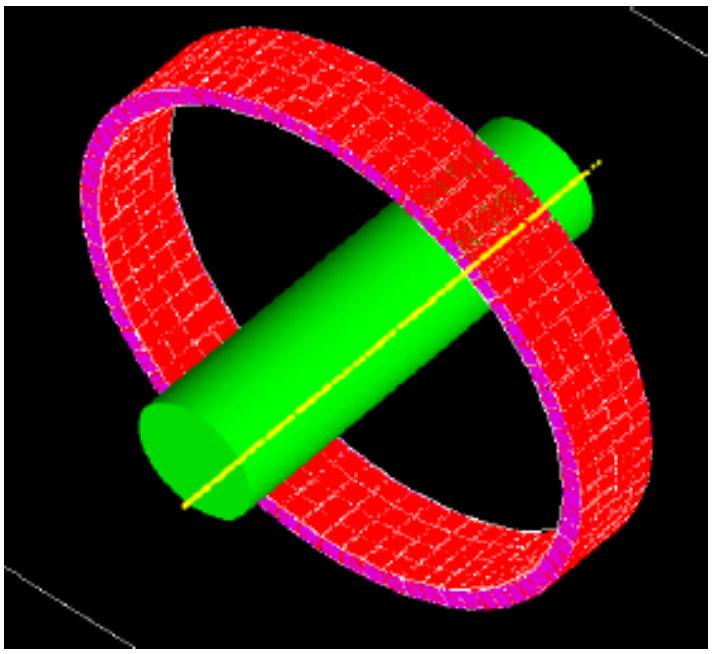

FIGURE 4.6: GATE geometry model of the clinical ECAT EXACT HR+ PET scanner. magenta indicates shielding, red, BGO blocks, and view of the NEMA NU2-2001 scatter fraction phantom (solid green tube), and line source placed in 4.5 cm yellow tube

TABLE 4.2: Physics process and the Digitizer detection chain of clinical PET ECAT EXACT HR+

Physics process	EXACT HR+	
Physics	Photoelectric	Low energy
	Compton	Low energy
	Rayleigh Scattering	Low energy
Cuts	Electron (cm)	0.2
	Ray-X (keV)	10
	Second Electron (keV)	10
Energy resolution at 511 keV	Aleatory between 0.2-0.3	
Dead-Time (ns)	Singles	5000
	Coincidences	500
CTW (ns)	12	
Energy Windows (kev)	300 - 650	

4.2.2 Validation of clinical PET ECAT EXACT HR+ using GATE

The simulation of a GATE-modeled ECAT EXACT HR+ scanner performed using the geometrical parameters and validated through the simulation of standard performance parameters proposed by the National Electrical Manufacturers Association (NEMA) [6]. These parameters are the (SF), the Sensitivity (S), and the Noise Equivalent Count Rate(NECR) as well as the true count rates, obtained from the described simulations were compared with experimental data extracted from the published works in [1, 96] are presented in this section.

4.2.2.1 Scatter fraction

The Scatter Fraction (SF) was performed using the NEMA NU 2-2001 phantom. Table 4.3 show a comparison of the obtained SF with the experimental result. The SF presents an agreement of 9.7 % with the experiment. This difference can be explained by the approximation of the scanner geometry using GATE and the absence of some compositions as the scanning bed patient.

TABLE 4.3: Scatter Fraction(SF) for PET ECAT EXACT HR+

Experimental results	46.9 %
Simulation results	42.3 %

4.2.2.2 Sensitivity

The sensitivity performance parameter of a scanner represents the efficiency to detect the annihilation radiation. The scanner sensitivity expressing the count rate per seconds (cps) [1, 97, 98]. In Table 4.4, the comparison of the simulated Sensitivities with the experimental data [1, 96, 97], shows a 2.9% agreement for R=0 cm and 0.15% for R=10 cm. The difference may be explained by limitations of the photomultiplier tubes (PMT) resolution and the absence modeling of the light shielding between the detector blocks [99]. Furthermore, the application of a varied quantum efficiency factor (QE), might provide better agreement [100].

TABLE 4.4: Sensitivity parameter for ECAT EXACT HR+ PET scanner, calculated using the NEMA NU2-2001 protocols

Experimental results cps/MBq	R=0 cm	6650
	R=10 cm	7180
	Ratio (R=0/R=10 cm)	0.926
Simulated results cps/MBq	R=0 cm	6853
	R=10 cm	7169
	Ratio (R=0/R=10 cm)	0.955

4.2.2.3 Noise Equivalent Count Rate and True Rate

Figure 4.7,4.8 shows successively the NECR and true count rates obtained from the simulation as a function of the source activity concentration. Measured parameters are also extracted from [1, 96, 97] and reported for comparison.

TABLE 4.5: Peak NECR of ECAT EXACT HR+ PET Scanner

Experimental results @ 8 kBq	36897 cps
Simulation @ 6 kBq paralyzable dead time	35397 cps
Simulation @ 7 kBq nonparalyzable dead time	36553 cps

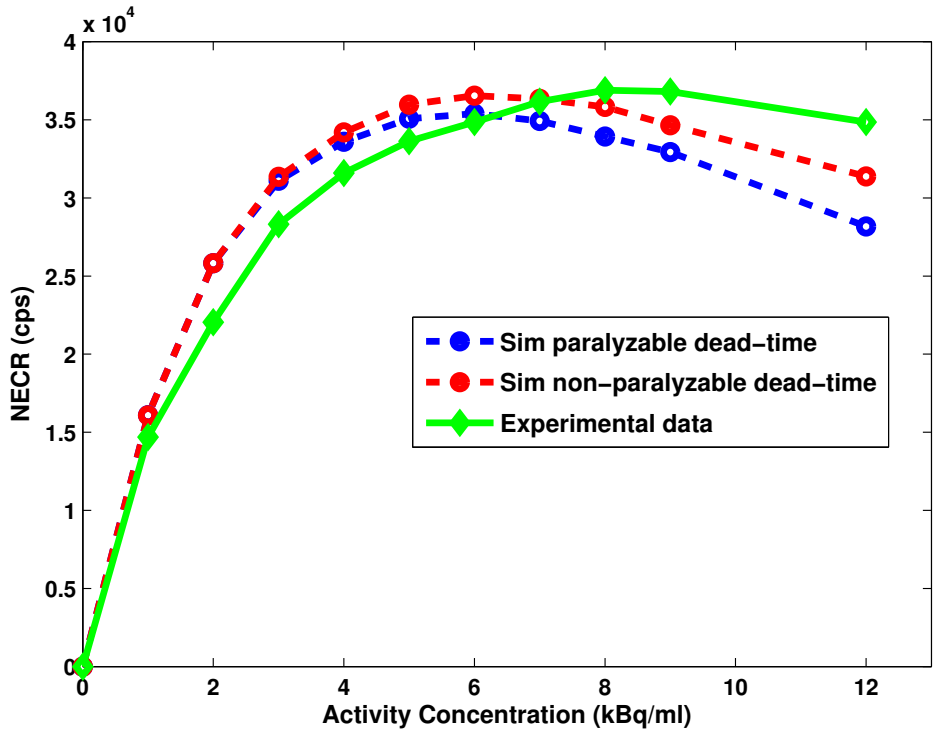

FIGURE 4.7: NECR as a function of the source activity. paralyzable dead-time (blue dotted line), non-paralyzable dead-time (red dotted line), experimental data (solid line).

Concerning the NECR peak values, Table 4.5 shows the NECR peak value for the scanner extracted from the Figure 4.7. A deviation of 4 % (NECR with paralyzable dead time) and 1 % (NECR with non-paralyzable dead time) is observed between the simulations and the experimental data. Here again, the differences are mainly due to the simple dead time model used in the simulation. Figure 4.7 and Table 4.5 exhibit that a better agreement is observed using a non-paralyzable dead time model, than using a paralyzable dead time model.
Figure 4.8 shows a 10.7% agreement with the experiments data for the true count rate. The differences are mainly due to the simple dead time model used in the simulation.

4.2.3 Influence of Windows Timing Coincidences and Dead Time on Count Rate Performance

Firstly, we used GATE platform to study the effect of changing the coincidence windows time on Noise Equivalent Count Rate. Secondly, we present an evaluation of the Count rate performance and noise equivalent count rate (NECR) in different coincidence timing windows arranging from 8 to 12 ns, with different dead-time electronic 5000 ns paralyzable and 4900 ns non-paralyzable.

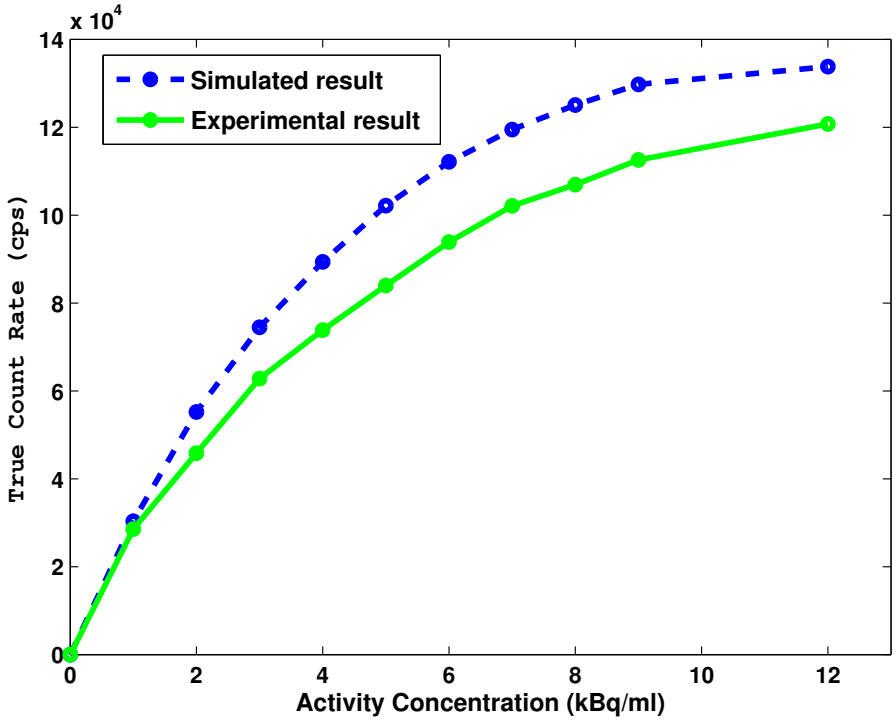

FIGURE 4.8: True count rates as a function of the source activity. Simulation (dotted line), experimental data (solid line)

The Figures 4.9 and 4.10 shows the study of the Count rate performance and noise equivalent count rate (NECR) values in different activity concentrations corresponding the different coincidence timing windows of 6, 8 and 12 ns of the ECAT EXAT HR+.
The obtained results in Figure 4.9 show that the true coincidence rate at lower activity concentrations, not affected by varying the coincidence window times However, at higher activity concentrations, the true rates increase slightly for shorter coincidence windows and random decrease.

Figure 4.10 shows a significant improvement of NECR by using the smaller coincidence window time. The peak NECR increased by 38%. This improvement explain by the reduction of the random when we used the smaller windows coincidence time.

Figure 4.11 shows for different CTW (8 ns, 12 ns) and dead-time (5000 ns paralyzable, 4900 ns non-paralyzable) the true count rates as a function of the source activity concentration. The results show that the true coincidence rate at lower activity concentrations, is not affected by varying the CTW. However, at higher activity concentrations, the true rates increase slightly for shorter CTW (peak true rate increased by 12.3%). The true rate also increased successively by 12% and 20% using two CTW (12 ns and 8 ns) and changing the dead time from 5000 ns paralyzable to 4900 ns non-paralyzable.

Figure 4.12 shows significant improvements based on NECR. Using the smaller

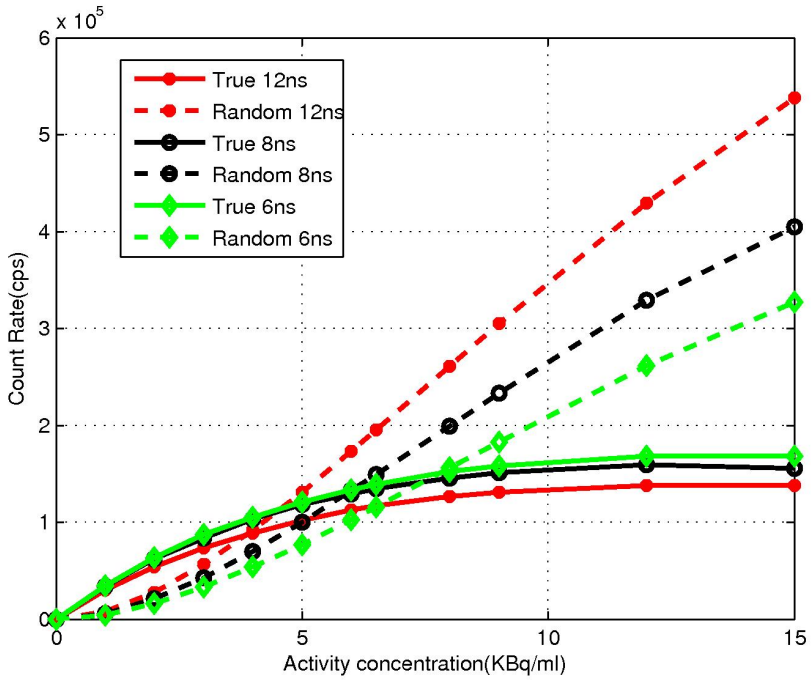

FIGURE 4.9: True rates and random versus activity concentration for varying coincidence window time

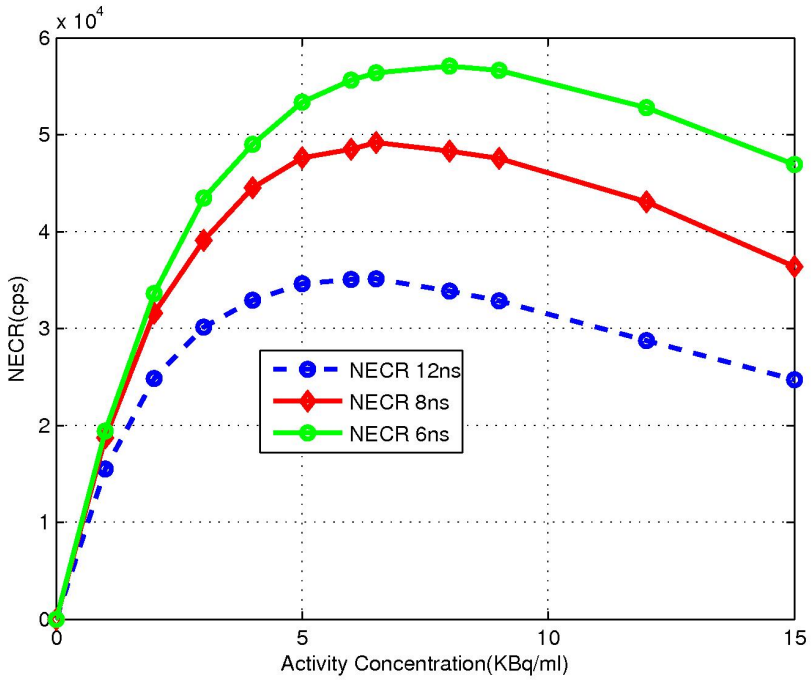

FIGURE 4.10: NECR versus activity concentration for varying coincidence window time

CTW, the NECR peak was increased by 28%. The NECR peak also increase respectively by 4.3% and 6.5% using two CTW (12 ns and 8 ns) and changing the dead time

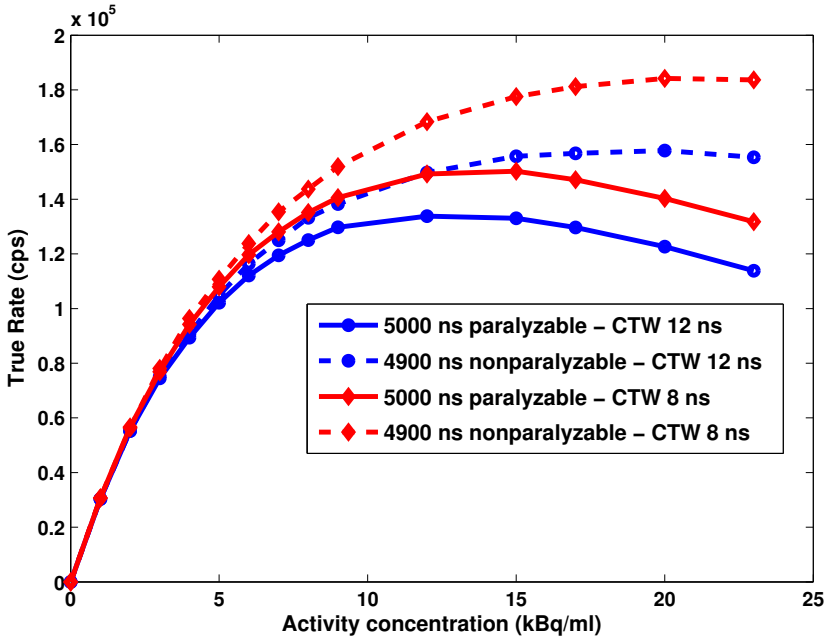

FIGURE 4.11: True rates vs. activity concentration for varying CTW and dead-time (value and model).

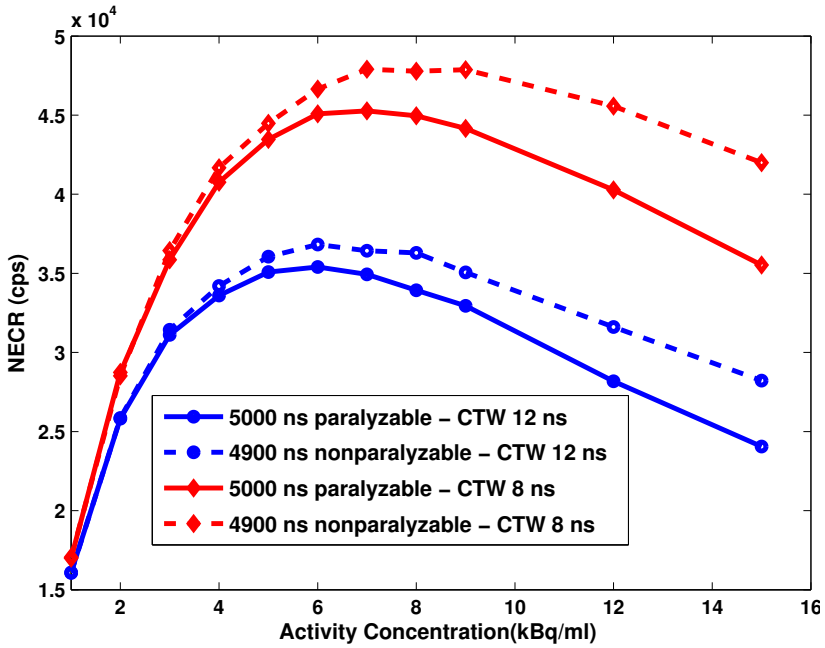

FIGURE 4.12: NECR vs. activity concentration for different CTW (12 ns and 8 ns) and dead-time model (nonparalyzable and paralyzable).

from 5000 ns paralyzable to 4900 ns non-paralyzable. This improvement is mainly due to the number of event recorded in the non -paralyzable dead time which is bigger than the number of event recorded in the paralyzable dead time [88].

4.3 Simulation study of Siemens Biograph mCT 20 Excel PET/CT System

Modern PET scanners are coupled with computed tomography (CT) systems for more precise anatomical localization of cancer [101]. The combined PET/CT system -considered a major development in nuclear medicine - creates complex corrected PET images by multiplying the emission scan by the attenuation correction map generated by X-ray CT. This enhances count rate and spatial resolution and upgrades clinical conditions, diagnostics, development, and treatment planning[101]. In order to manufacturing new scanners, it is necessary to optimize the acquisition protocols and ameliorate the scanner performances. Knowing that the scanner performance is affected by its design and the scintillating material [2]. The increase of the true coincidence counts related to the prompt counts can improve the statistical quality of the acquired projection data and minimize the noise impact, consequently this improvement is the main objectives of a PET acquisition protocol optimization studies [102, 103, 104]. In addition, the statistical quality of the acquired projection data does not only depend on the acquisition protocol, but also on the other parameters as the properties of patients and scanner [103, 105, 106]. Certain studies about scanner technical parameters has been performed, such as the energy window, the coincidences time window, the dead time, and the detectors type, covering most of the configurations currently applied in recent clinical PET scanners[104, 105, 106, 100].

These study focused on the Siemens $Biograph^{TM}$ mCT 20 Excel PET/CT scanner (Siemens Healthcare GmbH, Erlangen, Germany). We addressed the validation of GATE V7.1 simulations according to the NEMA (National Electrical Manufacturers Association) NU 2-2012 protocol [6, 32] and compared the results to the experimental data. We know that the CTW and scanner design are two parameters which affect the NECR. The NECR increase by decreasing the CTW and choose the best scanner design [104, 100]. Taking into account the relation between patient size over scanner FOV diameter and CTW. we studied the effect of the CTW and the block gap and inter-crystal gap on the count rate and spatial resolution in order to optimize the administered dose A_{adm} to the patient using the Siemens $Biograph^{TM}$ mCT 20 Excel scanner.

4.3.1 Model description

The characteristics, including geometry, of $Biograph^{TM}$ mCT 20 Excel PET/CT scanner used in this work are summarized in Table 4.6. The PET detection system is composed of three crowns of 48 Oxyorthosilicate Lutetium (LSO) modules defining an inner radius of 421 mm. Each module is divided into a matrix of 169 $(4 \times 4 \times 20\ mm^3)$ detection crystals $(axial \times transaxial \times depth\ mm^3)$ separated by 0.1 mm Gap. The scanner geometry is illustrated in the Figure 4.13

Other necessary parameters are also considered in the simulation, including the physics process of photon interaction, for which we used the standard Rayleigh, photoelectric, and Compton energy models, with electron range = 30 mm, secondary electron = 1 GeV, and X-ray energy = 1 GeV; and the digital detection chain modeled using GATE to collect the data output. The complete signal-processing chain

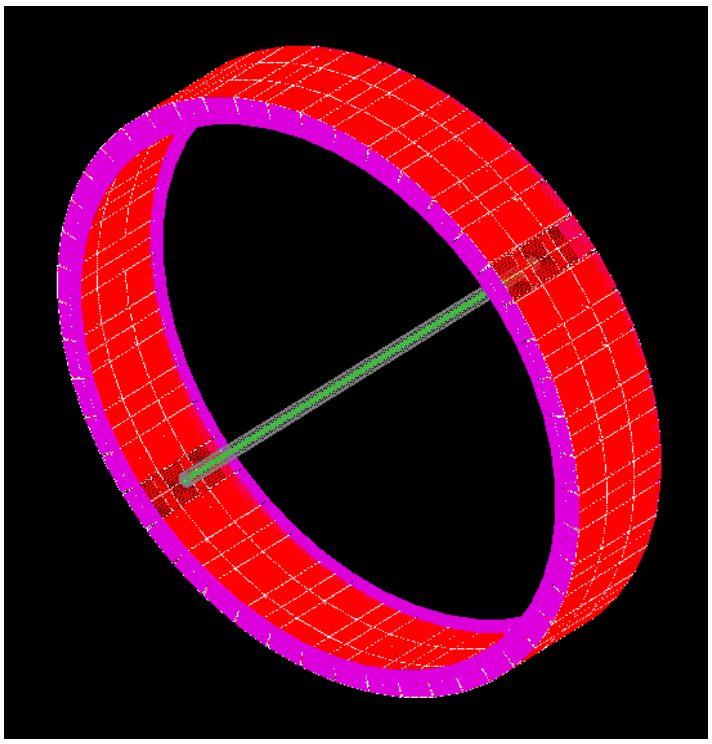

FIGURE 4.13: GATE geometry model of clinical Biograph mCT 20 excel PET scanner. (magenta) indicates shielding, (green), LSO blocks, and view of the NEMA NU2-2012 sensitivity phantom with line source placed at the center

TABLE 4.6: Characteristics of clinical PET/CT *Biograph*^{TM} mCT 20 Excel

Detector Materiel	LSO
Crystal Dimensions(mm^3)	$4 \times 4 \times 20$
Detector Ring Diameter (cm)	82.4
Detector elements per block	169
Blocks per detector ring	48
Detector total number	24,336
Axial Field of view (mm)	164

was simulated using the adder module, readout module, crystal-blurring module, paralyzable or non-paralyzable dead-time module, energy-window module, and coincidence sorter module. The adder module generates a pulse from the energy deposited in each crystal, which the readout module processes to create a new pulse specific to the crystal block. Then, an energy resolution is applied in the crystal-blurring module, followed by application of the dead-time module and the energy-window module on the single-event level [4]. The preceding steps generate a single-event file containing a list of single events. Application of the coincidence sorter

module to the single-event file creates the ROOT coincidence file, taking into account the coincidence pair events within the coincidence time window and the applied death time.

4.3.2 Calculation methodology

The counting of true, scatter, and random coincidences is controlled by the definition of the parameter given by the user during data analysis. We defined true coincidence as two photons produced by the same annihilation that did not interact with the scatter phantom. Scatter coincidence occurs when one of the two photons interacts with the scatter phantom or the bed patient's before reaching the detector. Random coincidence occurs when two photons originate from different annihilation's. For the GATE simulation of data analysis, we used a C++ program to calculate the number of true, scatter, and random coincidences based on a ROOT coincidence file. This file contained an array of multiple rows and columns, where each row corresponded to a specific ID coincidence and the columns contained the information of each photon, including the event ID number, the energy deposited energy, the detection coordinates, and the number of Compton and Rayleigh interactions. Those parameters were used to classify the coincidences as true, random, or scatter. Figure 4.14 shows the flow chart of the program that counts true, random, and scatter coincidences, which are used to calculate the sensitivity, SF, and NECR parameters.

4.3.3 Validation of Siemens $Biograph^{TM}$ mCT 20 Excel PET/CT System using Gate

The simulation results obtained for the performance parameters (SF, Sensitivity, NECR), spatial resolution and the true count rates are described. Then, the comparisons with experimental data sheet of $Biograph^{TM}$ mCT 20 Excel obtained from Siemens Company are discussed.

4.3.3.1 Spatial Resolution

The spatial resolution factor was calculated using the NEMA NU 2-2012 protocol in the transverse slice radially, tangentially, and axially. The images used to calculate the spatial resolution were reconstructed using the Software for Tomographic Image Reconstruction (STIR) with 3D Reprojection Filtered Back Projection algorithm (FBP3DRP) [40]. In addition, C++ analysis code, was used to build a sinogram by applying a Radon transformation to simulated data (ROOT format) and import it into STIR, where the reconstruction algorithm in FBP3DRP code was applied. The spatial resolution of the images was calculated with A Medical Imaging Data Examiner (AMIDE) [107] for each of the six different positions in the radial, tangential, and axial profiles using the full-width at half-maximum (FWHM) of the resulting point spread function.
The simulated spatial resolution results are compared with the experimental data in Table 4.7.

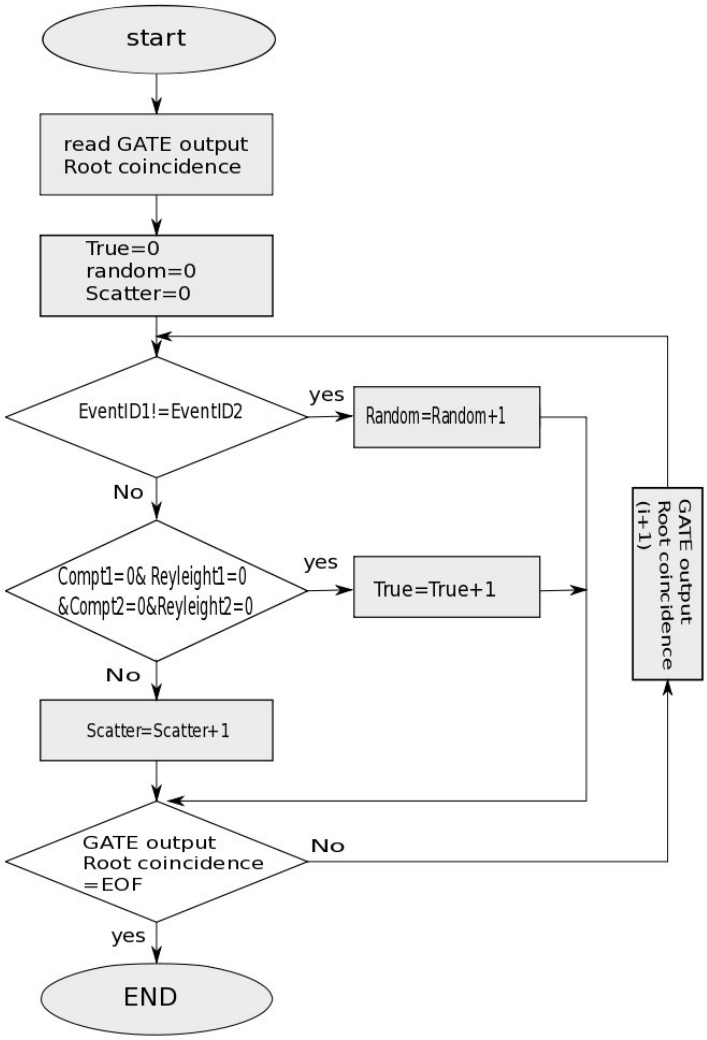

FIGURE 4.14: Flow chart for the C++ program the counts true, random, and scatter coincidences.

TABLE 4.7: Spatial resolution for PET/CT *Biograph*^{TM} mCT 20 Excel, calculated using the NEMA NU 2-2012 protocol

	Experimental results	Simulation
FWHM (mm) @ 1 cm, transverse	6	5.49 ± 0.02
FWHM (mm) @ 10 cm , transverse	6.3	5.96 ± 0.01
FWHM (mm) @ 1 cm, axial	5.7	5.47 ± 0.01
FWHM (mm) @ 10 cm, axial	6.2	5.72 ± 0.02

The spatial resolution parameter of the simulated system, reported in Table 4.7, agreed with the experimental data within 0.51 mm. This good agreement is mainly

due light spreading and light sharing between the PMTs that is not modeling in the GATE simulation.

4.3.3.2 Sensitivity

Figures 4.15(a) and 4.1(b) show the sensitivity of the detector for ^{18}F as count versus the thickness of aluminum in the phantom placed at the center and 10 cm from the center of the scanner FOV, respectively. The experimental data for sensitivity is compared with the simulation results (expressed in cps/kBq) in Table 4.8.

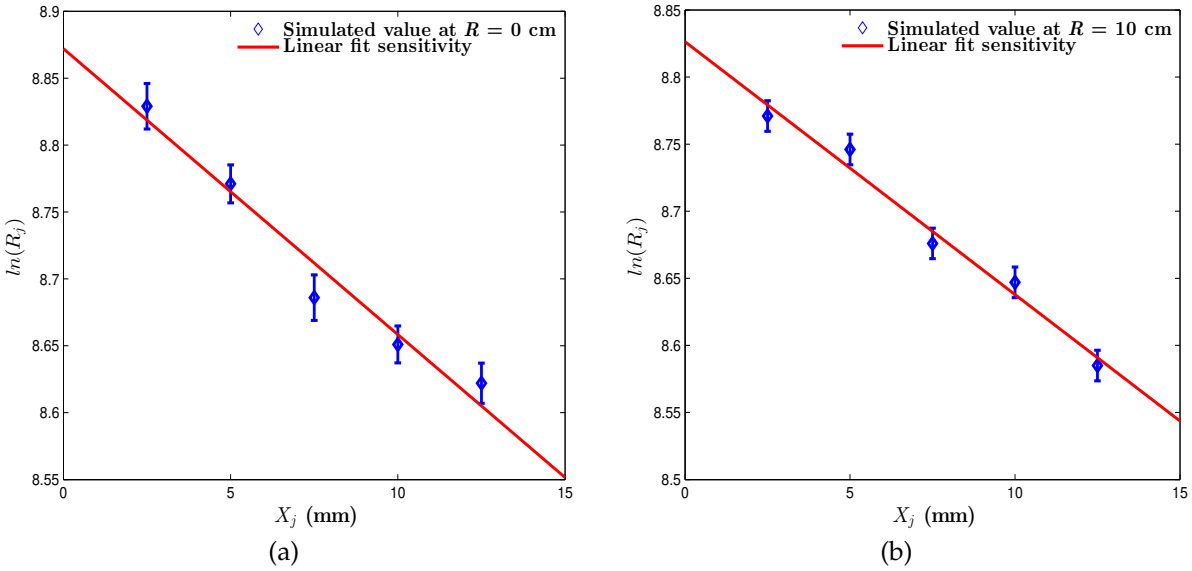

FIGURE 4.15: *Biograph*^{TM} mCT 20 Excel Sensitivity as a function of the shielding thickness of the phantom placed at the center of FOV (a), the phantom placed 10 cm from the center of FOV (b)

TABLE 4.8: Sensitivity parameter for PET/CT *Biograph*^{TM} mCT 20 Excel, calculated using the NEMA NU 2-2012 protocol

Experimental results (cps/kBq)	5.8
Simulation results (cps/kBq)	6.01 ± 0.002

The simulated sensitivity, reported in Table4.8, agreed with the experimental data by 3.6%. The difference in the values is explained by the limitations of the photomultiplier tube (PMT) resolution and by the absence of the modeling of light shielding between the detector blocks in the GATE simulation [99].

4.3.3.3 Scatter Fraction

A comparison between experimental data and simulation for the SF is given in Table 4.9

The simulated SF parameter, reported in Table 4.9, agreed with the experimental data by 2.7%. The difference is due to the approximation of the geometry used for

TABLE 4.9: Scatter fraction (SF) parameter for PET/CT *Biograph*^{TM} mCT 20 Excel

Experimental results	33 %
Simulation results	32.11 %

the GATE simulation and that the scanning bed was not taken into account in the simulation.

4.3.3.4 True Rate and Noise Equivalent Count Rate

Figure 4.16 displays the true count rate parameter obtained from the simulation as a function of the source activity concentration.

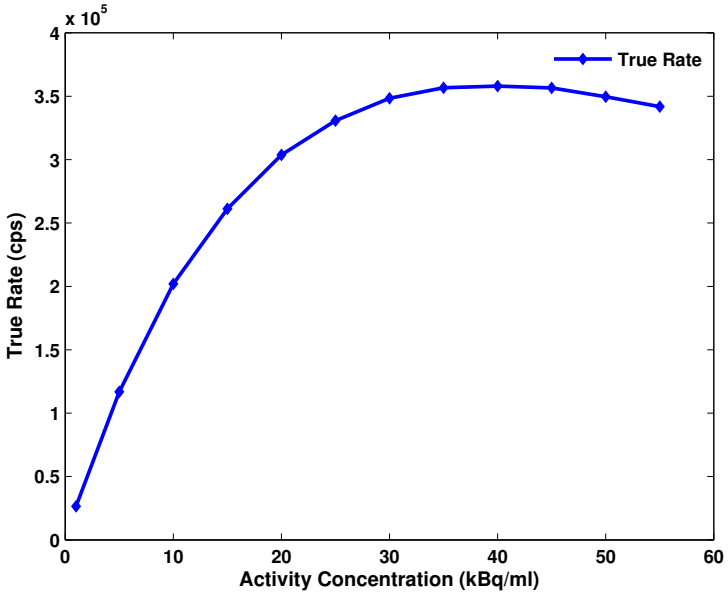

FIGURE 4.16: True count rate as a function of the source activity concentration.

Table 4.10 compares the experimental data for the peak true rate with the simulation results.

The simulated peak true rate, reported in Table 4.10, agreed with the experimental data by about 5.8%. The difference is mainly due to the simple dead time model used in the simulation.

TABLE 4.10: Peak true rate parameter for PET/CT *Biograph*^{TM} mCT 20 Excel

Experimental results	$380.00\,kcps\,@\,\leq 46kBq/cm^3$
Simulation results	$358.07\,kcps\,@\,40kBq/cm^3$

Figure 4.17 shows the simulation results for the NECR as a function of the source activity concentration.

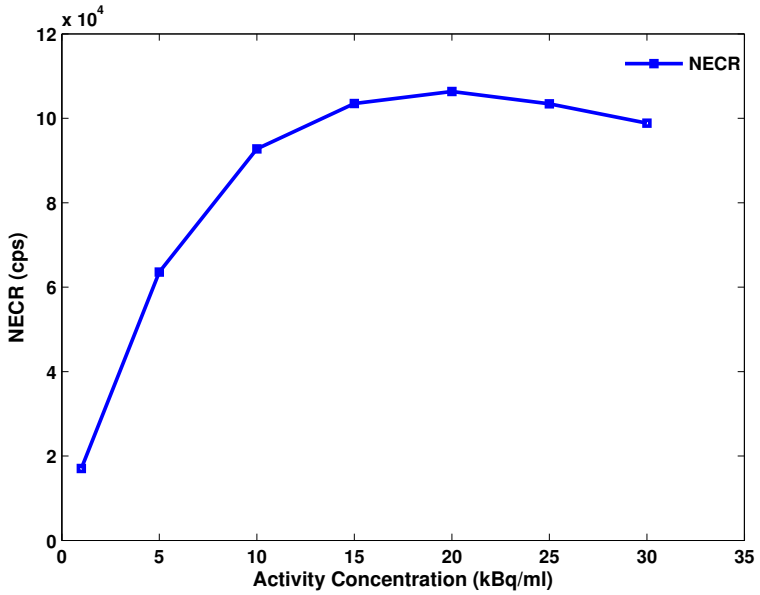

FIGURE 4.17: NECR as a function of the source activity concentration.

Table 4.11 compares the experimental data for the NECR peak with the simulation results.

TABLE 4.11: Noise equivalent count rate (NECR) peak for PET/CT $Biograph^{TM}$ mCT 20 Excel

Experimental results	$107.00\,kcps@ \leq 30kBq/cm^3$
Simulation results	$106.34\,kcps@20kBq/cm^3$

Table 4.11 presents the NECR peak value obtained from Figure 4.17 and the experimental value. These values agreed within 0.6%, with the difference mainly due to the simple dead time model used in the simulation.

4.3.4 Influence of Windows Timing Coincidences on Count Rate Performance

Figure 4.18 shows the true count rates for different coincidence time windows (4.1, 3.6, 3.1, and 2.6 ns) as a function of the source activity concentration, and Figure 4.19 shows the NECR as a function of the source activity concentration.

Figure 4.18(a) shows that varying the coincidence time window did not affect the true coincidence rate at lower activity concentrations. However, at higher activity concentrations, the true rate increased slightly for shorter coincidence time windows (peak true rate increased by 7.6%). Moreover, Figure 4.18(b) shows that at the higher activity, the random rate has been decreased by a factor of 30 % for the smaller CTW.

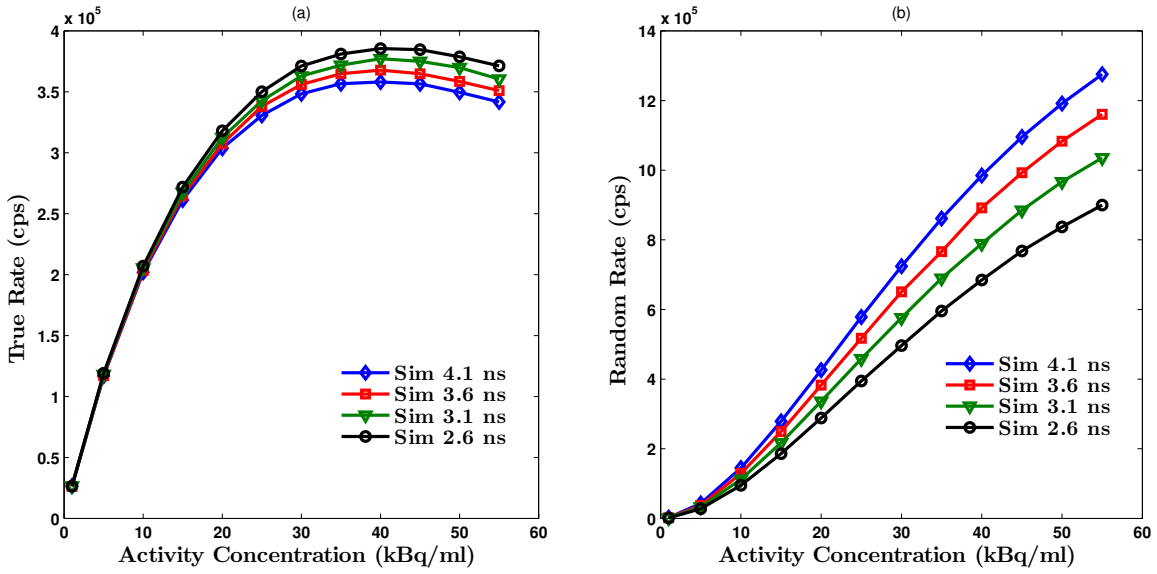

FIGURE 4.18: True rate vs. activity concentration for varying coincidence time windows.

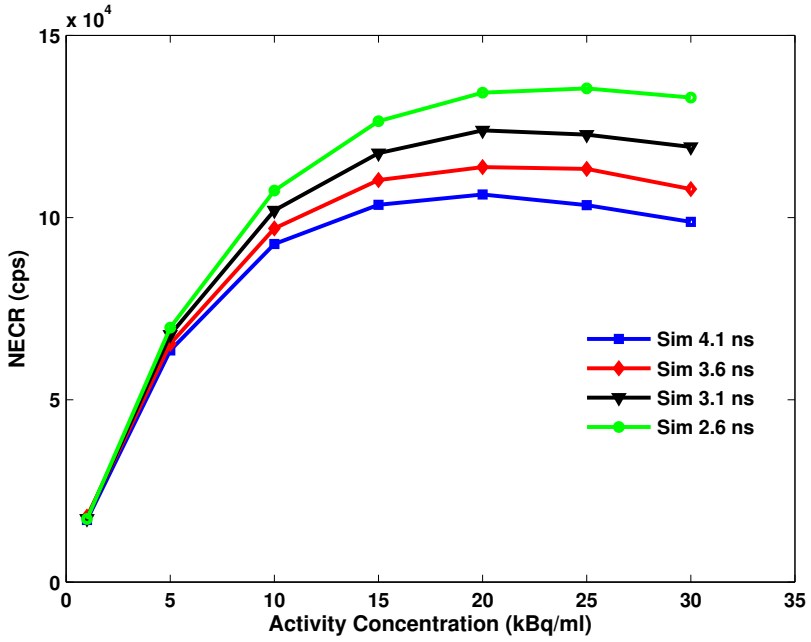

FIGURE 4.19: NECR vs. activity concentration for varying coincidence time windows.

Figure 4.19 shows significant improvement of NECR. This improvement is mainly due to the increase in the recorded true events and the decrease in the recorded random events for shorter coincidence time windows [5]. Using the smaller coincidence time window, the peak NECR increased by 27.4% when we change the simulated coincidence time window from 4.1 to 2.6 ns. The results suggest that a

larger CTW induces a lower NECR and the smaller CTW induces a higher NECR. The relation between the NECR administered activity (dose A_{adm}) is a nonlinear curve with a peak at moderate dose levels. Moreover, the administered activity (dose A_{adm}) depend on the intensity of activity distribution at time t, and the Administered dose is optimized when the NECR is maximized [105]. The larger CTW is also associated with smaller optimal doses while the smaller CTW increases the optimal dose. In addition, the decreasing of CTW decrease the FOV [100]. Therefore, the optimization of dose needs the use of specific CTW for A precise patient size. from our results the CTWs of 2.6, 3.1, 3.6, 4.1 ns are suggested to be used for the $patient - sizediameter(Psize) \leq 40cm$, $40cm \leq Psize \leq 50cm$, $50cm \leq Psize \leq 56cm$ and $56cm \leq Psize$ respectively.

4.3.5 Influence of Crystal/block Gap on Count Rate Performance and spatial resolution

The effect of windows coincidence time (WCT) along with block gap and inter-crystal gap on the count rate performance and on the spatial resolution is studied. Figures 4.20 and 4.21 show the true count rate and the NECR, respectively, as functions of the source activity concentration for different crystal gap/block gap combinations (0/4 mm, 0.1/2 mm and 0.2/0.4 mm), and Tables 4.12 and 4.13 summarize the peak true rate and the NECR peak for the same gap combinations.

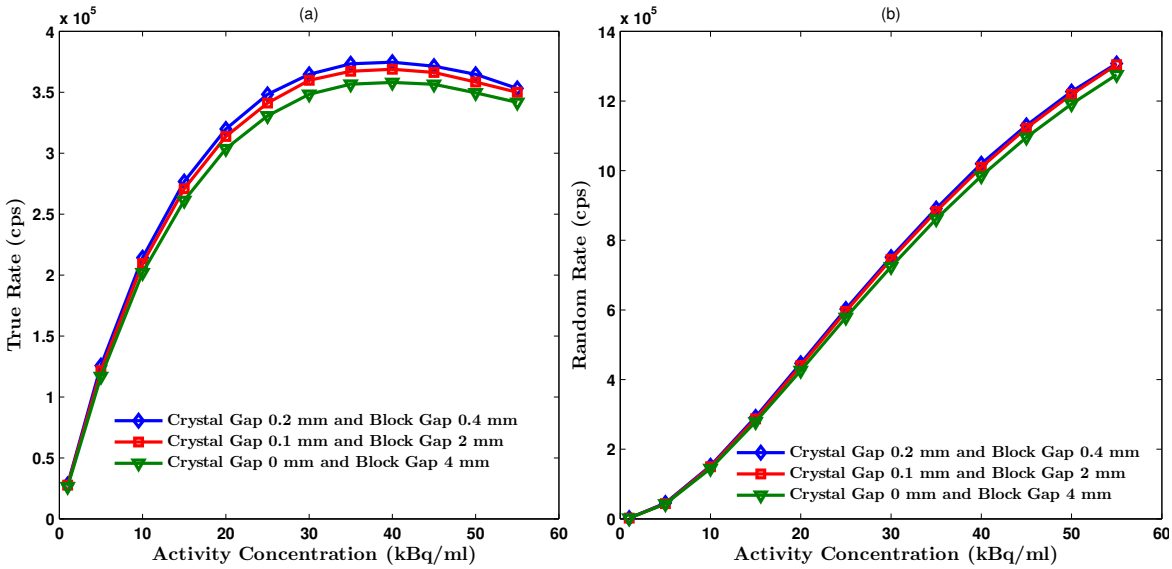

FIGURE 4.20: True rate vs. activity concentration for different crystal gap/block gap combinations.

Figure 4.20(a) shows that varying the crystal gap and the block gap did not affect the true coincidence rate at lower activity concentrations. However, at higher activity concentrations, the true rate increased slightly following an increase in the crystal gap and a decrease in the block gap. Moreover, Figure 4.20(b) shows that at the higher activity, the random rate has been not more affected by the the change of

the block gap and the crystal Gap. Table 4.12 presents the peak true rate for different crystal gap and block gap values. The peak true rate increased by 4.6% when the crystal gap and block gap changed from 0/4 mm to 0.2/0.4 mm.

TABLE 4.12: Peak true rate (cps) for different crystal and block gaps, calculated using the NEMA NU 2-2012 protocols

0 mm crystal gap and 4 mm block gap	358.07 $kcps@40kBq/cm^3$
0.1 mm crystal gap and 2 mm block gap	369.0 $kcps@40kBq/cm^3$
0.2 mm crystal gap and 0.4 mm block gap	374.70 $kcps@40kBq/cm^3$

Figure 4.21 shows that varying the crystal gap and the block gap did not affect the NECR at lower activity concentrations. However, at higher activity concentrations, the NECR increased slightly following an increase in the crystal gap and a decrease in the block gap. This improvement is obtained by minimizing the penetration of the photons into the neighboring crystal, which minimizes the parallax effect [108]. The peak NECR, reported in Table 4.13, increased by 5.5% when the crystal gap/block gap changed from 0/4 mm to 0.2/0.4 mm.

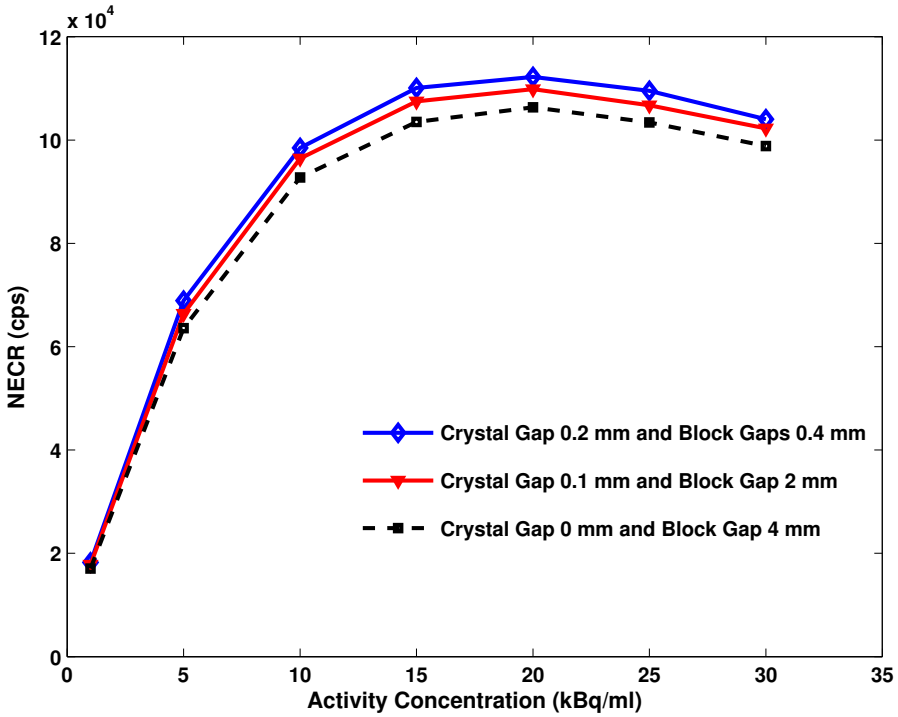

FIGURE 4.21: NECR vs. activity concentration for different crystal gap/block gap combinations.

Table 4.14 gives the transverse and axial spatial resolution at 1 and 10 cm for different crystal gap/block gap combinations (0/4 mm, 0.1/2 mm, and 0.2/0.4 mm),

TABLE 4.13: Peak NECR (cps) for different crystal and block gaps, calculated using the NEMA NU 2-2012 protocol

0 mm crystal gap and 4 mm block gap	106.34 $kcps@20kBq/cm^3$
0.1 mm crystal gap and 2 mm block gap	109.90 $kcps@20kBq/cm^3$
0.2 mm crystal gap and 0.4 mm block gap	112.23 $kcps@20kBq/cm^3$

while Table 4.15 presents the NECR peak for two detector models for several coincidence time windows and crystal gap/block gap combinations of 0/4 mm and 0.1/2 mm.

TABLE 4.14: Spatial resolution for different crystal and block gap combinations, calculated using the NEMA NU 2-2012 protocol

	0 mm crystal gap and 4 mm block gap	0.1 mm crystal gap and 2 mm block gap	0.2 mm crystal gap and 0.4 mm block gap
FWHM (mm) @ 1 cm, trans.	5.49 ± 0.01	5.33 ± 0.01	5.24 ± 0.02
FWHM (mm) @ 10 cm, trans.	5.96 ± 0.01	5.73 ± 0.06	5.68 ± 0.06
FWHM (mm) @ 1 cm, axial	5.47 ± 0.01	5.44 ± 0.03	5.45 ± 0.01
FWHM (mm) @ 10 cm, axial	5.72 ± 0.02	5.62 ± 0.03	5.61 ± 0.01

The data in Table 4.14 show that the transverse spatial resolution at 1 and 10 cm improved by 2.9% and 3.85%, respectively, and the axial spatial resolution at 1 and 10 cm improved by 0.5% and 1.74%, respectively, when the crystal gap/block gap combination changed from 0/4 mm to 0.1/2 mm. Moreover, the transverse spatial resolution at 1 and 10 cm improved by 1.7% and 0.8%, respectively, when the crystal gap/block gap changed from 0.1/2 mm to 0.2/0.4 mm. However, the axial spatial resolution at 10 cm improved by 0.18% and at 1 cm there was no improvement when the crystal gap/block gap changed from 0.1/2 mm to 0.2/0.4 mm. Hence, we conclude that the best model has a 0.1-mm crystal gap and a 2-mm block gap.

TABLE 4.15: Peak NECR for two detector models with different coincidence time windows, calculated using the NEMA NU 2-2012 protocol

	4.1 ns	3.6 ns	3.1 ns	2.6 ns
0 mm crystal gap and 4 mm block gap.	106.34 kcps @ $20kBq/cm^3$	113.85 kcps @ $20kBq/cm^3$	123.92 kcps @ $20kBq/cm^3$	135.46 kcps @ $20kBq/cm^3$
0.1 mm crystal gap and 2 mm block gap	109.90 kcps @ $20kBq/cm^3$	118.42 kcps @ $20kBq/cm^3$	128.83 kcps @ $20kBq/cm^3$	140.2 kcps @ $20kBq/cm^3$

Table 4.15 presents the peak NECR for two detector models with crystal gap/block gap values of 0/4 mm and 0.1/2 mm and several coincidence time windows. The NECR of the model with crystal gap/block gap values of 0.1/2 mm was better than that of the model with a crystal gap/block gap values of 0/4 mm.

4.3.6 Image quality

To acquire and evaluate reconstructed image quality in whole body PET imaging. We used the NEMA International Electrotechnical Commission (NEMA/IEC) body phantom, consist six fillable spheres with various sizes to simulate the cold and the hot lesion with a wall thickness of less than or equal to 1mm, four small spheres with internal diameters of 10, 13, 17, 22 mm and two large spheres with internal diameters of 28, 37 mm, and a cylindrical lung is inserted in the center of the phantom as illustrated in Figure 4.5 section 4.1.5. In addition a line source contained in a test phantom (a solid polyethylene cylinder used for the scatter fraction).
The NEMA/IEC body phantom is modeled using GATE to evaluate the reconstructed image quality of the simulated $Biograph^{TM}$ mCT 20 excel (the red ring as shown in the Figure 4.22(a and b)).

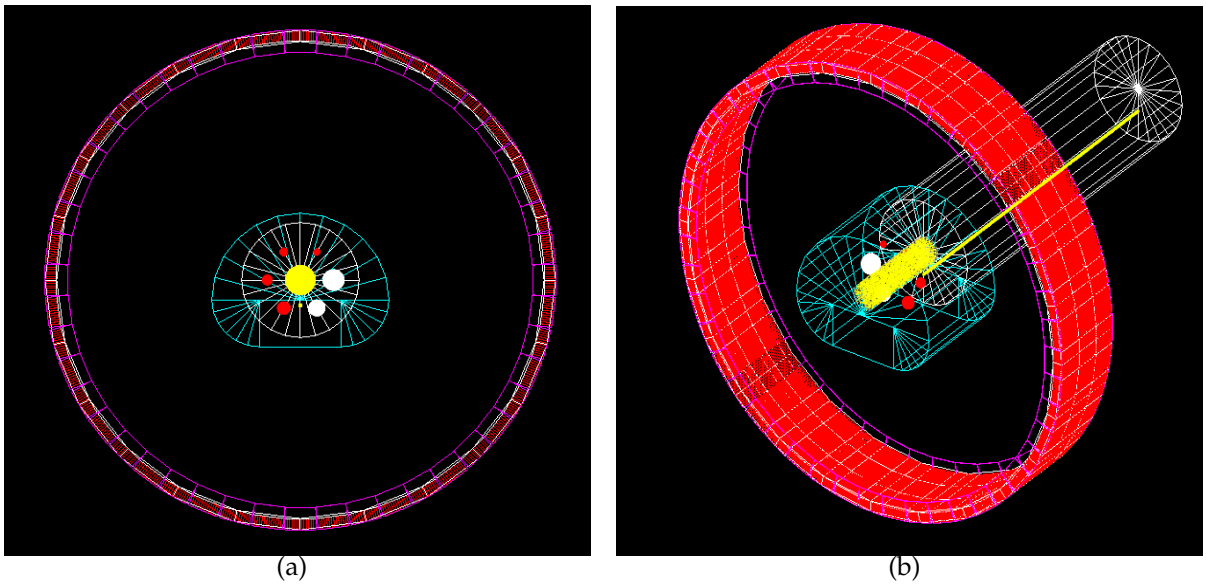

(a) (b)

FIGURE 4.22: (a) transverse view of body phantom, scatter phantom and scanner ring , (b) body and scatter phantom and the scanner geometry visualization with theta 135° and phi 135°

The modeled NEMA IEC body phantom as shown in Figure 4.22(a) and 4.22(b) (body, spheres and test phantom). The four smaller spheres (Red spheres in Figure 4.22(a)) were filled with a solution of ^{18}F diluted in the water with sphere-to-background ratio of either 8:1 or 4:1 (hot spheres), as well as the two bigger spheres (white spheres in Figure 4.22) were filled with distilled water and cylindrical lung (Yellow cylinder in Figure 4.22). The phantom was placed on the imaging table at the transverse center of FOV and positioned axially in the scanner in a way that the center of the spheres was at the middle slice of the scanner. The test phantom (the

White cylinder shown in Figure 4.22 (b)) was placed at the head end of the body phantom and adjacent to the body phantom.

4.3.6.1 Data collection and image reconstruction

The simulations have been performed using the GATE simulation toolkit. The data output ROOT coincidence file contain the number of true, scatter, and random coincidences. This file contained an array of multiple rows and columns, where each row corresponded to a specific ID coincidence and the columns contained the information of each photon, including the event ID number, the energy deposited, the detection coordinates, and the number of Compton and Rayleigh interactions. Those parameters were used to classify the coincidences as true, random, or scatter. The random and scatter coincidence wrongly assigned as coincidence event and can contribute substantially to the background image in PET scanner. Several methods are commonly used for randoms correction. They have been explained in the section 2.4.4. Since the GATE simulations allow random, scatter and true coincidences to be distinguished. The random and scatter coincidence correction can be applied in two different ways. In the first, the randoms and scatter correction is applied in the reconstruction algorithm. And in the second way we can subtract the estimated randoms and scattered from the prompts before the reconstruction. In our data output we used the second method to perform the random and scatter correction. A C++ analysis code , was used to build a sinogram by applying a Radon transformation to simulated data corrected (ROOT format) and import it into Software for Tomographic Image Reconstruction (STIR). The attenuation images correction was performed using attenuated image generated from the whole body phantom by STIR, this image slices are used to calculate the Attenuation coefficient, this coefficient are multiplied by the simulated data projection corrected random to get a corrected attenuation projection data. The reconstruction Ordered-Subsets Expectation-Maximization algorithm [47] (OSMAPOSL) code was applied to the corrected attenuation projection data with 4 iteration and 8 subsets. After that we use the Gaussian filter with the FWHM of 5 mm. We follow those parameters to acquired our data according the standard clinical whole body PET/CT protocol. Transverse slices through the axial center of the spheres within the image phantom were reconstructed with a selection of reconstruction parameters and different image corrections applied to the data. The Figure 4.23 shows the center slice image reconstructed.

4.3.6.2 Data processing

All slices were reconstructed and corrections applied. The total number of the selected slices to be analyzed is five slices. A center slice where the image contrast was assumed to be high was selected from the image slices and Four other slices as close as possible to +/-1 cm and +/-2 cm on either side of the central slice. A circular Regions of interest (ROI) were drawn on each hot sphere (10, 13, 17 and 22 mm) and cold sphere (28 and 37 mm) in the resulting transverses images after reconstruction. Then ROIs of the same sizes as the ROIs drawn on the hot and cold spheres were drawn in the background of the phantom on the center slice. And at a distance of 15 mm from the edge of the phantom and no closer than 15 mm to any of the other

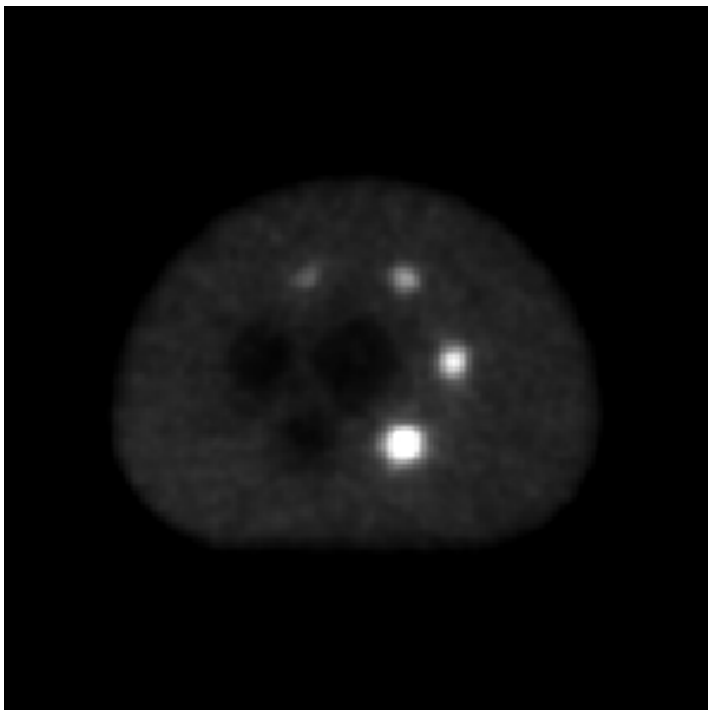

FIGURE 4.23: A slice reconstructed image with a Gaussian filter FWHM of 5 mm, 4 iterations, 8 subset and attenuation, scatter, random corrected.

spheres, we draw twelve 37 mm diameter ROIs on the background with ROIs of the smaller spheres (28, 22, 17, 13, and 10 mm) were drawn concentric to the twelve 37 mm ROI drawn on the background as shown in the Figure 4.24.

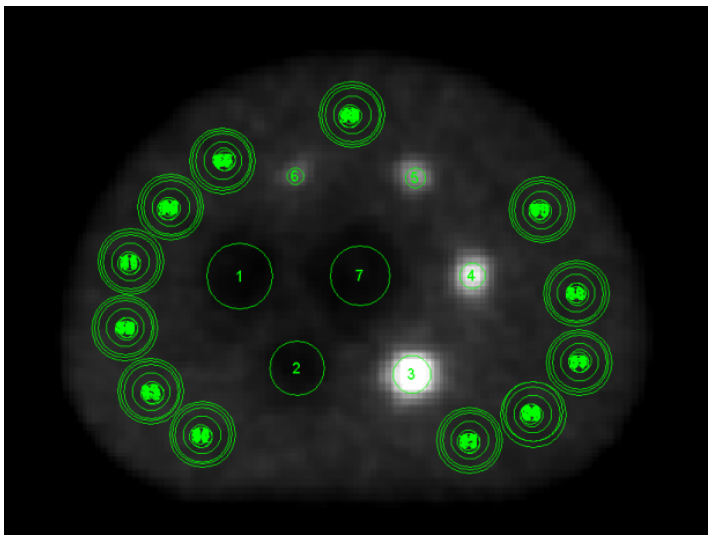

FIGURE 4.24: ROIs on Hot and cold spheres and lung insert, ROIs of the 37 mm, (28, 22, 17, 13 and 10 mm) and lung insert concentric to the 37 mm spheres for image quality analysis

The same procedure for drawing of spheres was performed on the other four slices as close as possible to +1/-1 cm and +2/-2 cm on either side of the central slice. Therefore, a total of sixty (60) ROIs of each sphere were drawn on the background, 12 ROIs on each of five slices. A circular ROI of 30 mm in diameter were also drawn on the lung insert. In addition Twelve other ROIs of the lung insert were drawn concentric to the 37 mm diameter ROI drawn on the background. This was also done all five slices. The image quality measurement based on the average counts in each image slice ROI recorded and used to perform calculations and evaluations of the following parameters : - the percentage of recovery coefficient. - percentage background variability. - percentage relative error - standard deviation on the quality of the reconstructed images.
These image quality parameters mentioned were calculated based on the formula stated in section 4.3.6.3 below.

4.3.6.3 Data Analysis

Image qualities for the hot spheres were calculated as percentage hotcontrast recovery coefficients. This was done to evaluate the contrast of hot spheres in a background regions.
the percentage hot contrast recovery coefficient $Q_{H,j}$ for sphere j, where j represents the hot spheres 10, 13, 17 and 22 mm is calculated by equation4.7

$$Q_{H,j} = \frac{\frac{C_{H,j}}{C_{B,j}} - 1}{\frac{a_H}{a_B} - 1} \times 100 \tag{4.7}$$

Where:
$C_{H,j}$ the average counts in the ROI for sphere j
$C_{B,j}$ the average of the background ROI counts for sphere j
a_H the activity concentration in the hot spheres
a_B the activity concentration in the background

Image qualities for cold spheres were calculated as percentage cold contrast recovery coefficient $Q_{C,j}$ for each sphere j, where j represents the cold spheres 28 and 37 mm using the equations4.8.

$$Q_{C,j} = (1 - \frac{C_{c,j}}{C_{B,j}}) \times 100 \tag{4.8}$$

Where:
$C_{c,j}$ the average counts in the ROI for sphere j
$C_{B,j}$ the average of the 60 background ROI counts for sphere j

The evaluation of the mean count variation of each sphere in the background from their corresponding mean count in the original spheres with either activity or no activity, was performed by the calculation of the background variability.
Percentage background variability N_j for all ROIs of sphere j (10, 13, 17, 22, 28 and 37 mm) in the image is given by:

$$N_j = (\frac{SD_j}{C_{B,j}}) \times 100 \tag{4.9}$$

Where SD_j is the standard deviation of the background ROI counts for sphere j, and is calculated as:

$$SD_j = \sqrt{\frac{\sum_{k=1}^{k} (C_{B,j,k} - C_{B,j})^2}{K-1}} \tag{4.10}$$

Where $C_{B,j}$ the average of the K=60 background regions of interest count of each spheres j.
The measurement of the difference between the expected counts and the measured counts in the images. as well as the measurement of the accuracy of attenuation and scatter corrections. Were performed by the calculation of Relative Count Error ($\triangle C$)

$\triangle C_{lung}$ relative error in the lung insert is the average of Relative error $\triangle C_{lung,i}$ expressed as percentage for each slice i is, given by the following equation 4.11:

$$\triangle C_{lung,i} = (\frac{C_{lung,i}}{C_{B,37mm}}) \times 100 \tag{4.11}$$

Where :
$C_{lung,i}$ the average counts in the lung insert ROI
$C_{B,37mm}$ the average of the sixty 37 mm background ROI of the lung insert.

To process and analyze the datasets, an automatic matlab program was developed to read the the image files and calculate the parameters described above: - the percentage of contrast recovery coefficient - percentage background variability - percentage relative error - standard deviation.

4.3.6.4 Image quality results following the NEMA NU 2-2012 protocol

Image quality results in images reconstructed of the simulated scanner model with a standard whole body PET/CT protocol Sphere-to-background activity ratio of 8:1 and 4:1 are presented bellow.

- **Sphere-to-background activity ratio of 8:1**

  The contrast recovery coefficients and background variability of the reconstructed images for the simulated scanner $Biograph^{TM}$ mCT 20 Excel using NEMA/IEC body phantom with a SBR of 8:1,are calculated using the equations 4.7 to 4.11. the results are given in table 4.24.

  The table 4.16 show that the contrast recovery coefficients for both hot and cold spheres increases with increasing sphere diameter (10 – 37 mm). The hot contrast recovery coefficient increases from 13.8 % for the 10 mm sphere to 79.8 % for the 22 mm sphere, while the cold contrast recovery coefficient increased from 61.4 % for the 28 mm sphere to 70.5 % for the 37 mm sphere. The background variability shows the values about 7 % for all spheres, the

TABLE 4.16: NEMA Image quality results for PET/CT *Biograph*^{TM} mCT 20 Excel with NEMA/IEC body phantom of 8:1 sphere-to-background ratio(SBR)

Sphere Diameters	Contrast recovery coefficient (%)	Background variability coefficient (%)
37 mm	70·5	7·3
28 mm	61·4	7·2
22 mm	79·8	7·0
17 mm	52·2	7·0
13 mm	27·8	7·3
10 mm	13·8	7·7
lung insert relative error (%)	26	

high obtained value is mainly due to the normalization that not performed in the data. The Accuracy of Attenuation and Scatter Corrections given by the lung insert relative error is 26 %.

- **Sphere-to-background activity ratio of 4:1**

The Figure 4.25 show a central slice-image reconstructed from the GATE simulation of NEMA/IEC body phantom with a SBR of 4:1. The Figure 4.25 show that it is possible to distinguish the spheres in the reconstructed images from the background Depending on the sphere size.

the results summarizes in table 4.17. the hot contrast recovery coefficient increases from 3.4 % to 24.8 % with increasing sphere diameter (10-22 mm), while the cold contrast recovery coefficient increase from 47.7 % to 57.4 % when sphere diameter increase from 28 mm to 37 mm. The background variability shows the values between 5.1 % and 7.2 % for all spheres. The Accuracy of Attenuation and Scatter Corrections given by the lung insert relative error that is 40 %.

4.4 Simulation study of the Siemens Biograph True point (True V) PET/CT System

4.4.1 Scanner geometry

The PET/CT *Biograph*^{TM} True point detection system is composed of 4 crowns of 48 Oxyorthosilicate Lutetium (LSO) modules defining an inner radius of 421 mm. Each module is divided into a matrix of 169 crystal $(4 \times 4 \times 20\, mm^3)$, successively $(axial \times transverse \times depth\, mm^3)$ separated by 0.1 mm Gap. The scanner geometry is illustrated in the Figure 4.26.
The characteristics, including geometry of the PET/CT *Biograph*^{TM} True point (true V) used in this work are summarized in Table 4.18.

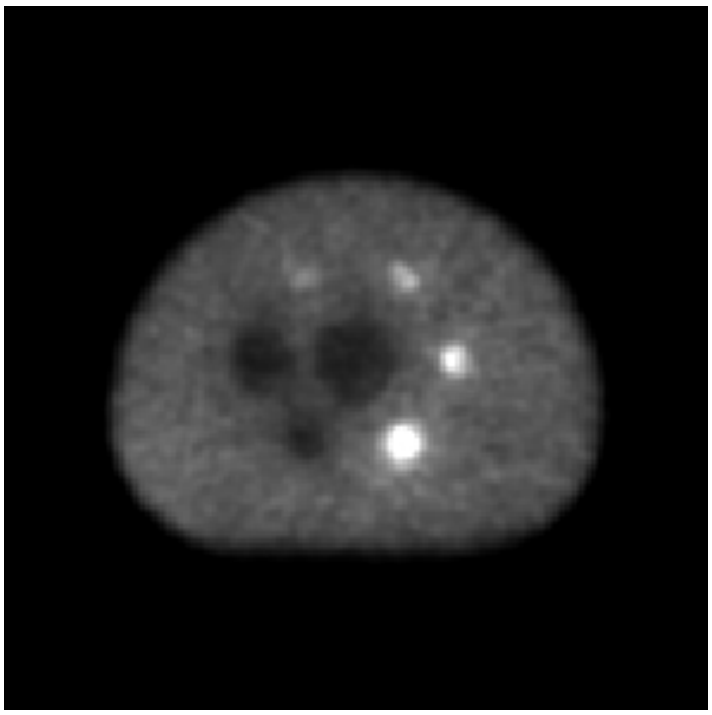

FIGURE 4.25: Slice-reconstructed image of simulated NEMA/IEC body phantom sphere-to-background ratio 4:1

TABLE 4.17: NEMA Image quality results for PET/CT *Biograph*^{TM} mCT 20 Excel with NEMA/IEC body phantom of 4:1 sphere-to-background ratio(SBR)

Sphere Diameters	Contrast recovery coefficient (%)	Background variability coefficient (%)
37 mm	57·4	5·1
28 mm	47·7	5·5
22 mm	24·8	6·3
17 mm	17·0	6·6
13 mm	9·5	7·0
10 mm	3·4	7·2
lung insert relative error (%)	40	

In addition to the specification parameters used for design of the scanner geometry, other parameters such as the physics process and the digitizer detection chain, summarized in table4.19, are also taken into accounts in the simulation.

4.4.2 Validation using GATE according to NEMA protocol

In this section, the simulation results obtained for the performance parameters spatial resolution sensitivity, SF, NECR and true count rates are described.

TABLE 4.18: Characteristics of clinical PET/CT *Biograph*^{TM} True Point (True V)

Detector Materiel	LSO
Crystal Dimensions(mm^3)	$4 \times 4 \times 20$
Detector Ring Diameter (cm)	82.4
Detector elements per block	169
Number of detector rings	52
Detector total number	32,448
Axial Field of view (mm)	216

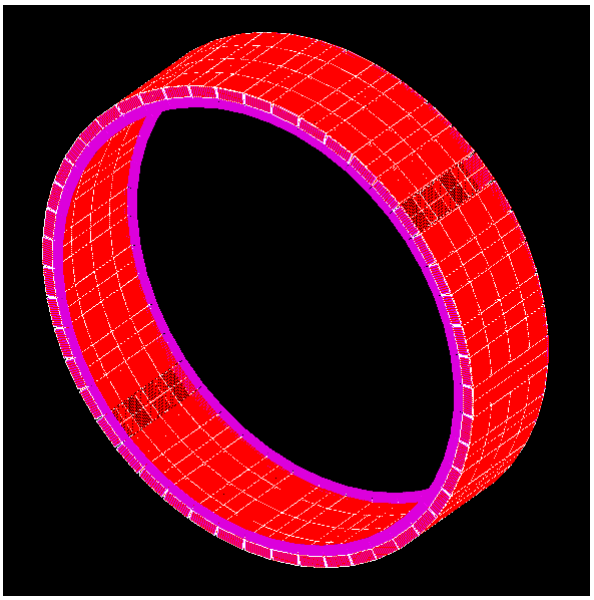

FIGURE 4.26: GATE geometry model of the clinical PET/CT *Biograph*^{TM} True point (True V). magenta indicates shielding, red, LSO blocks,

4.4.2.1 Spatial resolution

The spatial resolution factor was calculated according to the NEMA NU protocol described in detail at the section4.1.1, in the transverse slice radially, tangentially, and axially. The images used to calculate the spatial resolution were reconstructed using the Software for Tomographic Image Reconstruction (STIR) with Filtered Back Projection 3D Reprojection (FBP3DRP) algorithm.
The simulated spatial resolution results are compared with the experimental data in Table 4.20.

The spatial resolution parameter of the simulated system, reported in Table 4.20, agreed with the experimental data within 0.59 mm. This good agreement is mainly due to the absence of modeling in the GATE simulation of light spreading and light sharing between the PMTs.

TABLE 4.19: Physics process and the digitizer chain used in the simulated model PET/CT *Biograph*^{TM} True point (TrueV)

Physics process	*Biograph*^{TM} True point (True V)	
Physics	Photoelectric Compton Rayleigh Scattering	Low energy standard standard
Cuts	Electron (cm) Ray-X (keV) Second Electron (keV)	30 10^6 10^6
Energy resolution at 511 keV	< 14%	
Dead-Time (ns)	Singles Coincidences	900 -
CTW (ns)	4.5	
Energy Windows (kev)	435 - 650	

TABLE 4.20: Spatial resolution for PET/CT *Biograph*^{TM} True point (True V), calculated using the NEMA NU protocol

	Experimental results	Simulation
FWHM (mm) @ 1 cm, transverse	4.2	4.29
FWHM (mm) @ 10 cm , transverse	4.8	5.03
FWHM (mm) @ 1 cm, axial	4.7	5.29
FWHM (mm) @ 10 cm, axial	5.7	5.85

4.4.2.2 Sensitivity

The simulated sensitivity, reported in Table 4.21, agreed with the experimental data by 1.57 %. The difference in the values is explained by the limitations of the photomultiplier tube (PMT) resolution and by the absence of the modeling of light shielding between the detector blocks in the GATE simulation [99].

TABLE 4.21: Sensitivity parameter for PET/CT *Biograph*^{TM} True point (True V), calculated using the NEMA protocol

Experimental results (cps/kBq)	7.6
Simulation results (cps/kBq)	7.7

4.4.2.3 Scatter Fraction

The scatter fraction of the simulated model is calculated according to NEMA protocol using the scatter phantom and the formula 4.3 described in the section 4.1.3. A comparison between experimental data and simulation for the SF is given in Table 4.22

TABLE 4.22: Scatter Fraction(SF) for PET/CT *Biograph*^{TM} True point (True V), calculated using the NEMA protocol

Experimental results	<38 %
Simulation results	34.2 %

The simulated SF parameter, reported in Table 4.22, agreed with the experimental data by 7.6%. The difference is due to the approximation of the geometry used for the GATE simulation and that the scanning bed was not taken into account in the simulation.

4.4.2.4 Noise Equivalent Count Rate

The NECR is determined , as a described in the NEMA protocol presented in the section 4.1.4.
Figure 4.27 shows the simulation results for the NECR as a function of the source activity concentration.

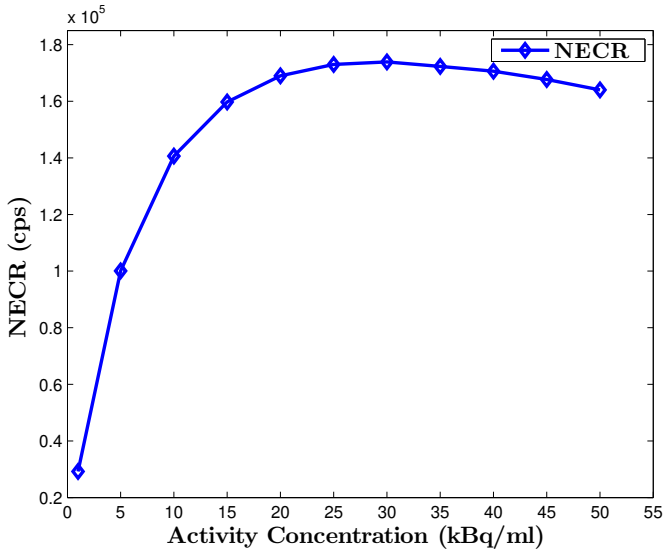

FIGURE 4.27: NECR as a function of the source activity concentration.

TABLE 4.23: Noise equivalent count rate (NECR) peak for the PET/CT *Biograph*^{TM} True Point (True V)

Experimental results	$165.00\,kcps@ \leq 32kBq/cm^3$
Simulation results	$173.92\,kcps@30kBq/cm^3$

Table 4.23 presents the NECR peak value obtained from Figure4.27 and the experimental value. The simulated value is better than the experimental value and agreed with it within 5.4%.

4.4.2.5 Image quality results following the NEMA protocol

Image quality results in images reconstructed with a standard whole body PET/CT protocol Sphere-to-background activity ratio of 8:1 and 4:1 are presented in the table 4.24 and table 4.25.

- **Sphere-to-background activity ratio of 8:1**

  The contrast recovery coefficients and background variability of the reconstructed images from the simulated scanner *Biograph*^{TM} True Point (True V) with a SBR of 8:1, are given in table 4.24.

TABLE 4.24: NEMA Image quality results for PET/CT *Biograph*^{TM} True Point (TrueV) with 8:1 sphere-to-background ratio(SBR).

Sphere Diameters	Contrast recovery coefficient (%)	Background variability coefficient (%)
37 mm	69·5	6·8
28 mm	57·3	7·3
22 mm	70·9	7·8
17 mm	50·0	8·3
13 mm	28·9	8·7
10 mm	10·3	9·0
lung insert relative error (%)	30	

From table 4.24 it is observed that the contrast recovery coefficients for both hot and cold spheres increases with increasing sphere diameter (10 – 37 mm). The hot contrast recovery coefficient increases from 10.3 % to 70.9 % when the sphere diameter increase from 10 mm to 22 mm, while the cold contrast recovery coefficient increase from 57.3 % for the 28 mm sphere to 69.5 % for the 37 mm sphere. The background variability shows the values between 6.8% and 9% for all spheres. The Accuracy of Attenuation and Scatter Corrections given by the lung insert relative error is 30 % .

- **Sphere-to-background activity ratio of 4:1**
  The Figure 4.28 show a central slice-image reconstructed from the GATE simulation of NEMA/IEC body phantom with a SBR of 4:1. The Figure 4.28 show that it is possible to distinguish the spheres in the reconstructed images from the background Depending on the sphere size.

  The contrast recovery coefficients and background variability of the reconstructed images from the simulated scanner *Biograph*^{TM} True Point (true V) with a SBR of 4:1, are given in table 4.24.

  From table 4.25 it is show that the contrast recovery coefficients for both hot and cold spheres increases with increasing sphere diameter (10 – 37 mm). The hot contrast recovery coefficient increases from 2.75 % for the 10 mm sphere to 22.6 % for the 22 mm sphere, while the cold contrast recovery coefficient

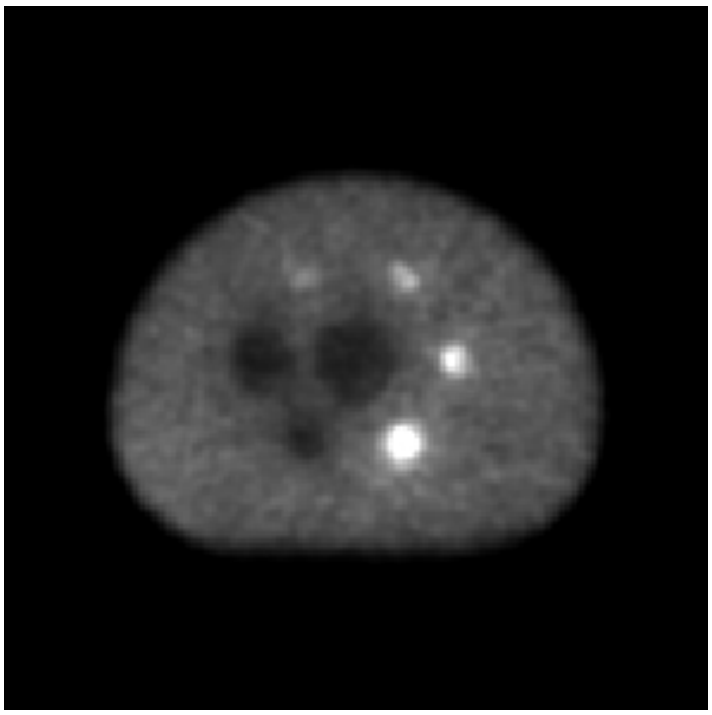

FIGURE 4.28: Slice-reconstructed image of simulated NEMA/IEC body phantom sphere-to-background ratio 4:1

TABLE 4.25: NEMA Image quality results for PET/CT *Biograph*^{TM} True Point (TrueV) with 4:1 sphere-to-background ratio(SBR)

Sphere Diameters	Contrast recovery coefficient (%)	Background variability coefficient (%)
37 mm	58·0	5·5
28 mm	47·1	5·7
22 mm	22·6	6·0
17 mm	16·8	6·3
13 mm	9·1	6·8
10 mm	2·7	7·6
lung insert relative error (%)	39·5	

increase from 47.1 % for the 28 mm sphere to 58 % for the 37 mm sphere. The background variability shows the values between 5.5 % and 7.6 for all spheres. The Accuracy of Attenuation and Scatter Corrections given by the lung insert relative error is 39.5 % .

4.5 Conclusion

In this chapter, we have presented the determination of the performance parameters, Scatter Fraction, Sensitivity, NEC, and count rates from the simulations performed with the designed model of the clinical ECAT EXACT HR+ scanner, using GATE. The validation shows good agreements with the published experimental data for this type of scanner. In addition, we have presented the influence of CTW and the dead time on the count rate performance using GATE. The obtained simulation results show that the true coincidences and NECR enhances when we minimize CTW and change the dead time from paralyzable model to non-paralyzable. This change increase the NECR factor. This factor is among several improving the image quality in the clinical PET scanner ECAT EXACT HR+. In addition, the validation of the clinical $Biograph^{TM}$ mCT 20 Excel scanner using GATE V7.1 and the NEMA NU 2-2012 protocol showed that there was good agreement between the simulated and the experimental data for the scatter fraction, sensitivity, and count rate performance measurements and the spatial resolution. The simulation study results showed that the true coincidences and NECR increase when the coincidence time window is minimized, the crystal gap is increased, and the block gap is decreased. However, the model with a 0.1-mm crystal gap and a 2 mm block gap showed improved spatial resolution. In addition the image quality shows good results.

The validation of the clinical the $Biograph^{TM}$ True point scanner using GATE V7.1 and the NEMA NU protocol showed that there were good agreements between the simulated and the experimental data for the scatter fraction, sensitivity, and count rate performance measurements and the spatial resolution. In addition the image quality show a good improvement. Therefore, Using TORQUE as the job manager for our local cluster on which the simulations were run yielded a very good computing performance.

Conclusion

The thesis work focuses on the Clinical PET (Positron Emission Tomography) scanner performance using Monte Carlo Simulation. We have simulated three clinical PET scanners, the ECAT EXACT HR+ scanner, $Biograph^{TM}$ mCT 20 Excel scanner and $Biograph^{TM}$ True point (true V) using GATE (Geant4 Application for Tomographic Emission) and according to NEMA NU 2-2012 and NEMA NU 2-2001 protocols. We have implemented the scanner geometry as well as the NEMA phantom geometry, the source type and it's own geometry, digitizer chain, physics process and data acquisition mode for each one of the scanners sited before. The realization of this work takes into account considerable Monte-Carlo simulations time. In order to reduce it, we have used the local culster in our laboratory managed by the open- source package TORQUE version 6.1.0 based on the original wrapper Portable Batch System PBS . The simulations performed with the designed models of the clinical ECAT EXACT HR+ scanner, $Biograph^{TM}$ mCT 20 Excel scanner and $Biograph^{TM}$ True point (true V) are validated following the NEMA NU 2-2012 and NEMA NU 2-2001 protocol. The performance parameters Scatter Fraction, Sensitivity, NECR and spatial resolution are calculated for the both simulated model's and compared with the experimental Data. The simulated results show that the performances of the experimental measured Data are accurately reproduced by GATE. The results show an agreement between the simulation and the experimental data where the obtained error is not exceeding 11%, and the reasons for these slight disagreements are due to the absence in the simulation of some components, such as the reflective material between the crystals and the bed patient also the dead time and PMT proprieties .
The validated models are used to study the influence of some parameters such as the CTW, the Dead Time and the block gap and intercrystal gap on the count rate performance and the spatial resolution. The clinical ECAT EXACT HR+ scanner is used to study the effect of changing the CTW and dead time model on the count rate performance using the GATE code, the obtained simulation results show that the true coincidences and NECR increase when we minimize CTW and change the dead time from paralyzable model to non-paralyzable. The peak NECR increased by 38% when we change the simulated coincidence time window from 12 to 6 ns and The NECR peak also increase respectively by 4.3% and 6.5% using two CTW (12 ns and 8 ns) and changing the dead time from 5000 ns paralyzable to 4900 ns non-paralyzable. In the other hand, the $Biograph^{TM}$ mCT 20 Excel scanner validated using GATE is used to study the effect of the CTW and the block gap and inter-crystal gap on the count rate and spatial resolution in order to optimize the administered dose to the patient . The results showed that the true coincidences and NECR increase when the coincidence time window is minimized, the crystal gap is increased, and the block gap is decreased. The peak true rate increased by 7.7% and the peak NECR increased by 27.4% when we change the simulated coincidence time

window from 4.1 to 2.6 ns. In addition the peak true rate increased by 4.6% and the peak NECR increased by 5.5% when the crystal gap and block gap changed from 0/4 mm to 0.2/0.4 mm. However, the model with a 0.1-mm crystal gap and a 2-mm block gap showed improved spatial resolution. The both scanner $Biograph^{TM}$ mCT 20 Excel and $Biograph^{TM}$ True Point(true V) scanner validated using GATE were used to perform the image quality ,Accuracy of attenuation ,and scatter correction according the NEMA/IEC body phantom [6]. The obtained results show for both scanner $Biograph^{TM}$ mCT 20 Excel and the $Biograph^{TM}$ True point (with True V option) a good image quality , a hight contrast for the hot and cold spheres and the background variability less than 10 %.

Appendix A

list of Publication

1 Rahal Saaidi et al. “A Monte Carlo Study of Clinical PET ECAT EXACT HR+ Using GATE”. In: Basic Concepts in Nuclear Physics: Theory, Experiments and Applications. Springer, 2016, pp. 223–225.

2 Rahal Saaidi et al. “GATE Simulation of a Clinical PET Scanner: Influence of Windows Timing Coincidences and Dead Time on Count Rate Performance”. In: Proceedings of Engineering and Technology PET 19 (2017), pp. 31–35.

3 Saaidi, R., Toufique, Y., Zeghari, A., El kharrim, A., and Cherkaoui El Moursli, R. (2019). GATE Simulation Study of the Siemens Biograph mCT 20 Excel PET/CT System, Polish Journal of Medical Physics and Engineering, 25(1), 7-14. doi: https://doi.org/10.2478/pjmpe-2019-0002

4 A ZEGHARI et al. “Modeling of a Linear Accelerator Saturne 43 and Study of Photon Dose Distributions”. In: Proceedings of Engineering and Technology PET 19 (2017), pp. 104–110.

5 Zeghari A, Saaidi R, Mghar M, Cherkaoui ElMR, (2018) "Monte Carlo Study of Photon Dose Distributions Produced By 12 MV Linear Accelerator". J of Biosens Biomark Diagn 3(1): 1-5. DOI: 10.15226/2575-6303/3/1/00120

6 A. Zeghari, R. Saaidi, and R. Cherkaoui El Moursli. “Investigation of variance reduction techniques parameters to enhance the efficiency for a 12 MV photon beam”. In: Journal of Radiation Research and Applied Sciences 12.1 (2019),pp. 192–199. DOI: 10.1080/16878507.2019.1623573.

7 A Zeghari, R Saaidi, and R Cherkaoui El Moursli. “Enhancement of the Dose on 12 MV Linac with Free Flattening Filter Mode”. In: Journal of Biomedical Physics and Engineering (2019).

Bibliography

[1] N. Karakatsanis et al. "Comparative evaluation of two commercial PET scanners, ECAT EXACT HR+ and Biograph 2, using GATE". In: *Nuclear Instruments and Methods in Physics Research Section A: Accelerators, Spectrometers, Detectors and Associated Equipment* 569.2 (2006). Proceedings of the 3rd International Conference on Imaging Technologies in Biomedical Sciences, pp. 368 –372. ISSN: 0168-9002. DOI: https://doi.org/10.1016/j.nima.2006.08.110. URL: http://www.sciencedirect.com/science/article/pii/S016890020601477X.

[2] DW Townsend. "Physical principles and technology of clinical PET imaging". In: *Annals-Academy of Medicine Singapore* 33.2 (2004), pp. 133–145.

[3] Dimitrios Nikolopoulos et al. "Comparative study using Monte Carlo methods of the radiation detection efficiency of LSO, LuAP, GSO and YAP scintillators for use in positron emission imaging (PET)". In: *Nuclear Instruments and Methods in Physics Research Section A: Accelerators, Spectrometers, Detectors and Associated Equipment* 569.2 (2006), pp. 350–354.

[4] P Gonias et al. "Validation of a GATE model for the simulation of the Siemens biograph^{TM} 6 PET scanner". In: *Nuclear Instruments and Methods in Physics Research Section A: Accelerators, Spectrometers, Detectors and Associated Equipment* 571.1-2 (2007), pp. 263–266.

[5] OpenGATE Collaboration. In: (). URL: http://wiki.opengatecollaboration.org/index.php/Users_Guide_V7.1.

[6] A Perkins et al. "NEMA Standards Publication NU 2-2012: Performance measurements of positron emission tomographs". In: *Rosslyn USA: National Electrical Manufacturers Association (NEMA)* (2012).

[7] Marcel Guillaume et al. "Recommendations for fluorine-18 production". In: *International Journal of Radiation Applications and Instrumentation. Part A. Applied Radiation and Isotopes* 42.8 (1991), pp. 749 –762. ISSN: 0883-2889. DOI: https://doi.org/10.1016/0883-2889(91)90179-5. URL: http://www.sciencedirect.com/science/article/pii/0883288991901795.

[8] IAEA Radioisotopes and RADIOPHARMACEUTICALS SERIES No. "Cyclotron Produced Radionuclides: Guidance on Facility Design and Production of [18F] Fluorodeoxyglucose (FDG)". In: (3).

[9] E.E. Kim et al. *Clinical PET and PET/CT: Principles and Applications*. Springer New York, 2012. ISBN: 9781441908025. URL: https://books.google.co.ma/books?id=jj9eHkn1tR0C.

[10] Dale L Bailey et al. *Positron emission tomography*. Springer, 2005.

[11] SR Cherry, JA Sorenson, and ME Phelps. *Physics in Nuclear Medicine, Saunders, Philadelphia, PA*. Tech. rep. ISBN 0-7216-8341-X, 2003.

[12] Aswin John Mathews. "A four-dimensional image reconstruction framework for PET under arbitrary geometries". In: (2014).

[13] Simon R Cherry and Magnus Dahlbom. "PET: Physics, instrumentation, and scanners". In: *PET*. Springer. 2004, pp. 1–124.

[14] DR Dance et al. "Diagnostic radiology physics". In: *International Atomic Energy Agency* (2014).

[15] Glenn F Knoll. *Radiation detection and measurement*. John Wiley & Sons, 1999.

[16] Timothy G Turkington. "Introduction to PET instrumentation". In: *Journal of nuclear medicine technology* 29.1 (2001), pp. 4–11.

[17] Klaus Wienhard et al. "The ECAT HRRT: performance and first clinical application of the new high resolution research tomograph". In: *Nuclear Science Symposium Conference Record, 2000 IEEE*. Vol. 3. IEEE. 2000, pp. 17–2.

[18] Steven R Meikle and Ramsey D Badawi. "Quantitative techniques in PET". In: *Positron Emission Tomography*. Springer, 2005, pp. 93–126.

[19] Andreas Thon et al. "Rate-dependence of the key performance parameters in an Anger logic based PET detector". In: *Nuclear Science Symposium Conference Record, 2004 IEEE*. Vol. 6. IEEE. 2004, pp. 3375–3379.

[20] Craig S Levin et al. "Compton scatter and x-ray crosstalk and the use of very thin inter-crystal septa in high resolution PET detectors". In: *IEEE TransactionNuclear Science*. Vol. 44. IEEE. 1997, pp. 218–224.

[21] Gopal B Saha. *Basics of PET imaging: physics, chemistry, and regulations*. Springer, 2005.

[22] Stefaan Vandenberghe et al. "Recent developments in time-of-flight PET". In: *EJNMMI physics* 3.1 (2016), p. 3.

[23] Adam Alessio, Paul Kinahan, et al. "PET image reconstruction". In: *Nuclear medicine* 1 (2006), pp. 1–22.

[24] Frederic H Fahey. "Data acquisition in PET imaging". In: *Journal of nuclear medicine technology* 30.2 (2002), pp. 39–49.

[25] F Lamare et al. "Validation of a Monte Carlo simulation of the Philips Allegro/GEMINI PET systems using GATE". In: *Physics in Medicine & Biology* 51.4 (2006), p. 943.

[26] BW Jakoby et al. "Physical performance and clinical workflow of a new LSO HI-REZ PET/CT scanner". In: *Nuclear Science Symposium Conference Record, 2006. IEEE*. Vol. 5. IEEE. 2006, pp. 3130–3134.

[27] P Geramifar et al. "Monte Carlo based performance assessment of four Commercial GE Discovery PET/CT scanners using GATE". In: *Nuclear Science Symposium Conference Record, 2008. NSS'08. IEEE*. IEEE. 2008, pp. 3995–3999.

[28] John J Williams et al. "Detector characterization of discovery ST whole-body PET scanner". In: *Nuclear Science Symposium Conference Record, 2003 IEEE*. Vol. 2. IEEE. 2003, pp. 717–721.

[29] Lawrence R MacDonald et al. "Count-rate performance of the discovery STE PET scanner using partial collimation". In: *Nuclear Science Symposium Conference Record, 2006. IEEE*. Vol. 4. IEEE. 2006, pp. 2488–2493.

[30] Parham Geramifar et al. "Monte Carlo assessment of time-of-flight benefits on the LYSO-based discovery RX PET/CT scanner". In: *Biomedical Imaging: From Nano to Macro, 2008. ISBI 2008. 5th IEEE International Symposium on*. IEEE. 2008, pp. 364–367.

[31] Raymond F Muzic and Jeffrey A Kolthammer. "PET performance of the GEMINI TF: a time-of-flight PET/CT scanner". In: *Nuclear Science Symposium Conference Record, 2006. IEEE*. Vol. 3. IEEE. 2006, pp. 1940–1944.

[32] Ivo Rausch et al. "Performance evaluation of the Biograph mCT Flow PET/CT system according to the NEMA NU2-2012 standard". In: *EJNMMI physics* 2.1 (2015), p. 26.

[33] BW Jakoby et al. "Physical and clinical performance of the mCT time-of-flight PET/CT scanner". In: *Physics in Medicine & Biology* 56.8 (2011), p. 2375.

[34] CJ Thompson. "The effect of collimation on single rates in multi-slice PET". In: *IEEE Transactions on Nuclear Science* 36.1 (1989), pp. 1072–1077.

[35] Margaret E Daube-Witherspoon and Gerd Muehllehner. "Treatment of axial data in three-dimensional PET". In: *Journal of nuclear medicine* 28.11 (1987), pp. 1717–1724.

[36] Robert M Lewitt, Gerd Muehllehner, and Joel S Karp. "Three-dimensional image reconstruction for PET by multi-slice rebinning and axial image filtering". In: *Physics in Medicine & Biology* 39.3 (1994), p. 321.

[37] Michel Defrise et al. "Exact and approximate rebinning algorithms for 3-D PET data". In: *IEEE transactions on medical imaging* 16.2 (1997), pp. 145–158.

[38] Paul R Edholm, Robert M Lewitt, and Bernt Lindholm. "Novel properties of the Fourier decomposition of the sinogram". In: *Physics and Engineering of Computerized Multidimensional Imaging and Processing*. Vol. 671. International Society for Optics and Photonics. 1986, pp. 8–19.

[39] Rodney A Brooks and Giovanni Di Chiro. "Principles of computer assisted tomography (CAT) in radiographic and radioisotopic imaging". In: *Physics in Medicine & Biology* 21.5 (1976), p. 689.

[40] Paul E Kinahan, JG Rogers, et al. "Analytic 3 D image reconstruction using all detected events". In: *IEEE Transactions on Nuclear Science* 36.1 (1989), pp. 964–968.

[41] Fayal Ben Bouallegue et al. "Exact and approximate Fourier rebinning algorithms for the solution of the data truncation problem in 3-D PET". In: *IEEE transactions on medical imaging* 26.7 (2007), pp. 1001–1009.

[42] James G Colsher. "Fully-three-dimensional positron emission tomography". In: *Physics in Medicine & Biology* 25.1 (1980), p. 103.

[43] Richard Gordon, Robert Bender, and Gabor T Herman. "Algebraic reconstruction techniques (ART) for three-dimensional electron microscopy and X-ray photography". In: *Journal of theoretical Biology* 29.3 (1970), pp. 471–481.

[44] K Kouris et al. "Reconstruction from sparsely sampled data by art with interpolated rays". In: *IEEE transactions on medical imaging* 1.3 (1982), pp. 161–167.

[45] Xiao-Liang Xu, Jeih-San Liow, and Stephen C Strother. "Iterative algebraic reconstruction algorithms for emission computed tomography: A unified framework and its application to positron emission tomography". In: *Medical physics* 20.6 (1993), pp. 1675–1684.

[46] Arthur P Dempster, Nan M Laird, and Donald B Rubin. "Maximum likelihood from incomplete data via the EM algorithm". In: *Journal of the royal statistical society. Series B (methodological)* (1977), pp. 1–38.

[47] H Malcolm Hudson and Richard S Larkin. "Accelerated image reconstruction using ordered subsets of projection data". In: *IEEE transactions on medical imaging* 13.4 (1994), pp. 601–609.

[48] Jolyon Browne and AB De Pierro. "A row-action alternative to the EM algorithm for maximizing likelihood in emission tomography". In: *IEEE transactions on medical imaging* 15.5 (1996), pp. 687–699.

[49] ME Daube-Witherspoon et al. "Application of the row action maximum likelihood algorithm with spherical basis functions to clinical PET imaging". In: *IEEE Transactions on Nuclear Science* 48.1 (2001), pp. 24–30.

[50] Takashi Obi et al. "2.5-D simultaneous multislice reconstruction by series expansion methods from Fourier-rebinned PET data". In: *IEEE transactions on medical imaging* 19.5 (2000), pp. 474–484.

[51] Lawrence A Shepp and Yehuda Vardi. "Maximum likelihood reconstruction for emission tomography". In: *IEEE transactions on medical imaging* 1.2 (1982), pp. 113–122.

[52] Nicolas Grotus. "La synchronisation respiratoire pour l'exploration des tumeurs pulmonaires par tomographie par émission de positons". PhD thesis. Paris 11, 2009.

[53] M Defrise et al. "A normalization technique for 3D PET data". In: *Physics in Medicine & Biology* 36.7 (1991), p. 939.

[54] TR Oakes, V Sossi, and TJ Ruth. "Normalization for 3D PET with a low-scatter planar source and measured geometric factors". In: *Physics in Medicine & Biology* 43.4 (1998), p. 961.

[55] Gabriele Tarantola, Felicia Zito, and Paolo Gerundini. "PET instrumentation and reconstruction algorithms in whole-body applications". In: *Journal of Nuclear Medicine* 44.5 (2003), p. 756.

[56] Elena Rota Kops and Hans Herzog. "Template based attenuation correction for PET in MR-PET scanners". In: *Nuclear Science Symposium Conference Record, 2008. NSS'08. IEEE*. IEEE. 2008, pp. 3786–3789.

[57] I Torres-Espallardo et al. "Effect of inter-crystal scatter on estimation methods for random coincidences and subsequent correction". In: *Physics in Medicine & Biology* 53.9 (2008), p. 2391.

[58] John M Ollinger and Jeffrey A Fessler. "Positron-emission tomography". In: *IEEE Signal Processing Magazine* 14.1 (1997), pp. 43–55.

[59] S Grootoonk et al. "Correction for scatter in 3D brain PET using a dual energy window method". In: *Physics in Medicine & Biology* 41.12 (1996), p. 2757.

[60] Lingxiong Shao, Richard Freifelder, and Joel S Karp. "Triple energy window scatter correction technique in PET". In: *IEEE transactions on medical imaging* 13.4 (1994), pp. 641–648.

[61] M Bentourkia et al. "Energy dependence of scatter components in multispectral PET imaging". In: *IEEE transactions on medical imaging* 14.1 (1995), pp. 138–145.

[62] Joel S Karp et al. "Continuous-slice PENN-PET: a positron tomograph with volume imaging capability". In: *J Nucl Med* 31.5 (1990), pp. 617–627.

[63] Simon R Cherry and Sung-Cheng Huang. "Effects of scatter on model parameter estimates in 3D PET studies of the human brain". In: *IEEE transactions on nuclear science* 42.4 (1995), pp. 1174–1179.

[64] DW Townsend, RA Isoardi, and B Bendriem. *The theory and practice of 3d pet*. 1998.

[65] Bing Bai et al. "Model-based normalization for iterative 3D PET image reconstruction". In: *Physics in medicine & biology* 47.15 (2002), p. 2773.

[66] Nicholas Metropolis and Stanislaw Ulam. "The monte carlo method". In: *Journal of the American statistical association* 44.247 (1949), pp. 335–341.

[67] I Buvat, I Castiglioni, et al. "Monte Carlo simulations in SPET and PET". In: *QJ Nucl. Med* 46.1 (2002), pp. 48–61.

[68] W Ralph Nelson and Yoshihito Namito. *The EGS4 code system: solution of gamma-ray and electron transport problems*. Tech. rep. Stanford Linear Accelerator Center, 1990.

[69] Hideo Hirayama et al. *The EGS5 code system*. Tech. rep. 2005.

[70] Iwan Kawrakow. "The EGSnrc code system, Monte Carlo simulation of electron and photon transport". In: *NRCC Report Pirs-701* (2001).

[71] Judith F Briesmeister et al. "MCNPTM-A general Monte Carlo N-particle transport code". In: *Version 4C, LA-13709-M, Los Alamos National Laboratory* (2000), p. 2.

[72] John S Hendricks et al. "MCNPX extensions version 2.5. 0". In: *Los Alamos National Laboratory* (2005).

[73] J Baro et al. "PENELOPE: an algorithm for Monte Carlo simulation of the penetration and energy loss of electrons and positrons in matter". In: *Nuclear Instruments and Methods in Physics Research Section B: Beam Interactions with Materials and Atoms* 100.1 (1995), pp. 31–46.

[74] Francesc Salvat et al. *PENELOPE, an algorithm and computer code for Monte Carlo simulation of electron-photon showers*. Tech. rep. Centro de Investigaciones Energeticas Medioambientales y Tecnologicas (CIEMAT), 1996.

[75] J Sempau et al. "An algorithm for Monte Carlo simulation of coupled electron-photon transport". In: *Nuclear Instruments and Methods in Physics Research Section B: Beam Interactions with Materials and Atoms* 132.3 (1997), pp. 377–390.

[76] Sea Agostinelli et al. "GEANT4—a simulation toolkit". In: *Nuclear instruments and methods in physics research section A: Accelerators, Spectrometers, Detectors and Associated Equipment* 506.3 (2003), pp. 250–303.

[77] CJ Thompson, J Moreno-Cantu, and Y Picard. "PETSIM: Monte Carlo simulation of all sensitivity and resolution parameters of cylindrical positron imaging systems". In: *Physics in Medicine & Biology* 37.3 (1992), p. 731.

[78] H Zaidi, A Herrmann Scheurer, and C Morel. "Development of an object-oriented Monte Carlo simulator for 3D positron tomography". In: *Conf. Rec. of the International Meeting in Fully Three-Dimensional Image Reconstruction in Radiology and Nuclear Medicine*. Citeseer. 1997, pp. 176–179.

[79] H Zaidi, A Herrmann Scheurer, and Christian Morel. "An object-oriented Monte Carlo simulator for 3D cylindrical positron tomographs". In: *Computer methods and programs in biomedicine* 58.2 (1999), pp. 133–145.

[80] Division of Nuclear Medicine (university of washington). In: (). URL: http://depts.washington.edu/simset/html/user_guide/user_guide_index.html.

[81] G Santin et al. "GATE: A Geant4-based simulation platform for PET and SPECT integrating movement and time management". In: *IEEE Transactions on nuclear science* 50.5 (2003), pp. 1516–1521.

[82] Anthonin Reilhac et al. "Pet-sorteo: a platform for simulating realistic pet studies". In: *IEEE Symposium Conference Record Nuclear Science 2004.* Vol. 7. IEEE. 2004, pp. 4053–4057.

[83] C Ross Schmidtlein et al. "Validation of GATE Monte Carlo simulations of the GE Advance/Discovery LS PET scanners". In: *Medical physics* 33.1 (2006), pp. 198–208.

[84] D Strulab et al. "GATE (Geant4 Application for Tomographic Emission): a PET/SPECT general-purpose simulation platform". In: *Nuclear Physics B-Proceedings Supplements* 125 (2003), pp. 75–79.

[85] S Jan et al. "GATE V6: a major enhancement of the GATE simulation platform enabling modelling of CT and radiotherapy". In: *Physics in Medicine & Biology* 56.4 (2011), p. 881.

[86] Karine Assie et al. "Monte Carlo simulation in PET and SPECT instrumentation using GATE". In: *Nuclear Instruments and Methods in Physics Research Section A: Accelerators, Spectrometers, Detectors and Associated Equipment* 527.1-2 (2004), pp. 180–189.

[87] Sébastien Jan et al. "GATE: a simulation toolkit for PET and SPECT". In: *Physics in Medicine & Biology* 49.19 (2004), p. 4543.

[88] OpenGATE Collaboration. In: (). URL: http://wiki.opengatecollaboration.org/index.php/Users_Guide_V7.2.

[89] Adaptive Computing. In: (). URL: http://www.adaptivecomputing.com/products/open-source/torque/.

[90] Jan De Beenhouwer et al. "Cluster computing software for GATE simulations". In: *Medical physics* 34.6Part1 (2007), pp. 1926–1933.

[91] OpenGATE Collaboration. In: (). URL: http://wiki.opengatecollaboration.org/index.php/Installation_Guide_V7.1.

[92] Kris Thielemans et al. "STIR: software for tomographic image reconstruction release 2". In: *Physics in Medicine & Biology* 57.4 (2012), p. 867.

[93] Claire Labbé et al. "An object-oriented library for 3D PET reconstruction using parallel computing". In: *Bildverarbeitung für die Medizin 1999*. Springer, 1999, pp. 268–272.

[94] Claire Labbé et al. "An object-oriented library incorporating efficient projection/backprojection operators for volume reconstruction in 3D PET". In: *Proc. of 3D99 conference*. 1999.

[95] Gopal B Saha. *Basics of PET imaging: physics, chemistry, and regulations*. Springer, 2015.

[96] Hans Herzog et al. "NEMA NU2-2001 guided performance evaluation of four Siemens ECAT PET scanners". In: *IEEE Transactions on Nuclear Science* 51.5 (2004), pp. 2662–2669.

[97] Y Toufique et al. "Grid Applied to Monte-Carlo Simulations of Positron Emission Tomography Systemss". In: *6th Iberian Grid infrastructure conference proceeding* (2012), pp. 123–133.

[98] Suleman Surti et al. "A multiscanner evaluation of PET image quality using phantom studies". In: *Nuclear Science Symposium Conference Record, 2003 IEEE*. Vol. 4. IEEE. 2003, pp. 2425–2427.

[99] Y Toufique et al. "A benchmark of clinical PET using GATE simulation on the computing Grid". In: *2013 ACS International Conference on Computer Systems and Applications (AICCSA)*. IEEE. 2013, pp. 1–4.

[100] P Geramifar et al. "Investigation of time-of-flight benefits in an LYSO-based PET/CT scanner: A Monte Carlo study using GATE". In: *Nuclear Instruments and Methods in Physics Research Section A: Accelerators, Spectrometers, Detectors and Associated Equipment* 641.1 (2011), pp. 121–127.

[101] Nicolas A Karakatsanis et al. "Monte-Carlo based characterization of the counting rate (NECR) response for personalized optimization of the administered activity in clinical PET imaging". In: *Frontiers in Biomedical Technologies* 1.1 (2015).

[102] Parham Geramifar et al. "Performance comparison of four commercial GE discovery PET/CT scanners: A monte carlo study using GATE". In: *Iranian Journal of Nuclear Medicine* 17.2 (2009), pp. 26–33.

[103] Nicolas A Karakatsanis et al. "A simulation study of the counting-rate performance of clinical pet systems applying a methodology for optimizing the injected dose". In: *Nuclear Science Symposium Conference Record, 2008. NSS'08. IEEE*. IEEE. 2008, pp. 5014–5019.

[104] Nicolas Karakatsanis and Konstantina Nikita. "A simulation model of the counting-rate response of clinical pet systems and it's application to optimize the injected dose". In: *Biomedical Imaging: From Nano to Macro, 2009. ISBI'09. IEEE International Symposium on*. IEEE. 2009, pp. 398–401.

[105] Nicolas A Karakatsanis, George Loudos, and Konstantina S Nikita. "A methodology for optimizing the acquisition time of a clinical PET scan using GATE". In: *Nuclear Science Symposium Conference Record (NSS/MIC), 2009 IEEE*. IEEE. 2009, pp. 2896–2901.

[106] LR MacDonald et al. "Measured count-rate performance of the Discovery STE PET/CT scanner in 2D, 3D and partial collimation acquisition modes". In: *Physics in Medicine & Biology* 53.14 (2008), p. 3723.

[107] Sau P loening A. "Amide a Medical Image Data Examiner:User's Manual V0.3.1". In: (2014). URL: http://amide.sourceforge.net/help/C/index.html.

[108] S Lashkari et al. "The influence of crystal material on intercrystal scattering and the parallax effect in PET block detectors: a Monte Carlo study". In: *4th Kuala Lumpur International Conference on Biomedical Engineering 2008*. Springer. 2008, pp. 633–636.

Résumé

Dans ce travail de thèse, la plate-forme GATE (Application Geant4 pour émission tomographique) a été utilisée pour valider la simulation des scanners PET clinique suivants ECAT EXACT HR+, Biograph™ True point (True V) et Biograph™ mCT 20 Excel selon le protocole NEMA NU 2-2001 et NEMA NU 2-2012. Nos résultats montrent un bon accord avec les données expérimentales. Le premier modèle validé ECAT EXACT HR+ est utilisé pour étudier l'influence des fenêtres temporelles de coïncidence et du temps mort sur le rendement du taux de comptage. Les résultats obtenus montrent que la Minimisation les fenêtres de temps de coïncidence augmentent la performance du taux de comptage NECR et vrai. De plus, le NECR est augmenté lorsque nous utilisons un temps mort non paralysable au lieu de paralysable. Le modèle validée de Biograph™ mCT 20 Excel est utilisée pour étudier l'effet de la fenêtre temporelle de coïncidence avec l'écart de bloc et l'écart entre cristaux sur les performances du taux de comptage et la résolution spatiale. Les résultats obtenues montrent que la diminution de fenêtre temporelle de coïncidence et l'écart de bloc ainsi qu'une augmentation de l'écart intercristal augmentent les performances du taux de comptage et améliorent la résolution spatiale. Pour les deux scanners Biograph™ mCT 20 Excel et Biograph™ True Point (True V), cette simulation permet d'améliorer la qualité d'image, la précision de l'atténuation et correction de dispersion selon le fantôme de corps NEMA / IEC.

Mots-clés : *Scanner PET* ; NEMA; GATE; temps mort; fenêtre temporelle.

Abstract

In this thesis work, we used GATE to validate the clinical PET scanner ECAT EXACT HR+, Biograph™ mCT 20 Excel and Biograph™ True point (True V) according to the NEMA NU 2-2001 and the NEMA NU 2-2012 protocol. Our results showed good agreement with experimental data. The first validated model ECAT EXACT HR+ is used to study the influence of the coincidence timing windows (CTW) and dead time (DT) on the Count rate performance. The obtained results show that the minimizing coincidence time windows increase the NECR and True count rate performance. Moreover, the NECR is increased when non paralyzable dead time is employed instead of paralyzable one. The validated model of Biograph™ mCT 20 Excel is used to study the effect of the CTW along with the block gap and the intercrystal gap on the count rate performance and the spatial resolution. The results showed that a decrease in the coincidence time window and the block gap and an increase in the intercrystal gap increase the count rate performance and improve the spatial resolution. In addition, the both scanner Biograph™ mCT 20 Excel and the Biograph™ True point (with True V option) scanner validated using GATE were used to perform the image quality, Accuracy of attenuation, and scatter correction according the NEMA/IEC body phantom. The obtained images show a good image quality.

Key Words : PET Scanner; NEMA; GATE; dead time; Coincidence Windows time.